A Geophysical Investigation of the Arctic Sea Ice Surface

Melinda Anne Webster

A dissertation

submitted in partial fulfillment of the

requirements for the degree of

Doctor of Philosophy

University of Washington

2016

Reading Committee:

Ignatius G. Rigor, Chair

Eric D'Asaro

Jody Deming

Program Authorized to Offer Degree:

Oceanography

University of Washington

Abstract

A Geophysical Investigation of the Arctic Sea Ice Surface

Melinda Anne Webster

Chair of the Supervisory Committee:
Affiliate Assistant Professor Ignatius G. Rigor
Oceanography

The oldest records of the Arctic sea ice pack illustrate a frozen, yet dynamic icescape composed of hummocks and weathered ridges draped in thick snow. In recent decades, the effects of climate change have transformed this image: the Arctic sea ice pack is younger, thinner, and more dynamic. As a result, the properties of its surface are changing and impacting its ice mass balance. This work investigates the recent geophysical changes of the Arctic sea ice surface, giving emphasis to snow, melt ponds, and sea ice surface topography through the three following papers: (1) interdecadal changes in spring snow depth, (2) seasonal evolution of melt ponds, and (3) the spatial scaling of melt pond distributions.

In the first analysis, recent in situ and airborne observations were used to extend the snow climatology to the contemporary period. Through this, we were able to identify the interdecadal

change in spring snow depth distributions, and found that snow has thinned by 37 ± 29% in the western Arctic and 56 ± 33% in the Beaufort and Chukchi seas. The decrease was attributed to later autumnal sea ice formation. During the peak snowfall period in autumn, snow falls into the ocean and melts due to the absence of sea ice.

In the second analysis, an algorithm was developed for identifying melt ponds in high-resolution satellite images of a Lagrangian site. The site was composed of mixed sea ice types, allowing for a comparison of seasonal melt pond evolution between first-year and multiyear sea ice undergoing the same forcings. Surprisingly, melt ponds formed three weeks earlier on multiyear sea ice than first-year sea ice. Nearly half of the snow on the multiyear sea ice was optically-thin, which likely contributed to early melt pond formation. The uniformity in melt pond formation, drainage, and distribution was inversely proportional to the level of sea ice deformation; melt pond uniformity increased with decreasing sea ice deformation.

The third analysis investigated the spatial scaling of melt pond distributions at two sites with homogenous (undeformed first-year) and heterogeneous (mixed deformation and age) sea ice. The relationship between small-scale variability in melt pond geometries and aggregate-scale estimates of melt pond fractions was examined. The results revealed that: (1) melt pond geometry is most variable before melt pond drainage at the heterogeneous site, but after melt pond drainage at the homogenous site, (2) aggregate-scale estimates of melt pond fractions in homogenous and heterogeneous sea ice sites are larger than previously recognized, ranging from ~70 km^2 to ~480 km^2, and (3) aggregate-scale estimates of melt pond fractions may be dependent on the composition of sea ice types and stage of melt pond evolution.

Chapter 2, published citation:

Webster, M. A., I. G. Rigor, S. V. Nghiem, N. T. Kurtz, S. L. Farrell, D. K. Perovich, and M. Sturm (2014), Interdecadal changes in snow depth on Arctic sea ice, *J. Geophys. Res. Oceans, 119,* 5395–5406, doi:10.1002/2014JC009985.

Chapter 3, published citation:

Webster, M. A., I. G. Rigor, D. K. Perovich, J. A. Richter-Menge, C. M. Polashenski, and B. Light (2015), Seasonal evolution of melt ponds on Arctic sea ice, *J. Geophys. Res. Oceans, 120,* doi:10.1002/2015JC011030.

Table of Contents

List of Figures

List of Tables

Acknowledgements

I am truly grateful for the community of which I've become a part of:

I would like to thank my advisor, Ignatius Rigor, for his guidance, patience, and support throughout my time at the University of Washington. I express my sincere thanks to my committee, Eric D'Asaro, Jody Deming, and LuAnne Thompson, and my Graduate Student Representative, Stephen Warren, for their genuine interest, encouragement, and constructive feedback. I would like to thank again Eric D'Asaro and Stephen Warren for their guidance and insightful discussions.

I am deeply grateful for the guidance, invaluable discussions, encouragement, and opportunities to experience sea ice first-hand from Bonnie Light and Don Perovich. I am very thankful for the helpful discussions and welcomed collaborations from Jackie Richter-Menge and Sinead Farrell. I am grateful for the opportunity to learn about the fascinating world of earth system modeling from Dave Bailey and Marika Holland. I am thankful for the opportunity to work with Son Nghiem, who has shown utmost patience and kindness. I thank Matthew Sturm for the introduction to the wondrous world of snow, and sharing his enthusiasm for exploring it further. I thank Seelye Martin for his kindness, encouragement, and generosity in sharing a library of sea ice knowledge, which motivates me to learn more. I thank Nathan Kurtz for his collaboration, as well as the introduction to the realm of radar and snow. I thank Chris Polashenski for the collaboration and helpful discussions on melt ponds. I thank the Operation IceBridge science team for the opportunity to participate in insightful discussions over the years. I appreciate the opportunity to work alongside a wonderful community at the Polar Science Center and School of Oceanography.

I am incredibly grateful for my family: both of my parents, Cathy and Bob Webster, for their encouragement, support, and for being inspirational figures; Steven Webster, Laura Tapp, and Benny, for their kindness and encouragement; Brian Webster, Katie Webster, and Olivia Webster, for their excitement and support; Rosalie Cook, Don and Merlene Webster, for their love and encouragement to follow one's passion and run fast; the Newman Clan, for their love and support; my friends, for their sanity and insanity.

Lastly, I would like express my love and gratitude for my husband, Josh Newman, who has given unwavering love and support.

Dedication

To my family

Chapter 1. Introduction

1.1 OVERVIEW

Over the last century, the Earth's global mean temperature has risen by 0.85°C as a result of climate change [*Stocker et al.,* 2013]. The greatest warming has occurred at high latitudes, where polar ice makes up only ~8% of the Earth's surface but is a key component in the global energy budget. Polar ice drives atmospheric circulation patterns [*Budikova,* 2009; *Hunke et al.,* 2010; *Overland et al.,* 2010; *Screen et al.,* 2013; *Vihma,* 2014], governs the ocean's meridional overturning circulation [*Killworth,* 1983; *Aagaard et al.,* 1985; *Aagaard and Carmack,* 1989; *Dickson and Brown,* 1994], and reflects 60–90% of incoming solar radiation at high latitudes [*Ruddiman,* 2001; *Comiso,* 2010]. In this dissertation, I focus on the ~30% of polar ice that is the Arctic sea ice cover, and document geophysical changes of its surface that have arisen due to climate change: a thinning snow cover, increasing melt pond coverage, and decreasing intra-floe heterogeneity in melt pond distributions. These three themes have been subdivided into chapters. Each chapter provides: (1) an in-depth look at the current understanding of the theme, (2) motivation for expanding our knowledge of it, (3) descriptions of data, tools, and techniques for obtaining new information, (4) evidence for establishing new conclusions, and (5) discussions of the implications to feedbacks within the Arctic system. This chapter begins with Section 1.2, which gives an introduction to the environment addressed by the themes of this dissertation.

1.2 THE ARCTIC SEA ICE COVER

What is Arctic sea ice? In simplest terms, it is the frozen part of the ocean in the Arctic, but Arctic sea ice serves many roles. It is a thermally insulating cover on top of the ocean [*Ono,* 1967; *Trodahl et al.,* 2001; *Pringle et al.,* 2007], a barrier of momentum transfer from surface winds [*Guest and Davidson,* 1991; *Morison and McPhee, 2001*], a hunting platform essential to Yupik and Inuit communities [*Krupnik and Jolly,* 2002; *Laidler,* 2006], a driver of deep water formation [*Aagaard et al.,* 1985; *Aagaard and Carmack,* 1989], a habitat for sympagic organisms [*Eicken et al.,* 2009; *Thomas and Dieckmann,* 2010], a hazard for the shipping and oil industries [*Van der Zwaag and Lamson,* 1990; *Brigham,* 2007; *Weidemann,* 2014], and one of the most reflective surfaces on Earth [*Grenfell and Perovich,* 1984; *Perovich et al.,* 2002a; *Perovich and Polashenski,* 2012]. From its molecular, tetrahedral structure to the two percent of the planet that it can cover [*Parkinson and Cavalieri,* 2008; *Cavalieri and Parkinson,* 2012], Arctic sea ice is awe-inspiring in the truest sense. Its wide-reaching influence has made it a priority subject to be explored, studied, and monitored, which we continue to do today.

From satellite observations in 1978–1996, we learned that the Arctic sea ice pack normally cycled between 7 million and 15 million square kilometers with the seasons, and that a portion of the sea ice pack survived the melt season every year [*Gloersen et al.,* 1992; *Parkinson et al.,* 1999]. Summer survival is what makes Arctic sea ice a composite of age, thickness, and deformation (Figure 1.1). Age is the most common metric for characterizing sea ice types, and throughout this dissertation, I will use it to distinguish young ice from old ice [*WMO,* 1970; *Johnston and Timco,* 2008]. By formal definition, sea ice that has not yet survived one summer is first-year (FY) sea

ice, while ice that has survived more than two summer melt seasons is multiyear (MY) ice [*WMO*, 1970; *Johnston and Timco,* 2008].

Figure 1.1 First-year (**left**) and multiyear (**right**) sea ice in the Beaufort and Chukchi seas in late July, 2011. Note that MY ice has rougher surface topography, which limits the spread of melt ponds compared to undeformed, smooth FY sea ice.

Despite being composed of the same material, FY and MY ice differ considerably in their dynamic and thermodynamic properties [*Untersteiner,* 1986]. These differences result from the time-dependency of sea ice morphology and its physical makeup [*Perovich et al.,* 2001]. MY sea ice has had more opportunities to undergo deformation events, summer meltwater flushing, and winter growth, so it is often thicker, fresher, and more deformed than FY sea ice. Here, we give an overview of two key differences between FY and MY ice and their effects on the ice mass balance of the Arctic sea ice cover.

The most striking difference between FY and MY ice in a setting that contains both is the disparity in thickness. FY sea ice is typically about a third-to-half of the thickness of MY ice [*WMO,* 1970; *Untersteiner,* 1986; *Johnston and Timco,* 2008]. Because it is thinner, FY sea ice is

more susceptible to ocean and atmospheric forcings, allowing more momentum transfer from surface winds [*Thorndike and Colony,* 1982; *Guest and Davidson,* 1991; *Rampal et al.,* 2009], farther wave propagation into the sea ice pack [*Wadhams,* 1986; *Squire et al.,* 2009; *Doble et al.,* 2015], and greater ocean mixing [*Rainville and Woodgate,* 2009; *Martin et al.,* 2014]. In winter, the presence of FY sea ice modifies the surface heat balance by increasing the amount of oceanic heat flux through the ice cover to the cooler atmosphere [*Maykut and Untersteiner,* 1971; *Maykut,* 1982]. In summer, FY sea ice decreases the survivability of the sea ice pack because less heat is required to melt less of the sea ice.

The ice mass balance of the Arctic sea ice pack is also influenced by the level of deformation of the sea ice itself. Overall, FY sea ice is less deformed than MY ice because it has had less time to undergo deformation and weathering [*WMO,* 1970; *Johnston and Timco,* 2008]. In winter, the smooth surface topography of FY ice allows snow to drift across it more readily, creating a thinner, more uniform snow cover [*Sturm et al.,* 2002]. A thin snow cover melts faster and earlier [*Perovich,* 2007; *Webster et al.,* 2015], which exposes sea ice to solar radiation sooner in the spring season. As surface melt begins and the meltwater pools to form melt ponds, the level topography of FY ice allows melt ponds to spread laterally to encompass a relatively larger area of the ice surface [*Fetterer and Untersteiner,* 1998*; Perovich et al.,* 2002b; *Webster et al.,* 2015]. High areal melt pond fractions, in turn, reduce the surface albedo [*Perovich et al.,* 2007; *Perovich and Polashenski,* 2012], increasing solar absorption and transmission [*Nicolaus et al.,* 2012; *Light et al.,* 2015] and accelerating surface and bottom melt of the sea ice cover.

Ample evidence has shown that the Arctic sea ice pack is shifting away from its composite makeup and trending towards a dominant sea ice type: first-year sea ice (Figure 1.2A) [*Rigor and Wallace,* 2004; *Nghiem et al.,* 2007; *Maslanik et al.,* 2011]. The average thickness of the Arctic

sea ice pack has halved [*Kwok and Rothrock,* 2009; *Laxon et al.,* 2013; *Lindsay and Schweiger,* 2015], and its areal extent has decreased to approximately four million square kilometers in summer (Figure 1.2B) [*Stroeve et al.,* 2007, 2012]. In essence, the Arctic sea ice pack is becoming a seasonal sea ice cover, with the first ice-free September for the Arctic Ocean projected to occur in 2100 [*Stocker et al.,* 2013].

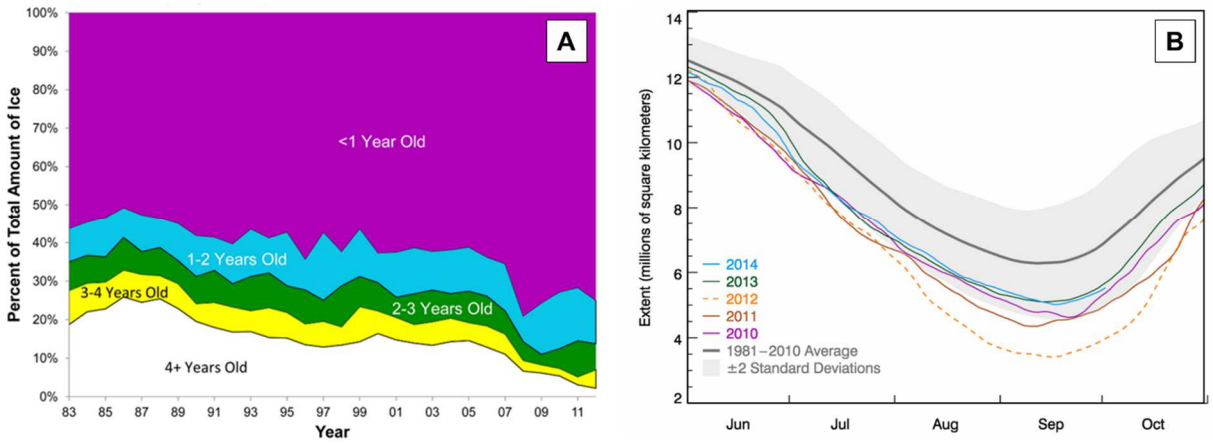

Figure 1.2 (A) Sea ice age as a percentage of the total sea ice extent (*J. Maslanik, National Snow and Ice Data Center and M. Tschudi, University of Colorado, accessed on 8 June 2016 at http://nsidc.org/arcticseaicenews/tag/ice-age/*). **(B)** Minimum September sea ice extent from passive microwave satellite data using a 15% sea ice concentration threshold (*National Snow and Ice Data Center, accessed on 8 June 2016 at http://nsidc.org/arcticseaicenews/2014/09/arctic-minimum-reached/*).

The implications of these changes to the Arctic and global ocean systems are numerous [*Lindsay and Zhang,* 2005; *Holland et al.,* 2006; *Vihma,* 2014]. For the Arctic Ocean, the absence of summer sea ice creates a positive ice-albedo feedback [*Maykut and Untersteiner,* 1971; *Curry*

et al., 1995]. With an increasing absence of sea ice during summer, ~93% of the incoming solar radiation is absorbed by open water, which by comparison, is over twice as much solar absorption by sea ice [*Perovich et al.,* 2007; *Perovich and Polashenski,* 2012]. As more solar absorption occurs, the remaining sea ice floes experience greater bottom melt [*Perovich et al.,* 2011] and the ocean heat content increases [*Steele et al.,* 2008]. In autumn, this increase in ocean heat content delays the formation of new sea ice [*Markus et al.,* 2009], as more time is required to cool the surface ocean sufficiently to allow freezing to occur. This cascading effect has influenced the timing and magnitude of the seasonal cycle of the Arctic sea ice pack, and will likely continue to transform it into a younger, thinner, more seasonal sea ice cover [*Lindsay and Zhang,* 2005; *Holland et al.,* 2006].

In this dissertation, I focus on the impacts of the changing Arctic sea ice cover on three geophysical properties of its surface: snow, melt ponds, and surface topography. The objective is to increase understanding of the interdecadal change in snow depth on sea ice, the role of snow distribution in seasonal melt pond evolution, and the spatial scaling of melt pond distributions, all with respect to the increasing trend in first-year sea ice in the Arctic. Following the specific studies of these geophysical properties of the sea ice surface, presented in Chapters 2–4, Chapter 5 concludes with the implications of the overall findings in the broader context of climate change and feedbacks within the Arctic system.

1.3 CHAPTER SUMMARIES

Chapter 2. A study was conducted on the distribution of snow on sea ice in the western Arctic during spring. Measurements from contemporary years were compared to the 1954–1991 climatology to assess the interdecadal changes in spring snow depth distribution. The results show that snow thickness has decreased, with the greatest decrease occurring in the marginal seas. The decrease was correlated with the trend in later sea ice formation during autumn, which coincides with the period of maximum snowfall. These results suggest that autumn snow increasingly falls directly into the surface ocean and melts, given the absence of a sea ice platform, which reduces the annual snow accumulation.

Chapter 3. Seasonal melt pond evolution was investigated on drifting Arctic sea ice. An algorithm was developed to analyze high-resolution satellite imagery for melt pond fractions at a Lagrangian site composed of first-year and multiyear sea ice. Melt ponds formed first on multiyear sea ice and three weeks later on first-year sea ice. The timing offset was attributed to an unusually thin snow cover on multiyear sea ice; nearly half of the multiyear snow was ten centimeters or thinner, which is a thickness range considered to be optically thin. Uniformity in melt pond distribution and seasonal evolution decreased with increasing sea ice surface roughness.

Chapter 4. The spatial scaling of melt pond distributions was investigated at two sites with homogenous (undeformed first-year) and heterogeneous (mixed deformation and age) sea ice by examining the link between small-scale variability in melt pond geometry and aggregate-scale estimates of melt pond fractions. The results revealed that: (1) melt pond geometry is most variable

during maximum coverage before pond drainage at the heterogeneous site, but after pond drainage at the homogenous site, (2) aggregate-scale estimates of melt pond fractions in homogenous and heterogeneous sea ice sites are larger than previously recognized, and (3) aggregate-scale estimates of melt pond fractions may be dependent on the composition of sea ice types and stage of melt pond evolution.

Chapter 2. Interdecadal Changes in Snow Depth

ABSTRACT

Snow plays a key role in the growth and decay of Arctic sea ice. In winter, it insulates sea ice from cold air temperatures, slowing sea ice growth. From spring into summer, the albedo of snow determines how much insolation is absorbed by the sea ice and underlying ocean, impacting ice melt processes. Knowledge of the contemporary snow depth distribution is essential for estimating sea ice thickness and volume, and for understanding and modeling sea ice thermodynamics in the changing Arctic. This study assesses spring snow depth distribution on Arctic sea ice using airborne radar observations from Operation IceBridge for 2009–2013. Data were validated using coordinated in situ measurements taken in March 2012 during the BRomine, Ozone, and Mercury EXperiment (BROMEX) field campaign. We find a correlation of 0.59 and root-mean-square error of 5.8 cm between the airborne and in situ data. Using this relationship and IceBridge snow thickness products, we compared the recent results with data from the 1937, 1954–1991 Soviet drifting ice stations. The comparison shows thinning of the snow pack, from 35.1 ± 9.4 cm to 22.2 ± 1.9 cm in the western Arctic, and from 32.8 ± 9.4 cm to 14.5 ± 1.9 cm in the Beaufort and Chukchi seas. These changes suggest a snow depth decline of 37 ± 29% in the western Arctic and 56 ± 33% in the Beaufort and Chukchi seas. Thinning is negatively correlated with the delayed onset of sea ice freeze-up during autumn.

2.1 INTRODUCTION

The Arctic is undergoing unprecedented change [*Overpeck et al.,* 2005; *National Academies,* 2012]. The trend in sea ice extent is decreasing at an accelerated rate [*Stroeve et al.,* 2012], and there has been a shift from thick, multiyear ice to a thinner, younger sea ice regime [*Nghiem et al.,* 2007; *Kwok and Rothrock,* 2009; *Maslanik et al.,* 2011]. This shift has profoundly affected the state of Arctic sea ice, which has become more dynamic and susceptible to melt, changing the ice volume [*Laxon et al.,* 2013], ocean heat flux [*Perovich et al.,* 2007], surface albedo [*Perovich and Polashenski,* 2012], and snow cover [*Hezel et al.,* 2012].

Snow on sea ice plays a key role in sea ice thermodynamics [*Maykut and Untersteiner,* 1971; *Maykut,* 1986; *Blazey et al.,* 2013]. Depending on snow thickness, distribution, and density, it can help recover the sea ice pack, or exacerbate its loss. During the spring, snow thickness limits how much transmittance and absorption of solar energy can occur within the sea ice and underlying ocean [*Perovich and Polashenski,* 2012]. Thick snow may withstand melt and maintain a high surface albedo throughout the summer melt period [*Eicken et al.,* 2004]. Conversely, meltwater from snow creates a superimposed ice layer that facilitates the formation of melt ponds [*Eicken et al.,* 2004; *Petrich et al.,* 2012], which absorb 1.7 times more solar radiation than bare sea ice and 5 times more than cold, snow-covered sea ice [*Perovich and Polashenski,* 2012; *Perovich et al.,* 2002a]. Earlier onset of Arctic sea ice melt has been documented [*Markus et al.,* 2009], and likely contributes to earlier spring phytoplankton blooms and shifts in sympagic-based ecosystems [*Arrigo et al.,* 2008; *Wassmann et al.,* 2010; *Grebmeier et al.,* 2012]. In cases with no snow, melt pond formation can be inhibited due to the absence of a superimposed ice layer [*Eicken et al.,* 2004].

While a decreasing trend has been reported in most terrestrial regions [*IPCC,* 2013], interdecadal changes of snow depth on Arctic sea ice have not been adequately addressed. A past climatology of snow on Arctic sea ice was developed in the study by Warren et al., 1999, hereafter referred to as W99, which used extensive field data from the Soviet drifting ice stations in 1937 and 1954-1991. W99 spring snow depths ranged from a few centimeters on young sea ice to over 40 cm on multiyear sea ice. These values may not be representative of the current conditions of the snow cover [*Kurtz and Farrell,* 2011], and likely contribute to uncertainties in current sea ice thickness and volume estimates [*Laxon et al.,* 2013]. Thus, contemporary conditions of snow thickness distribution on Arctic sea ice need to be assessed and reported. This has become particularly important in view of the regime shift of Arctic sea ice to younger thinner ice, which is more susceptible to thermodynamic forcings, emphasizing the greater role of snow thickness in sea ice growth and melt than in earlier decades [*Maykut*, 1986].

Obtaining high-resolution measurements of snow thickness distribution on Arctic sea ice has been challenging. Traditional, in situ observations are limited spatially. More recently, remote-sensing data have become available for the analysis of regional snow thickness. Validation of the accuracy of both airborne and satellite snow depth estimates is required [*Farrell et al.,* 2012; *Brucker and Markus,* 2013], and remains the subject in a number of on-going studies. In this study, we present a new assessment of the spring snow thickness distribution on Arctic sea ice using airborne and in situ measurements at the highest spatial resolution scale currently available. Coordinated in situ snow depth measurements from the BRomine Ozone Mercury EXperiment (BROMEX) campaign in March 2012 [*Nghiem et al.*, 2013] were used to validate the IceBridge standard and quick-look snow thickness products. The validated snow thickness products were then used to produce an updated climatology of spring snow depth distribution on sea ice in the

western Arctic, and quantify the change in snow depth in recent years via comparison with the W99 climatology.

2.2 DATA

2.2.1 *IceBridge airborne data*

The Operation IceBridge standard snow depth product was the primary dataset used in this study. These data are publicly available on the National Snow and Ice Data Center (NSIDC) website (http://nsidc.org/data/idcsi2) and form part of the "IceBridge Sea Ice Freeboard, Snow Depth, and Thickness Product" [*Kurtz et al.,* 2012]. Between 2009 and 2013, Operation IceBridge conducted 45 flights in March and April, before the onset of melt, measuring snow thickness on Arctic sea ice (Fig. 2.1). The snow thickness was measured with the University of Kansas' ultra-wideband frequency-modulated continuous wave (FMCW) snow radar using the 2–8 GHz frequency range [*Leuschen,* 2009]. The snow radar pulse-limited footprint is approximately 14.5 m along-track and 11 m across-track on level sea ice for the nominal flight altitude; the radar echoes are stacked in the snow depth retrieval algorithm to reduce speckle noise, which lessens the along-track resolution to 40 m.

The snow radar has been continually changed and improved, with larger bandwidth and higher signal-to-noise ratio (SNR) [*Panzer et al.,* 2013]. The radar bandwidth determines the range resolution, which is five centimeters for 2009–2011, and four centimeters for 2012–2013 [*Panzer et al.,* 2013; *Kurtz et al.,* 2013b]. The snow depth retrieval algorithm was updated to account for changes in the SNR. Subsequently, two algorithms are now used, one to account for the low SNR during the 2009 campaign, and one to adapt to the changing SNR in the 2010 and later campaigns

[*Kurtz et al.,* 2013b]. Due to these continual changes, repeat validation is required to ensure accuracy of the retrieval algorithms. Currently, the uncertainty associated with the IceBridge snow depth product is 5.7 cm based on comparisons with in situ data gathered in April 2009 [*Kurtz et al.,* 2013b].

Since 2012, IceBridge has provided a quick-look data product within approximately one month of acquisition to facilitate use of the data for seasonal forecasting of the Arctic sea ice cover [*Kurtz et al.,* 2013]. The main differences between the snow radar standard product and quick-look product are the use of lower quality Global-Positioning-System trajectory data and noise reduction techniques for the field-processed quick-look data. Quantifying the differences in the standard and quick-look data can be done by comparing the two datasets. For the snow depth data, this was done by first gridding the output data from the snow radar to a 25 km polar stereographic grid and examining statistics of the differences. The quick-look data for 2012 was very consistent with the standard data product, with a mean difference as small as 0.05 cm, and standard deviation of differences of two centimeters. There was also no discernible spatial pattern in the differences. For 2013, the mean difference was 1.6 cm and the standard deviation of differences was 2.4 cm. The overall differences were small; however, there was a strong spatial pattern to the differences in multiyear ice areas north of Greenland and Canada, which had several centimeters less snow than the standard data product.

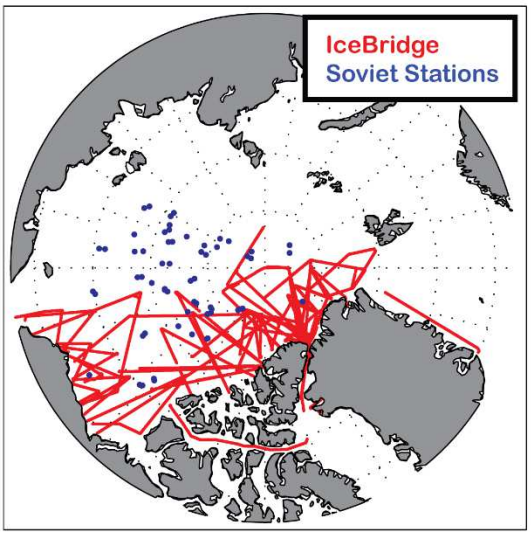

Figure 2.1 Locations of the 2009-2013 Operation IceBridge flights measuring snow depth (red lines) and 1937, 1954–1991 Soviet station (blue dots) during March and April.

2.2.2 *In situ data*

Coordinated in situ snow depth measurements were made during the BROMEX field campaign [*Nghiem et al*., 2013] to validate the IceBridge quick-look and standard snow thickness products. On 15 March 2012, the NASA P-3B aircraft, carrying the Operation IceBridge instrument suite, flew an east-west transect at ~460 m altitude in clear and calm conditions over the BROMEX field site near Barrow, Alaska. These conditions persisted throughout the week as ground-based snow depth measurements were carried out in temperatures ranging from -36.0 ˚C to -30.1 ˚C with wind speeds of 2.7 m s^{-1} to 5.0 m s^{-1} (http://www.esrl.noaa.gov/gmd/dv/). No significant blowing snow events were observed throughout the week of field measurements.

Two ground-truth transects were made underneath the flight path on Elson Lagoon, an area consisting of relatively level, undeformed first-year sea ice covered by drifted snow (Fig. 2.2). The standard deviation of the sea ice thickness was less than 15 cm. Snow depths were measured every one-to-five meters using a Snow-Hydro© Automated Snow Depth Probe, or "MagnaProbe," which has an accuracy of ± 0.3 cm on level sea ice and snow. Snow density was measured every ~30 m with a "Federal Sampler" [*Marr,* 1940]. The first transect consisted of three lines approximately 1000 m in length, each five meters apart, for a width of ten meters. The second transect included five lines roughly 400 m in length, five meters apart, for a width of 20 m.

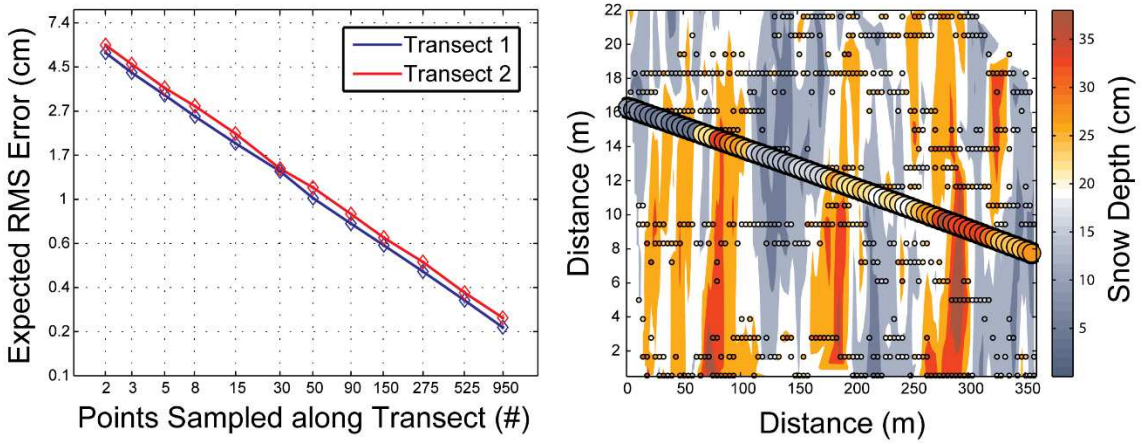

Figure 2.2 Left panel: The RMS error of Transects 1 and 2 on Elson Lagoon based on the number of points measured along the transect using a Poisson distribution after *Blanchet and Davidson* [2011] and W99. **Right panel:** An interpolation of the in situ data collected along Transect 2. In situ measurements are shown by small circles, and the IceBridge quick-look product by bold circles. The color of the circles corresponds to snow depth. Note the differing distance range for the axes.

The W99 climatology was used for comparison with the contemporary snow depth distribution from the IceBridge products. The analysis focused on March and April months, which we define as our spring study period, because this period offered the most data for comparison (Fig. 2.3). The W99 climatology consists of snow depth data from the Soviet Union's manned drifting ice stations in 1937, 1954–1991. The data are readily available at the NSIDC website [*Fetterer and Radionov,* 2000]. Each "North Pole" station was located on multiyear sea ice, and began its drifting trajectory from the central Arctic Ocean. During its drift, snow depth was measured every ten meters along the same 100-m snowline every ~10 days throughout the station's lifetime. The snowlines were located on variable surface topography, from level to ridged sea ice. The updated climatology was reproduced following W99.

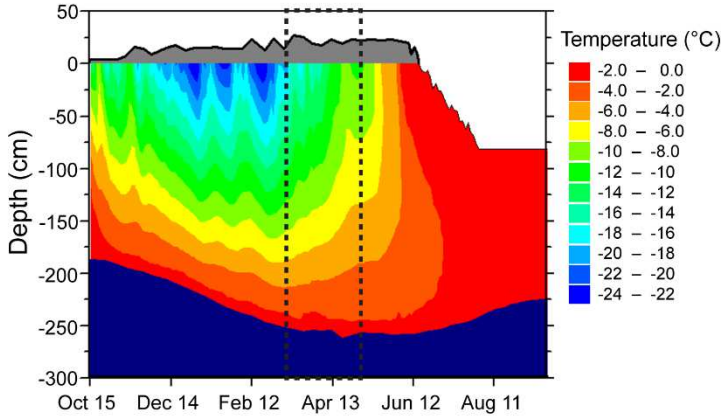

Figure 2.3 Temperature profiles, in Celsius, from an IMB buoy in a multiyear sea ice floe at the Surface Heat Budget of the Arctic Ocean (SHEBA) field campaign. Our analysis focuses on March and April months only, outlined by the highlighted dashed box, which is before the onset of melt.

Snow data from the Cold Regions Research and Engineering Laboratory's (CRREL) Ice Mass Balance (IMB) buoys [*Perovich et al.,* 2013] were also analyzed and compared to the W99 climatology. The IMB buoys are equipped with acoustic range-finders which measure the time between the transmitted signal from the sensor and backscattered signal from the surface, yielding the distance between the buoy sensor and air-snow interface [*Perovich et al.,* 2013]. Using the initial snow and sea ice thicknesses with the measured distances, we extracted information on the change in snow depth during the lifetime of each IMB buoy. The IMB buoys were deployed on both first-year and multiyear sea ice mainly in the western and central Arctic in 1993–2013, and new deployments are currently on-going.

2.2.3 *Satellite data*

The relationships between the reduced snow cover, snow accumulation rates, and sea ice freeze-up dates were evaluated using data from the Soviet stations, IMB buoys, and a freeze-up product derived from passive microwave satellite data [*Markus et al.,* 2009]. The sea ice freeze-up product covers the entire passive microwave record, 1979–2012, and is currently available on the Cryosphere Research Portal [http://neptune.gsfc.nasa.gov/csb/]. For the correlation analysis, we compared the average day of autumn freeze-up with the spring snow depth in corresponding areas for both periods.

2.3 METHODS

2.3.1 *In situ sampling*

To estimate the error associated with in situ data, subsets of varying size were randomly selected from the data and averaged. This iterative approach was performed 2000 times. The root-mean-square error was then calculated, providing the expected RMS error of the in situ data according to the number of snow depths measured. This method assumes a Poisson distribution, which has been used in snow depth modeling [*Blanchet and Davidson*, 2011] and in W99. For an average of 16 in situ measurements per snow radar footprint, the expected error was 1.4 cm. The slopes of the first few point-measurements in both transects were approximately -0.5, indicating that the one-to-five-meter spaced measurements were independent of each other (Fig. 2.2). Transects 1 and 2 have similar fitted lines in Figure 2.2, indicating that both transects were consistently sampled and that the snow depth distributions were not significantly different between the transects. For the validation analysis, all in situ point measurements within the snow radar footprint were averaged and compared to the IceBridge snow thickness products. No outliers were removed from the in situ or IceBridge datasets. A robust least square cubic regression line was fitted to the data to account for a varying error in the in situ averages and a constant 5.7 cm uncertainty in the IceBridge products.

2.3.2 *Snow depth interpolation*

In order to assess the springtime snow depth distribution from the 2009-2013 IceBridge snow thickness products, we used the same method of W99. A least squares solution was found for the two-dimensional quadratic equation using rectangular coordinates, defined by

$$H = H_o + Ax + By + Cxy + Dx^2 + Ey^2 \quad (2.1)$$

where H_o is the snow depth at the North Pole, x and y are rectangular coordinates converted from latitudes and longitudes using the Equal-Area Scalable Earth Grid (EASE-Grid) map projection [*Knowles,* 1993], and *A, B, C, D,* and *E* are coefficients. Once the solution was found, snow depth was interpolated between data points, producing a snow depth distribution for a given region based on the dataset used.

In W99, gridded averages of Soviet drifting ice station data were used when solving for the least squares solution. We averaged the IceBridge snow thickness product by the same grids for consistency. There are differences between the locations of the Operation IceBridge flights, and the Soviet drifting ice stations. Thus, the analysis was limited to the western Arctic where both datasets overlap. RMS errors were calculated between the interpolated and gridded snow depths for comparison with the errors reported in W99.

The decadal change in spring snow depth was calculated using data from the Soviet drifting ice stations, the IMB buoys, and the IceBridge snow thickness product. These data span 1950–1987, 1993–2013, and 2009–2013, respectively. The anomaly was found by taking each point measurement minus the W99 multiyear average for that location. Each year's spring anomalies were averaged to produce the decadal change between 1950 and 2013.

2.3.3 *Accumulation rates*

Snow accumulation rates from the W99 climatology and the contemporary period were compared to assess whether snow accumulation rates have changed. Snow accumulation rates were defined as the monthly average snow depth minus the previous month's average snow depth. Although IMB buoy data exist from 1993 to the present, buoys from 2009–2013 were chosen for the accumulation analysis due to the temporal overlap with the 2009–2013 Operation IceBridge data.

2.4 RESULTS

2.4.1 *IceBridge validation*

The right panel of Figure 2.2 shows a three-dimensional comparison between the in situ point measurements, represented by small circles, and the IceBridge snow depth product, represented by bold circles. There is good agreement between the two datasets, and also between the IceBridge product and the in situ interpolation. On average, Transect 1 had 26 in situ point measurements within each snow radar footprint, while Transect 2 had 39 point measurements within each snow radar footprint, providing the most densely sampled ground-truth lines for Operation IceBridge to date.

Figure 2.4 shows the variation between the IceBridge quick-look and standard snow depth products and in situ averages along each transect. Overall, the patterns between the in situ and IceBridge datasets agree well, and the differences between their averages are within the estimated uncertainties. The RMS error between the IceBridge quick-look product and the in situ averages

was 5.8 cm, comparable to the estimated uncertainty of 5.7 cm for the 2009–2011 IceBridge snow depth products [*Kurtz et al.,* 2012].

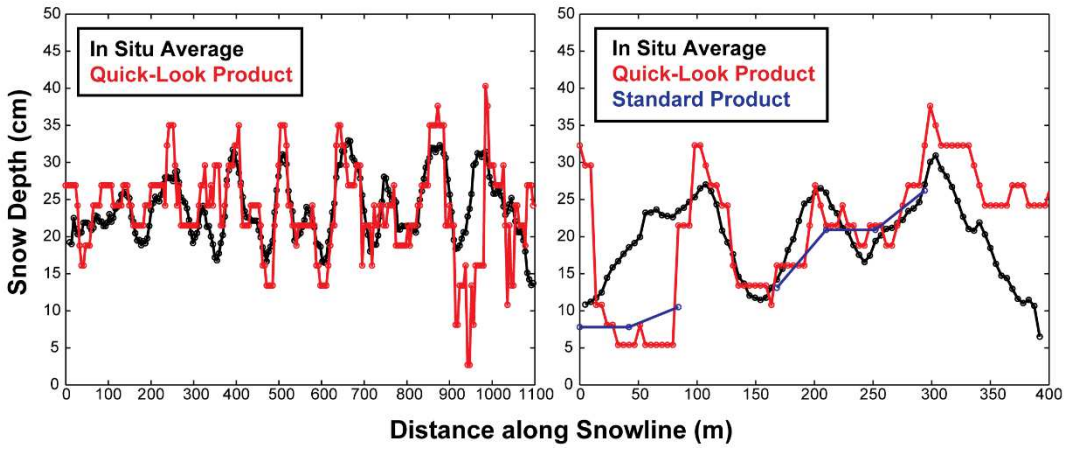

Figure 2.4 Comparisons between the in situ averages (black), the IceBridge quick-look snow depth product (red), and, where available, the IceBridge standard product (blue) along Transects 1 (**Left panel**) and 2 (**Right panel**). Transects 1 and 2 were ~1000 m and ~400 m in length, respectively.

However, the IceBridge product appears to underestimate thin snow depths in comparison to the in situ averages, and a clear discrepancy can be seen around 50 m along Transect 2 (Fig. 2.4); this discrepancy is also apparent in the scatter plot (Fig. 2.5) where the IceBridge quick-look and standard products estimate a snow thickness of roughly five-to-eight centimeters while the in situ mean is ~23 cm. It is unclear why this low bias exists. The value of snow density used in the IceBridge retrieval algorithm is 320 kg m^{-3}, while the measured snow density along the two transects was 332 ± 13 kg m^{-3}. This density difference leads to a ~0.1 cm snow depth difference, which is not enough to explain the bias nor why the bias is most prominent at low snow values. An examination of the radar echogram in the low areas shows the chosen snow-ice interface was

smooth and consistent over this region, but the backscatter was low compared to the surrounding ice (Fig. 2.6). At a distance of 350 m–400 m along Transect 2, the high IceBridge snow depth estimates are likely due to the presence of coherent noise in the radar data.

In short, the above data demonstrate that the IceBridge snow depth product can accurately measure snow depth on level, undeformed sea ice, but the anomalies also underscore the need for more validation efforts to fully resolve the sources of error in snow depth estimates over different sea ice types and roughness conditions. Considering the good agreement between the IceBridge products and in situ data, we use a one-to-one relationship for estimating snow depth distributions in the western Arctic.

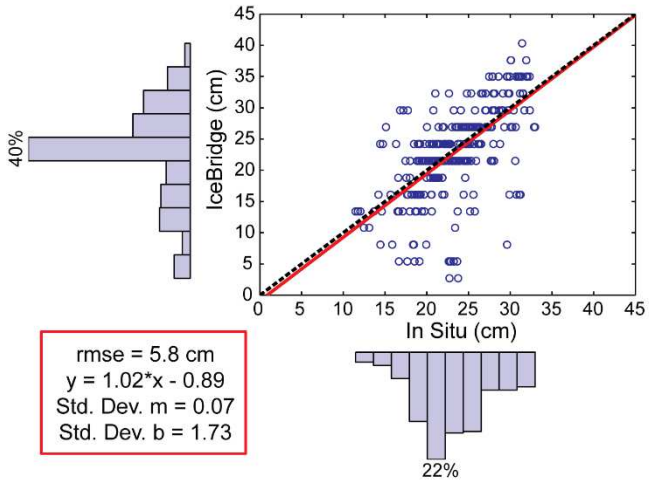

Figure 2.5 The least squares cubic regression (red line) between the IceBridge quick-look data (y-axis) and the in situ averages (x-axis). The one-to-one line is shown by the black dashed line. Both histograms have ten bins, and the values of the largest bins are a percentage of the normalized distributions.

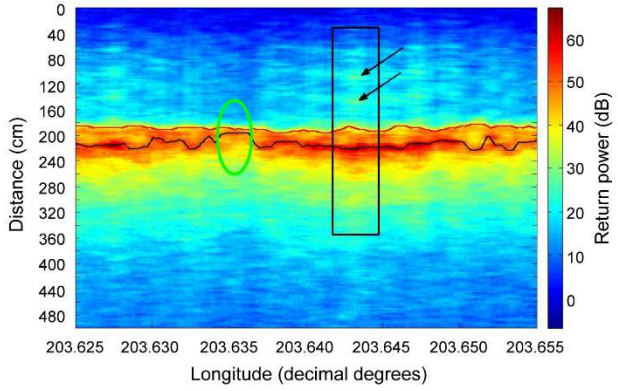

Figure 2.6 The radar echogram of Transect 2. The red line is the chosen snow-air interface and the chosen black line is the chosen snow-ice interface. The area with the green circle shows the ~0–100 m region of Transect 2 where thin snow depths were identified. The black box area shows where thick snow depths were chosen, and the arrows point to the presence of coherent noise in the radar data.

2.4.2 *Comparison with climatology*

The spring snow depth distributions estimated from the IceBridge and the Soviet station datasets using equation 2.1 are shown in Figure 2.7, along with their point measurements. There is a marked decrease in snow thickness spanning the western Arctic in 2009–2013 compared to the 1937, 1954–1991 climatology. An average snow depth of 35.1 ± 9.4 cm was observed in the W99 climatology for the western Arctic; the 2009-2013 average was 22.2 ± 1.9 cm, suggesting a thinning of 37 ± 29% (Fig. 2.7). The Beaufort and Chukchi seas exhibited the greatest change, having thinned by approximately 56 ± 33% (Fig. 2.8). The RMS error between the 2009-2013 in situ and interpolated snow depths was 1.9 cm, and significantly lower than the reported error of 9.4 cm in the W99 climatology. The decadal change in spring snow depth revealed a trend of -0.29

cm per year with 99% significance (Fig. 2.9). In comparison, the largest trend found by W99 was approximately -0.10 cm per year for May, the month of maximum snow depth, in 1950–1991. The negative trend was attributed to a possible decrease in precipitation [W99].

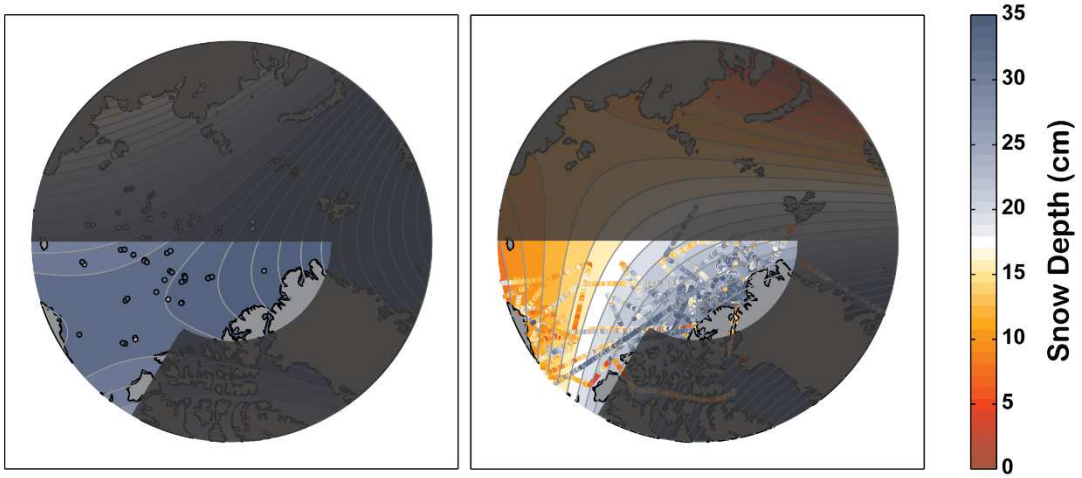

Figure 2.7 The snow depth distribution resulting from the two-dimensional quadratic equation (Equation 2.1) fitted to the 1937, 1954–1991 Soviet drifting ice station data (**Left panel**) and the 2009–2013 IceBridge snow depth products (**Right panel**) for March and April. Point measurements are indicated by the small circles; snow depths are indicated by color. The grey shading indicates areas where no data are available.

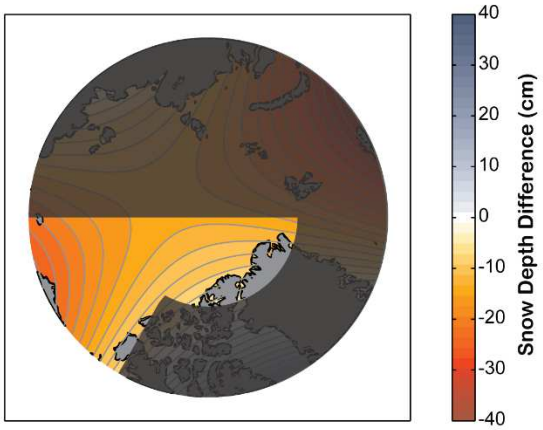

Figure 2.8 The difference between the 2009–2013 IceBridge snow depth distribution and the W99 climatology. Red indicates that the snow cover has thinned compared to the W99 snow climatology, white indicates no change in snow depths, and blue represents an increase. The grey shading indicates areas where no data are available.

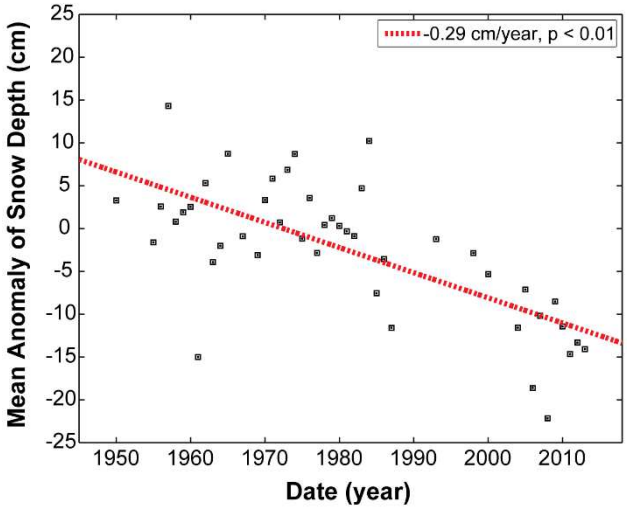

Figure 2.9 The decadal change in snow depth in spring. The anomalies were calculated using data from Soviet drifting ice stations (1950–1987), Ice Mass Balance buoys (1993–2013), and the Operation IceBridge snow depth products (2009–2013). The anomaly is the measurement minus

the W99 multiyear average in spring at that location. The average of the anomalies for each year is shown by black squares, and the red line represents the trend in centimeters per year. For measurements within the western Arctic only, the trend was -0.27 cm per year with 99% significance.

According to *Kurtz and Farrell* [2011], IceBridge snow depth measurements for 2009 were 52% thinner in areas of first-year sea ice than the 1937, 1954–1991 climatology. Our findings also show thinner snow depths in the Beaufort and Chukchi seas, where much of the sea ice is younger [*Richter-Menge and Farrell,* 2013] and later sea ice freeze-up dates have been observed [*Markus et al.,* 2009]. A modeling study by *Hezel et al.,* [2012] projected snow depths on Arctic sea ice using the first-order effects of sea ice freeze-up dates and precipitation rates. There was good agreement between the IceBridge and modeled snow depth distributions in the western Arctic, both in space and magnitude. The 2009-2013 IceBridge average was 22.2 ± 1.9 cm, while the modeled 1981–2000 and 2081–2100 averages were 28 ± 7 cm and 16 ± 5 cm, respectively [*Hezel et al.,* 2012].

2.4.3 *Accumulation and sea ice freeze-up*

While there are numerous processes that affect spring snow thickness on Arctic sea ice, snow accumulation rates and the timing of sea ice freeze-up directly affect spring snow thickness the most; they are considered to have first-order effects on snow depth [*Radionov et al.,* 1997; *Hezel et al.,* 2012]. The comparison between the CRREL IMB buoy and the Soviet ice station data showed no significant changes in monthly snow accumulation rates, with the exception of April

(Fig. 2.10). In April, the Soviet station and IMB buoy data yielded accumulation rates of 3.3 ± 1.1 cm per month and 0.6 ± 0.4 cm per month, respectively. The differences in accumulation rates for all other months were smaller than their standard errors (Fig. 2.10). Note that the large standard errors in the IMB buoy data are due to the sample size rather than the quality of the buoy data; there were 8–17 IMB buoys per month for 2009–2013. The maximum snow accumulation rates for the Soviet station and IMB buoy data occurred in September, and were 6.5 ± 1.7 cm per month and 7.5 ± 2.0 cm per month, respectively. The differences in snow accumulation rates, particularly the maximum rates, were not large enough to explain the observed decrease in snow depths across the western Arctic. In addition, the annual snow accumulations from the Soviet drifting ice stations and the IMB buoys were comparable with values of 30.1 ± 3.2 cm and 28.5 ± 3.9 cm, respectively (Fig. 2.10). These results were also consistent with multiple reanalysis products showing no trend in the 1981–2010 annual precipitation for our region of study [*Lindsay et al.,* 2014].

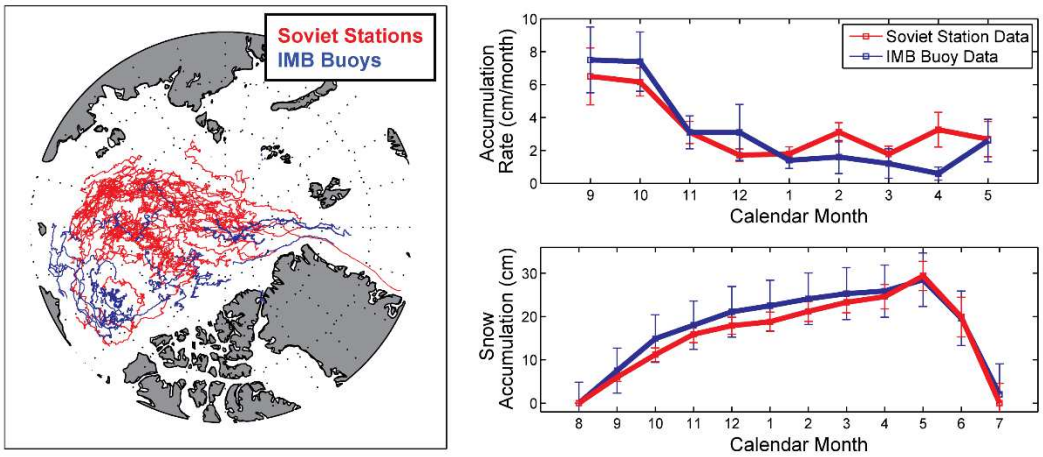

Figure 2.10 Left panel: The locations of the CRREL Ice Mass Balance buoys (blue) and Soviet drifting ice stations (red). **Top Right panel:** The average monthly snow accumulation rate

according to Ice Mass Balance buoy data (blue) and the Soviet drifting ice stations snowline data (red). Rates and their standard errors are given in centimeters per month (y-axis), and the months are given by calendar number beginning with September (x-axis). **Lower Right panel:** Snow accumulation as a function of time, with Soviet station data in red and IMB buoy data in blue.

Because maximum snow accumulation rates occur in September and sea ice freeze-up is now trending later in autumn in this region [*Markus et al.,* 2007], snow falls directly into the ocean until sea ice forms, resulting in a thinner, cumulative snow cover. The results of sea ice freeze-up dates and snow thickness distributions for the 2009–2013 and 1937, 1954–1991 periods are shown in Figure 2.11. The upper plots represent the 2009–2013 period with sea ice freeze-up in the left panel and snow depth distribution in the right panel. We found a good spatial match between sea ice freeze-up and snow thickness distribution, with a correlation coefficient of -0.68. The strong correlation indicates that the delay in sea ice freeze-up may significantly contribute to the decrease in snow depth. Because the correlation coefficient is not exactly -1.0, it also indicates that other factors play a role, such as changes in atmospheric patterns, sea ice motion and deformation, snow lost to leads, and wind-driven snow redistribution. The Beaufort and Chukchi seas exhibit later sea ice freeze-up and thinner snow depths, which is consistent with the shift to younger sea ice types in this region [*Nghiem et al.,* 2007; *Maslanik et al.,* 2011]. The Lincoln Sea, being mostly composed of multiyear sea ice, has the earliest freeze-up and the thickest snow depths. The lower plots show the 1937, 1954–1991 period of sea ice freeze-up and snow thickness distribution. The sea ice freeze-up and snow thickness distribution had a correlation coefficient of -0.23 for the 1979–1991 period. Note that sea ice freeze-up for this period was calculated based on the available

satellite passive microwave record from 1979–1991, and the lack of data prior to 1979 might possibly contribute to the low correlation.

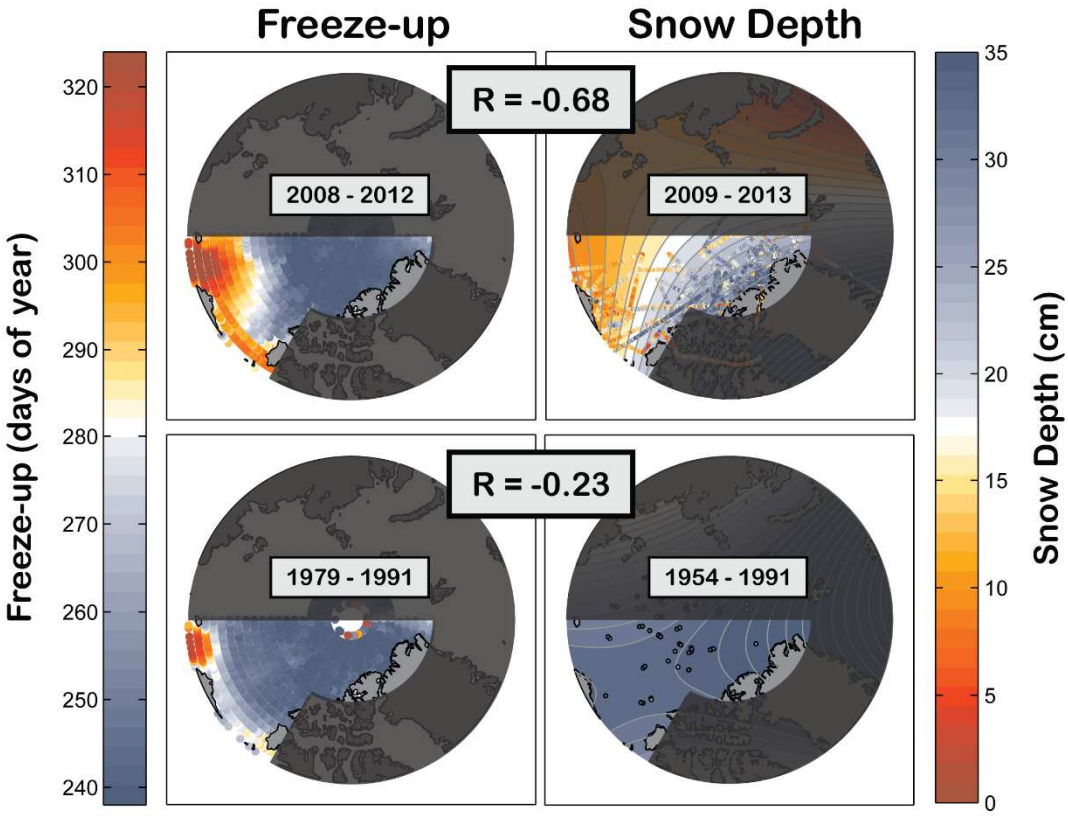

Figure 2.11 The correlations between sea ice freeze-up dates (left panels) and snow depth distributions (right panels) for the 2009–2013 and 1954–1991 periods. Later freeze-up dates are represented by red shading while earlier freeze-up dates are represented by blue shading. Note that freeze-up dates are given in Days of Year, and ranges from approximately late August to late November. **Upper left**: Sea ice freeze-up dates for the 2008–2012 period. **Upper right**: Snow depth distribution according for the 2009–2013 period. **Lower left**: Sea ice freeze-up dates for the 1979–1991 period. **Lower right**: The W99 snow depth climatology.

While earlier melt onset has substantial effects on the surface albedo and progression of melt in late spring and early summer, it does not impact the spring snow thickness as much as the timing of sea ice freeze-up. The melt onset occurs in June for the western Arctic and late May for the Beaufort and Chukchi seas in 2009–2013 [*Markus et al.,* 2009]. If we subtract the May accumulations (Fig. 2.10) due to melt from the total accumulation, and separately, subtract September accumulations due to later freeze-up from the total, the loss of snow in September is larger than the loss in May, indicating that September snow loss due to delayed freeze-up has a greater impact on the cumulative snow accumulation than the snow loss in May due to earlier melt onset. Our study focuses on the March and April period, which is before the onset of melt in this region for both periods [*Markus et al.,* 2009].

Using the freeze-up product and IMB and W99 accumulation rates, we found that later freeze-up dates may explain the magnitude of decrease in snow depth shown in Figures 2.8 and 2.9. On average for the 2008–2012 period, the continual freeze-up occurred on September 18 for the western Arctic, and October 22 for the Beaufort and Chukchi seas. Taking the monthly snow accumulation (Fig. 2.10), dividing it by the number of days pertaining to the month, we get an accumulation per day for the corresponding month. The delay in sea ice freeze-up results in a 4.5 cm ± 1.2 cm total loss in the western Arctic, and a 12.8 cm ± 2.4 cm total loss in the Beaufort and Chukchi seas. These results are consistent with and within the errors of the differences between the W99 and IceBridge results: 12.9 cm ± 9.6 cm for the western Arctic, and 18.3 cm ± 9.6 cm for the Beaufort and Chukchi seas. When taking into account that snow accumulation is greatest during the early autumn, the delay in freeze-up appears to have a significant impact on spring snow thickness on sea ice in the western Arctic.

2.5 DISCUSSION

We assessed the significance of a thinner snow cover on winter surface heat fluxes for a variety of ice types representative of the W99 and 2009–2013 periods and assumed mid-December conditions for sea ice thicknesses, air temperature, under-ice temperature and snow densities in the Beaufort and Chukchi seas (Table 2.1). Based on the IceBridge snow thickness distribution for 2009–2013, the Beaufort and Chukchi seas have an average snow depth of 14.5 cm in spring. A mid-December snow depth can be estimated by subtracting the cumulative snow accumulation based on the monthly snow accumulation rates. Using the IMB buoy accumulation rates, the total snow accumulation between mid-December and the end of March was 5.8 ± 2.2 cm, yielding a mid-December snow depth of 8.8 ± 2.9 cm in the Beaufort and Chukchi seas.

Table 2.1 Mid-December estimates[a]

	Young ice (2009–2013)	**Young ice (1954–1991)**	**First-year ice (1954–1991)**	**Multiyear ice (1954–1991)**
Ice Thickness (m) [Reference]	0.75 [*Schweiger et al.,* 2012]	1.2 [*Thorndike et al.,* 1975]	1.4 [*Kwok and Cunningham,* 2008]	3 [*Kwok and Cunningham,* 2008]
Snow Density (kg m^{-3}) [Reference]	290 [*Kwok and Cunningham,* 2008]	300 [W99; *Kwok and Cunningham,* 2008]	300 [W99]	300 [W99]
December Snow Depth (m)	0.088 ± 0.029	0.287 ± 0.094	0.287 ± 0.094	0.287 ± 0.094
Surface Heat Flux (W m^{-2})	79–85	43–49	39–43	20–22

[a]Ice thicknesses, snow densities, December snow depths, and the resulting surface heat fluxes for varying ice types in mid-December conditions assuming an air temperature of -34°C and under-ice temperature of -1.8°C [*Maykut and Untersteiner,* 1971; *Maykut,* 1978].

To find the surface heat flux, the thermal heat conductance of the sea ice and snow cover was calculated first. The thermal heat conductance was determined using

$$\gamma = k_i k_s / (k_s H + k_i h) \tag{2.2}$$

where γ is the thermal heat conductance (W m^{-2}°C^{-1}), k_i is the conductivity of the top of the sea ice and a constant of 2.14 W m^{-2}°C^{-1} [*Maykut,* 1978; *Pringle et al.,* 2006], and k_s is the conductivity of the snow, estimated as a function of snow density following *Sturm et al.* [1997]. The surface heat flux was then calculated as a function of the thermal heat conductance and the vertical temperature gradient as shown in

$$F_c = \gamma (T_b - T_0) \quad (2.3)$$

where F_c is the surface heat flux, γ is the thermal heat conductance found in equation (2.2), T_b is the temperature at the bottom of the sea ice, and T_0 is the temperature at the surface of the snow. The resulting surface heat flux through 0.75 m-thick sea ice and 8.8 ± 2.2 cm-thick snow cover was ~79–85 W m^{-2}. Applying the W99 snow climatology and accumulation rates, the W99 mid-December mean snow depth was 28.7 ± 9.4 cm, yielding a surface heat flux of ~43–49 W m^{-2} on young ice, ~39–43 W m^{-2} on first-year ice, and ~20–22 W m^{-2} on multiyear ice (Table 2.1).

The timespan between initial snow accumulation after sea ice freeze-up and mid-December is smaller in the 2009–2013 period compared to the 1954–1991 period, leaving less time for snow to densify. To explore the impact of lower bulk snow densities on surface heat fluxes, we performed a sensitivity study of snow density. Typically, snow density increases the fastest during the autumn when storms generate large snowfalls and wind-packing occurs [*Radionov et al.,* 1997; W99; *Sturm et al.,* 2002]. Bulk snow densities in the sensitivity study ranged from 200 kg m^{-3}, representing new and recent snow, to 300 kg m^{-3}, representing typical December wind-packed snow [*Sturm et al.,* 2002]. Densities greater than 300 kg m^{-3} were excluded since observations have shown that snow density remains relatively constant until the onset of spring melt. [W99; *Kwok and Cunningham,* 2008]. In the sensitivity analysis, the maximum difference in surface heat flux was ~1 W m^{-2} for all ice types when using a snow density of 200 kg m^{-3} instead of 300 kg m^{-3}. Otherwise, the changes in surface heat flux due to smaller differences in snow densities were negligible.

2.6. CONCLUSION

This study has shown that the airborne radar used on Operation IceBridge can accurately measure snow depth on level, first-year sea ice. This finding of "local" accuracy is enough to warrant the use of the extensive IceBridge snow depth data to assess snow cover trends across the Arctic Basin. On-going and future validation efforts on more complex sea ice topography will allow us to improve our accuracy when using the data, and for now, these data provide the highest spatial resolution of spring snow thickness. For the 2009–2013 period, the products show that snow has decreased by 37 ± 29% in the western Arctic and by 56 ± 33% in the Beaufort and Chukchi seas, compared to the 1954–1991 snow depth climatology produced by W99. These are large changes in snow depth distributions, and the implications are significant for future sea ice in the region. The changes could arise from changes in winter precipitation, changes in the date when sea ice is present to accumulate snow, or a combination of both.

Addressing the latter point, we provided evidence showing that monthly and annual snow accumulations have not changed in magnitude or timing using IMB buoy and W99 data. The results imply that either snowfall rates and snow redistribution have not changed, or the combined effect of their changes has cancelled any potential snow accumulation loss. We found a strong correlation between the timing of sea ice freeze-up and the reduction in spring snow thickness, which is consistent with the shift to first-year and young sea ice types in this region [*Nghiem et al.,* 2007; *Maslanik et al.,* 2011] and with snow depth measurements on younger ice types [*Radionov et al.,* 1997]. In future scenarios, delayed sea ice freeze-up and increasing winter precipitation are expected, which underscores the need for continual monitoring of the snow cover on Arctic sea ice.

The combined effect of reduced snow cover and young ice based on the 2009–2013 results yielded surface heat fluxes nearly double than that on young ice in the 1954–1991 period, and nearly quadruple than that on multiyear sea ice, regardless of differences in snow density. These results have several implications for the sea ice climate system. They indicate that: (1) the current and projected shift to younger ice types and a thinner snow cover in the Arctic will result in larger net outgoing longwave radiation during the autumn and winter seasons than in the 1954–1991 period, (2) the increase in heat input to the atmospheric boundary layer will likely increase the atmospheric moisture content, affecting precipitation rates, and (3) with a delayed, thinner sea ice cover, snowfall rates, regardless of change, will have an increasingly important role in the surface heat exchange during the autumn and winter seasons.

While the observed change in snow thickness distribution is consistent with the first-order effects of unchanged snow accumulation rates and delayed sea ice freeze-up, there are local processes that should be considered when interpreting our results. Sea ice motion and deformation, blowing snow, changes in snow redistribution and sea ice roughness, increased precipitation due to more open water areas, increased snow loss due to snow drifting into open leads, and altered atmospheric patterns, all likely contribute to changes in the snow depth distribution. Of particular interest is the shift to younger ice types, and the effects of their reduced surface roughness on drifting snow. The exact contributions of such processes are largely unknown due to the scarcity of collocated and contemporaneous datasets. These processes may be investigated in future validation efforts with better spatial resolution and more frequent coverage of airborne and satellite measurements, as well as with modeling studies that continue to develop and improve complex feedbacks. Impacts of these local processes may be better understood through the synthesis of

future observational, modeling, and remote sensing work, especially with the advent of ICESat2 in 2017.

Chapter 3. Seasonal Melt Pond Evolution

ABSTRACT

The seasonal evolution of melt ponds has been well-documented on multiyear and landfast first-year sea ice, but is critically lacking on drifting, first-year sea ice, an ice type that is becoming increasingly prevalent in the Arctic. Using one-meter resolution panchromatic satellite imagery paired with airborne and in situ data, we evaluated melt pond evolution for an entire melt season on drifting first-year and multiyear sea ice near the 2011 Applied Physics Laboratory Ice Station (APLIS) site in the Beaufort and Chukchi seas. A new algorithm was developed to classify the imagery into sea ice, thin ice, melt pond, and open water classes on two contrasting ice types: first-year and multiyear sea ice. Surprisingly, melt ponds formed three weeks earlier on multiyear ice. Both ice types had comparable mean snow depths, but multiyear ice had zero-to-five-centimeter deep snow covering ~37% of its surveyed area, which may have facilitated earlier melt due to its low surface albedo compared to thicker snow. Maximum pond fractions were 53 ± 3% and 38 ± 3% on first-year and multiyear ice, respectively. APLIS pond fractions were compared with those from the Surface Heat Budget of the Arctic Ocean (SHEBA) field campaign. APLIS exhibited earlier melt and double the maximum pond fraction, which was in part due to the greater presence of thin snow and first-year ice at APLIS. These results reveal considerable differences in pond formation between ice types, and underscore the importance of snow depth distributions in the timing and progression of melt pond formation.

3.1 INTRODUCTION

Global climate change is altering the Arctic system [*Overpeck et al.,* 2005; *National Academies,* 2012; *Kirtman et al.,* 2013]. According to the IPCC's 5th Assessment Report, the Arctic will be "nearly sea ice-free in September" by 2100 [*Stocker et al.,* 2013]. Model projections continue to overestimate the September minimum sea ice extent, indicating that certain physical processes and parameters are not fully understood for accurately predicting the state of the Arctic ice pack [*Stroeve et al.,* 2007; *Flato et al.,* 2013; *Kirtman et al.,* 2013]. One of the largest model uncertainties is the behavior of melt ponds [*Flocco et al.,* 2012; *Holland et al.,* 2012; *Hunke et al.,* 2013], whose presence has been shown to impact the timing and magnitude of the September minimum sea ice extent [*Schröder et al.,* 2014]. Melt ponds decrease surface albedo and increase solar absorption and transmission in sea ice during summer and thus, modify the surface heat budget of the sea ice cover [*Perovich et al.,* 2002a; *Light et al.,* 2008; *Nicolaus et al.,* 2012; *Light et al.,* 2015]. The presence of melt ponds also triples the amount of photosynthetically active radiation available to primary producers [*Nicolaus et al.,* 2012], and has an equally significant impact on the Arctic ecosystem [*Frey et al.,* 2011].

Our current understanding of seasonal melt pond evolution comes from studies of first-year landfast and drifting multiyear sea ice where long-term field measurements have been logistically feasible [*Nazintsev,* 1967*; Yackel et al.,* 2000; *Perovich et al.,* 2001; *Perovich et al.,* 2002b; *Eicken et al.,* 2004; *Polashenski et al.,* 2012]. Through these observations, four distinct stages of melt pond evolution have been described that capture the typical melt pond behavior during a summer melt season (see Figure 11 in *Eicken et al.,* [2002]). However, it is important to note that episodic events such as a mid-summer snowfall or an unusually-long period of sunny

skies can disrupt the sequence and timing of these stages. Nevertheless, in summation, melt pond evolution is best described by the following:

Stage 1: Snow melts, and a sub-surface freshwater ice layer is formed. The sub-surface ice layer helps maintain an impermeable medium, on which meltwater can remain and pool together to form melt ponds. These ponds typically have hydraulic heads well above sea level. Most meltwater contributes to pond formation, however some is lost through small cracks and flaws within the sea ice.

Stage 2: The snow cover is mostly melted, and melt ponds are well-developed. As in-ice temperatures increase, brine volumes subsequently enlarge, which increases the overall permeability of the sea ice. Once the sea ice becomes sufficiently permeable, meltwater flushing occurs and the hydraulic heads of melt ponds begin to decrease.

Stage 3: In-ice flaws and brine channels continue to grow with increasing temperatures, and the sea ice reaches its maximum permeability. During this stage, melt ponds can melt through the sea ice entirely and remain in direct contact with the surface ocean. For most sea ice in the seasonal ice zone, the sequence of melt pond evolution stops here as sea ice floes completely melt out.

Stage 4: For sea ice that withstands summer melt, its melt ponds begin to freeze over when air temperatures have sufficiently cooled. A freshwater ice layer forms on top of the melt ponds, creating a lid on which snow can accumulate and act as a reflective shield against solar radiation.

Melt pond evolution, whether it takes place on landfast, drifting, first-year, or multiyear sea ice, is well-represented by these four stages. However, the timing, duration, and magnitude of each stage differs considerably between landfast and drifting sea ice, and also between first-year and multiyear sea ice. Landfast sea ice has distinct dynamic and thermodynamic processes due to the effects of shallow bathymetry [*Reimnitz et al.,* 1978; *Mahoney et al.,* 2007], tides and near-shore currents [*George et al.,* 2004; *Petrich et al.,* 2012b], a fixed orientation to the sun, and perhaps most importantly, warm air and dust from nearby land [*Grenfell and Perovich,* 2004]. Even its snow differs compositionally from that on drifting sea ice because its snow cover affected by: (1) earlier freeze-up of landfast ice, which allows more time for snow accumulation and snow metamorphosis, (2) a fixed orientation to the dominant wind direction, affecting snow redistribution, and (3) the relatively larger amount of ice deformation on a per area basis due to concentrated compression of sea ice near shore, which also affects snow redistribution. The combination of these effects is unique to landfast ice melt processes, and thus, the timing and magnitude in melt pond evolution on landfast ice may not be not wholly representative of that on drifting sea ice.

Even if sea ice is drifting, the physical properties of multiyear ice facilitate a melt pond evolution uncharacteristic of first-year sea ice, [*WMO,* 1970; *Fetterer and Untersteiner,* 1998; *Johnston and Timco,* 2008]. Multiyear sea ice has pre-existing surface topography, which controls local snow depth distributions and melt pond fractions. Troughs in between ridges and hummocks trap drifting snow, often resulting in a thicker, more variable snow cover [*Radionov et al.,* 1997; *Untersteiner,* 1986; *Sturm et al.,* 2002]. In summer, the hummocky surface confines the lateral spread in melt pond area, and yield melt pond fractions on the order of ~30% [*Untersteiner,* 1986; *Fetterer and Untersteiner,* 1998; *Perovich et al.,* 2002b; *Eicken et al.,* 2004]. Comparatively, first-

year sea ice has low surface relief [*WMO,* 1970; *Untersteiner,* 1986; *Johnston and Timco,* 2008]. Its smooth surface topography allows snow to drift freely, resulting in a more uniform distribution primarily composed of well-developed drift bedforms, such as sastrugi, barchans, etc., which melt ponds form around in a similarly uniform fashion [*Filhol and Sturm,* 2015; *Radionov et al.,* 1997; *Sturm et al.,* 2002; *Petrich et al.,* 2012a; *Polashenski et al.,* 2012]. Its low surface relief allows pooled meltwater to spread laterally on the ice surface, resulting in larger areal melt pond fractions, which can be as large as 70% [*Yackel et al.,* 2000; *Eicken et al.,* 2004; *Scharien and Yackel,* 2005*; Polashenski et al.,* 2012].

There has been little previous work done on melt ponds on drifting first-year ice due to the logistical difficulties in collecting field observations on younger sea ice types. This study aims to provide a quantitative and qualitative understanding of the seasonal evolution of melt ponds on drifting first-year and multiyear sea ice, from pre-melt conditions in April to completely ice-free conditions in September. Using 1-meter resolution panchromatic imagery derived from higher-resolution National Technical Means (NTM) satellite imagery, we developed a new algorithm for classifying melt ponds, sea ice, thin ice, and open water. We analyzed imagery from the 2011 APLIS field site as it drifted from the Beaufort Sea into the Chukchi Sea (Fig. 3.1). The 2011 APLIS site was strategically placed on the boundary of multiyear and first-year sea ice, providing the opportunity to compare melt pond evolution on two contrasting ice types undergoing the same forcings. Airborne and in situ measurements during a joint NASA Operation IceBridge (OIB) and U.S. Naval Research Laboratory (NRL) "Determining the Impact of Sea Ice Thickness on the Arctic's Naturally Changing Environment" (DISTANCE) field campaign, located near the APLIS/Naval Ice Experiment (ICEX) ice camp [*Gardner et al.,* 2012] were used to evaluate pre-melt conditions on both ice types. These measurements allowed an exploration of the relationship

between snow cover, surface topography, and the timing of melt pond formation. Observations from buoys deployed by the International Arctic Buoy Programme (IABP) [http://iabp.apl.washington.edu/] and the Cold Regions Research and Engineering Laboratory Ice Mass Balance buoy project [http://imb/erdc/dren.mil] aided in the interpretation of the changing surface conditions at the field site. The melt pond fractions at APLIS were then compared with those from aerial images from the SHEBA field campaign [*Perovich et al.,* 2002b].

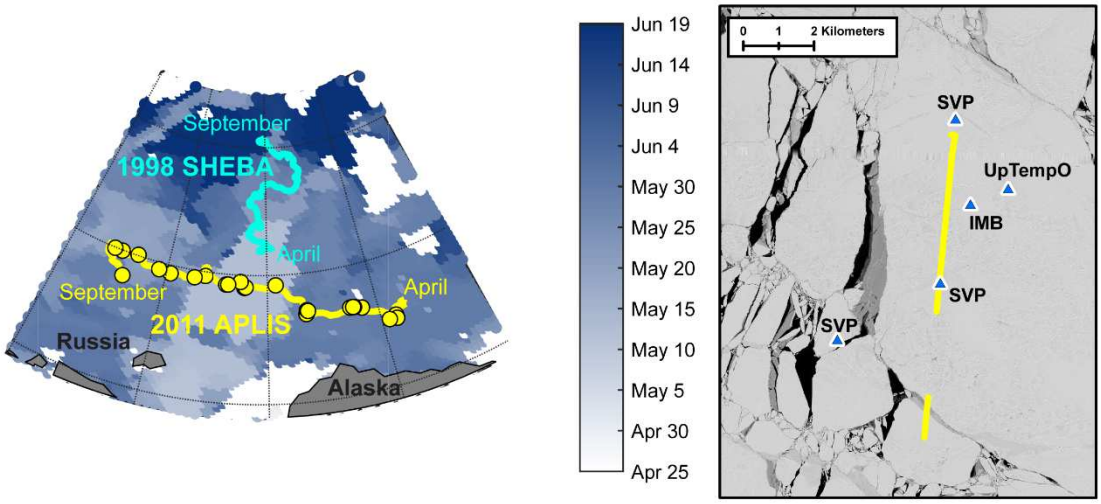

Figure 3.1 Left: Locations of the 1998 SHEBA (cyan) and 2011 APLIS (yellow) field campaigns. Both started in the Beaufort Sea, and eventually drifted into the Chukchi Sea. The yellow dots are locations of the NTM imagery for the APLIS field site. The background is the date of first melt in 2011 derived from passive microwave satellite data [*Markus et al.,* 2009]. **Right:** Locations of the SVP, UpTempO, and IMB buoys at the 2011 joint NASA OIB/NRL DISTANCE field campaign site, near the APLIS/ICEX ice camp. The ground survey line is in yellow, while the buoys are represented by blue triangles. The NTM image is from 28 April 2011.

3.2 DATA

3.2.1 *Satellite imagery*

Through the Measurements of Earth Data for Environmental Analysis (MEDEA) working group, images were derived from classified, higher-resolution satellite imagery from the U.S. NTM, or U.S. National Imagery Systems, and made publicly available at the Global Fiducials Library [http://gfl.usgs.gov/]. The images are 1-meter, panchromatic, greater than 15 km x 15 km in size with location and solar angle information at the time of acquisition. The images are dependent on cloud-free conditions and radiometrically inconsistent with spectral resolutions stretched to 256 levels [*Kwok,* 2013]. The NTM satellites target static sites, and in other cases, the area around the GPS locations of drifting buoys. The latter allows for a complete seasonal observation of melt pond evolution from a Lagrangian point-of-view. The 1-meter resolution enables identification of two surface features in melt pond evolution that can go unobserved in coarser resolution satellite imagery: (1) melt ponds that are smaller than the spatial resolution of the imagery and subsequently misidentified as sea ice, and (2) melt ponds on highly melted, level ice where melt pond fractions are large and the underlying ice thickness is thin, often resulting in the misclassification of dark-colored melt ponds as open water. Image acquisition is sporadic and dependent on clear weather, ranging from every day to roughly every three weeks. The 2011 APLIS site was chosen for this study due to the sequence of clear sky images through time (Table 3.1), its location on the multiyear ice pack boundary, and the abundance of available coincident airborne and in situ data. The passive microwave melt product was also used to help identify melt onset and freeze-up at the 2011 site [*Markus et al.,* 2009].

Table 3.1 NTM image and surface information[a]

Date (dd-mmm [scene])	Latitude (DD.DDDD)	Longitude (DD.DDDD)	Surface Temperature (°C)	Evaluated Area (km²)	First-Year Fraction (%)	Multiyear Fraction (%)
28-Apr [1]*	72.6541	-148.0323	-10.1	15	82	18
6-May [1]*	72.5219	-148.0280	-7.5	14	89	11
12-May [1]*	72.5624	-148.9739	-7.0	19	87	13
21-May [1]*	73.2769	-152.1350	-1.9	20	86	14
26-May [1]*	73.3753	-153.1670	-0.1	22	76	24
27-May [1]*	73.3823	-153.6753	0.9	17	79	21
27-May [2]*	73.3829	-153.2968	0.9	15	72	28
3-Jun [1]*	73.2396	-155.3930	-0.6	14	82	18
3-Jun [2]	73.1247	-155.4080	-0.6	14	95	5
17-Jun [2]*	73.5584	-159.5730	1.2	13	79	21
18-Jun [1]*	73.5238	-159.4423	1.4	5	91	9
28-Jun [1]*	74.6111	-163.7394	1.0	22	85	15
7-Jul [1]*	74.5132	-168.3492	1.0	12	89	11
9-Jul [1]*	74.7391	-168.9297	1.3	16	78	22
12-Jul [1]*	74.6002	-171.0215	1.5	7	80	20
23-Jul [1]*	74.8382	-174.2279	0.8	12	90	10
16-Aug [1]	74.7254	178.8184	-0.3	17	N/A	N/A
30-Aug [1]	74.9754	172.7827	-0.8	15	N/A	N/A

[a]Information pertaining to each analyzed NTM scene of the 2011 APLIS site. The asterisk indicates the scenes used in the ice type analysis in Section 3.4.2.

3.2.2 *Airborne data*

As part of the 2011 joint NASA OIB/NRL DISTANCE field campaign, an array of airborne and in situ observations were made in March in the vicinity of the 2011 APLIS/ICEX ice camp on the

boundary of multiyear and first-year sea ice in the Beaufort Sea [*Gardner et al.,* 2012]. The in situ observations were made along a nine-kilometer transect that was positioned to cross a range of sea ice types in the area, including undeformed and deformed first-year ice, thin newly-formed ice, and multiyear ice. OIB conducted a series of passes over the field site while collecting a suite of measurements, one from which surface elevation was derived. The OIB P-3 aircraft was equipped with a Digital Mapping System (DMS), capturing visible imagery of the surface along the flight path [*Dominguez,* 2010]. The DMS images were orthorectified and geolocated, and at the nominal flight altitude of ~460 meters, have a horizontal resolution of 10 cm [*Dominguez,* 2010]. Surface roughness in relation to ice type was determined using a combination of DMS images, in situ ice type identifications, and surface elevation data from the OIB Airborne Topographic Mapper (ATM), a spiral scanning laser altimeter which has a single-shot vertical accuracy of five-to-seven centimeters depending on the surface roughness within the laser footprint [*Krabill,* 2010; *Farrell et al.,* 2012; *Martin et al.,* 2012].

3.2.3 *In situ observations*

The strategic location of the 2011 APLIS site on the boundary of the multiyear ice zone provides an opportunity to compare the physical properties and features of drifting first-year and multiyear sea ice. Observations of snow and ice thickness were made roughly every five meters along the nine-kilometer NASA/NRL survey line on first-year and multiyear ice of varying deformation. Snow depth was measured using a Snow-Hydro© automated snow depth probe, or "MagnaProbe," with a ± 0.3 cm accuracy on level snow and sea ice. Coincident ice thickness measurements were collected using an EM-31 inductive measurement device, which has a ± 10 cm accuracy [*Eicken*

et al., 2001]. Three Surface Velocity Profiler (SVP) buoys recording air temperature and GPS locations were deployed at the southern, middle, and northern points of the survey line. The three drift tracks aided in the geolocation of the OIB airborne and NASA/NRL in situ measurements in the NTM imagery. Melt onset and freeze events were identified using a combination of SVP, Ice Mass Balance (IMB) [*Perovich et al.,* 2013], and UpTempO temperature data [http://psc.apl.washington.edu/UpTempO/].

3.3 METHODS

3.3.1 *Algorithm overview*

An algorithm was created with the overarching goal of correctly identifying melt ponds, sea ice, thin ice, and open water in the NTM imagery. The sea ice class consists of thin, medium, and thick first-year ice, and multiyear ice [*World Meteorological Organization (WMO),* 1970]. The thin ice class was defined in this study and includes nilas, grey, and white ice [*WMO*, 1970], all of which have darker intensities than first-year and multiyear ice in the NTM imagery. Nilas, grey ice, white ice, submerged ice around floe edges, water-saturated ice on heavily-ponded undeformed ice, and cloud and ridge shadows can readily be misclassified as melt ponds due to their similar dark intensity to melt ponds. The algorithm goes through a multistep process identifying and separating these hard-to-distinguish features, along with open water and sea ice, so that residual dark pixels are correctly classified as melt ponds (Fig. 3.2). The algorithm relies on: (1) physically-based thresholds accounting for the radiometric inconsistencies in the NTM imagery, and (2) consideration of neighboring pixels' intensities due to classes with overlapping grayscales. Melt

pond fractions are presented as the pond area divided by the total ice area. The total ice area is ponded ice and unponded ice combined. Sea ice, thin ice, and open water fractions are reported as the percentage of the analyzed scene; their sum is 100%.

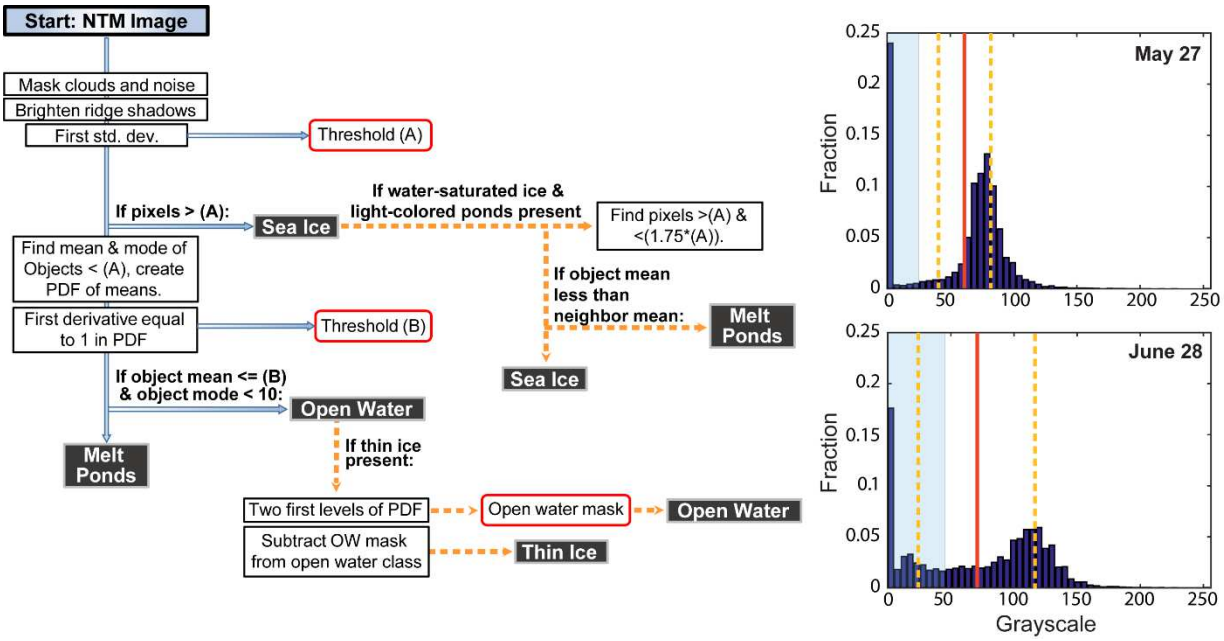

Figure 3.2 Left: A schematic for the classification algorithm outlining the steps for identifying sea ice, thin ice, melt pond and open water classes from the NTM imagery. The blue arrows indicate standard procedure, while dashed orange lines represent specific conditions in which additional steps must be used to prevent misclassifications. The end-product is represented by solid-grey boxes. **Right:** Histograms of the NTM images for 27 May (top) and 28 June (bottom), with the mean brightness indicated by the red line, and standard deviation by the dashed yellow line. The blue shading represents pixels less than Threshold (A), the value of the standard deviation that undergo processing by the classification algorithm.

3.3.2 *Masking*

Prior to automated classification, clouds, cloud shadows, and instrument noise were manually masked to prevent misclassifications. After masking, ridge shadows were replaced with an equivalent brightness of ridges in the scene (Fig. 3.3, A1-A2). Because ridges produce the highest intensity in each scene, dark pixels connected to ridge pixels were identified as shadows. Shadow length was determined using an estimated ridge height of three meters [*Lowry and Wadhams,* 1979], and available solar elevation angle information (Equation 3.1). The three-meter estimated ridge height was verified by solving for the "ridge height" term in Equation 3.1 using manual measurements of ridge shadow lengths in scenes with low solar elevation angles. The three-meter estimated height and solutions to Equation 3.1 were largely consistent, warranting the use of a three-meter estimate. The shadow direction was estimated as 180° from the solar azimuth angle. The intensity histogram of the "shadow" pixels was evaluated for a bi-modal distribution, which indicates the presence of melt ponds in the ridge shadows. In the event of shaded melt ponds, a threshold was identified as the trough in the bimodal distribution. The intensity value of any shaded pixels greater than this threshold were increased to the brightness of ridges. Ridge shadow corrections were performed primarily on spring images when sun angles were low enough to cast large shadows, and made up less than ~0.5% of each spring scene. Any errors associated with this step made up less than the total shadow coverage, and were deemed negligible.

$$shadow\ length = \frac{ridge\ height}{\tan\left(\theta_{elevation}\right)} \tag{3.1}$$

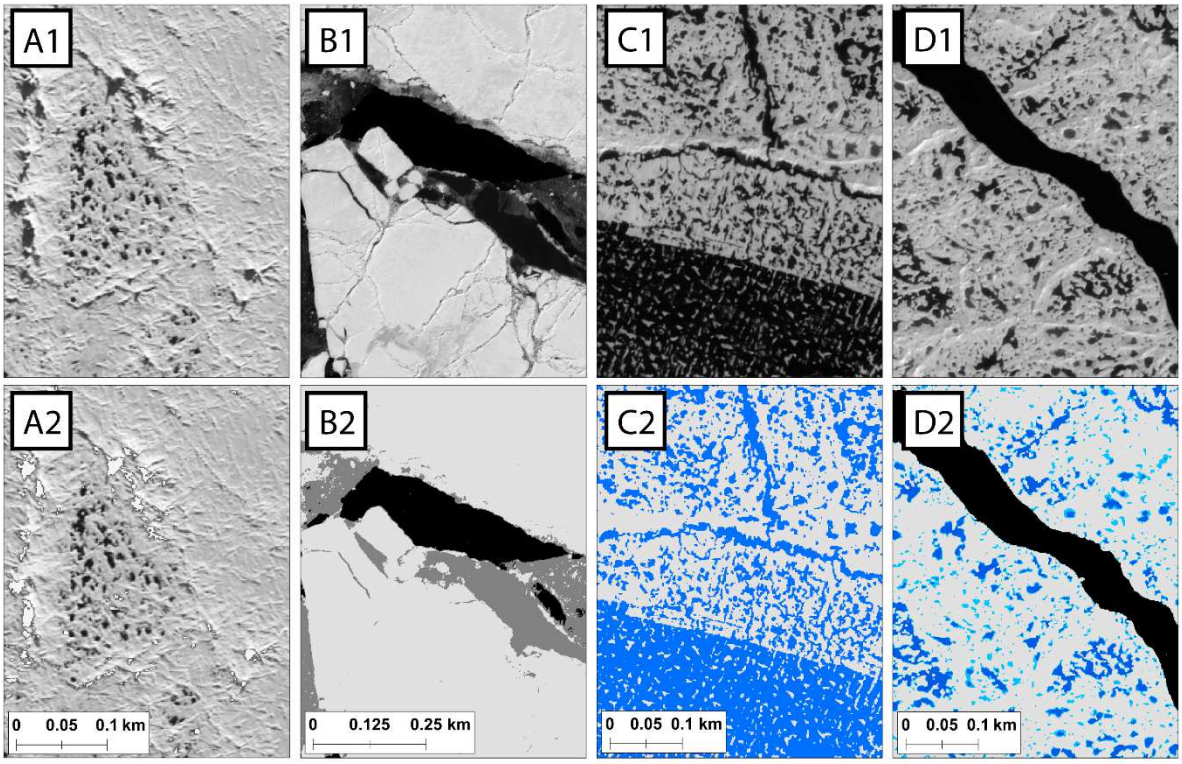

Figure 3.3 The upper plots are the raw NTM imagery while the bottom plots are the results of key steps in the classification process. **A2**: an example of treating ridge shadows, which brightens shadows to ridge intensity. **B2:** an example of the open water mask application (black) with light and dark grey representing thick and thin ice, respectively. Note the change in scale. **C2:** the classification results for melt ponds (blue) over thin first-year, thick first-year, and multiyear sea ice (light grey). Multiyear ice is in the upper third of the image, thick first-year ice in the middle, and heavily-ponded thin first-year ice on the bottom. **D2:** the effect of adding in Steps 7 and 8 in the classification process. The additional light-colored ponds are light blue, while ponds identified without Steps 7 and 8 are blue. Open water is black and sea ice light grey.

3.3.3 *Algorithm description*

After cloud and shadow masking, the NTM images were separated into classes using the brightness, mean, and mode of interconnected pixels (Fig. 3.2, left). The interconnected pixels were grouped together based on their grayscale intensity, and are hereby referred to as "objects." The open water, thin ice, sea ice, and melt ponds were classified using the following steps:

1. *Thresholding for sea ice and dark objects*: Threshold (A) was defined as the value of the first standard deviation of the entire cloud-free area in the NTM scene (Table 3.1). Using the value of a standard deviation accounts for radiometric variability between scenes, as well as variability in surface brightness due to the changing melt conditions (Fig. 3.2, right). For example, if numerous melt ponds are present, their intensities cover a larger grayscale range, which increases the standard deviation of the scene and consequently increases Threshold (A). Any pixels with values between one and Threshold (A) were identified, and based on their interconnectedness using four neighbors, were grouped together into objects to be analyzed in subsequent steps. Pixels with intensities greater than Threshold (A) were classified as sea ice, except in scenes of the late melt season that had both dark water-saturated sea ice and light-colored melt ponds. These two surfaces are indistinguishable from each other without additional steps due to their overlapping intensities. Steps 7 and 8 provide greater detail on the approach for distinguishing them from one another.

2. *Object statistics*: The mean and mode of each object found in Step 1 was calculated. Objects containing fewer than five pixels were set aside in Step 3 for improved performance, but incorporated into all subsequent steps.

3. *Thresholding for open water and thin ice*: The darkest, most homogenous shade in an NTM scene is open water; the consistent, low reflectance of open water dominates, resulting in a low mean and variance of any object composed of open water. A probability density function (PDF) was created of the object means, and the derivative calculated. Threshold (B) was identified as the first sequential derivative equal to or greater than one. If no threshold was found, as in the case of images with high noise levels, the derivatives were multiplied by ten and Step 3 was repeated until Threshold (B) was found.

4. *Separating open water and thin ice*: Objects with means less than or equal to Threshold (B) and a mode intensity of less than ten were identified as open water, helping prevent the misclassification of open water in between broken up floes as melt ponds. In early spring scenes, nilas and young ice [*WMO*, 1970] were included in the open water class due their dark gray shades and neighboring relationships with open water. These ice types were separated from the open water class using an open water mask outlined in Step 5, and classified as the thin ice class.

5. *Open water mask*: An open water mask was created to encompass objects occupying the lowest two levels of the object intensity PDF. The open water mask was subtracted from the open water areas identified in Step 4, with the residual pixels being separated into a thin ice class (Fig. 3.3, B1-B2). In scenes with rotten sea ice at the end of the melt season, an open water mask derived in the same manner was applied, leaving behind melt pond pixels which have an ice bottom intact, but classifying ponds that have melted through entirely as open water. Ponds that melted through entirely made up less than 5% of the total pond fraction in all cases.

6. *Melt pond class:* Residual objects with means greater than (B) were classified as melt ponds (Fig. 3.3, C1-C2). The image classification is complete at Step 6 for scenes exhibiting melt Stage 1 (pond formation) and melt Stage 2 (pond drainage) [*Eicken et al.,* 2002; *Polashenski et al.,* 2012]. Total computation time, including cloud and open water masking, is ~15 minutes on an Intel i7 8-core processor machine.

7. *Light pixel objects*: For scenes exhibiting melt Stage 3 [*Eicken et al.,* 2002; *Polashenski et al.,* 2012], Steps 7 and 8 were followed for correctly identifying and separating dark, water-saturated sea ice and light-color melt ponds from each other. Melt Stage 3 describes a highly permeable, melted ice cover where the majority of ponds have formed thaw holes, and are in direct contact with the surface ocean [*WMO,* 1970; *Eicken et al.,* 2002; *Polashenski et al.,* 2012]. During this advanced stage of melt, heavily-melted, water-saturated sea ice is often present on undeformed first-year floes. This melting ice can be misclassified as melt ponds due to its similar intensity to light-colored melt ponds. Likewise, light-colored melt ponds on thick ice can be misclassified as sea ice due to their high intensity reflectance. To counter these misclassifications, a new set of "light" objects was identified using pixels brighter than Threshold (A) but darker than 1.75 times Threshold (A), encompassing pixels of light-color ponds and water-saturated sea ice.

8. *Light-colored melt ponds*: The means of both the light objects and the surrounding pixel neighbors were calculated. Neighboring pixels were identified as any pixels surrounding an object with a distance of one pixel. If the mean of an object was larger (brighter) than its neighbors', the object was classified as sea ice. If the object mean was less than its neighbors', it was classified as a melt pond. In the 28 June scene comprised of heavily-melted, thin undeformed first-year and

deformed multiyear ice, Steps 7 and 8 contributed to a ~10% increase in areal pond fraction (Fig. 3.3, D1-D2). Note that Steps 7 and 8 are only required for scenes of highly advanced melt when light-colored ponds on thick ice and dark, water-saturated thin ice are both present. In future work, scenes comprised of only one ice type may not require these additional steps due to the less complex nature of the sea ice surface.

3.3.4 *Ice type identification*

First-year and multiyear ice types were manually identified in the NTM and DMS images using floe shape, deformation, and surface roughness, as well as melt pond shape and homogeneity following the descriptions in Johnston and Timco [2008] and the WMO Sea-Ice Nomenclature [1970]. The 2011 ice type identifications were verified with those made in March along the NASA/NRL ice survey line near the 2011 APLIS/ICEX field camp, and were consistent. Deformed and undeformed first-year sea ice types were combined into a single first-year sea ice class for the scope of this study, but separating the study by level of ice deformation would be an insightful topic to expand on in future work.

A challenge in using NTM imagery for an ice type analysis is that there is variability in scene acquisition and ice drift, which means that not all of the same ice floes will be included in all scenes. Changes in melt pond fractions may be affected by a sudden increase or decrease in the percentage of multiyear and first-year ice from scene to scene. Considering this, the percentages of multiyear and first-year ice from each scene are provided in Table 3.1. On average, multiyear and first-year ice made up 16% and 84% of the analyzed scene areas, respectively, and both standard deviations were 6%. The main seven-kilometer-by-seven-kilometer ice floe where

OIB/NRL airborne and in situ measurements were collected was present in 13 out of the 16 scenes from April to July. In August, the sea ice was too deteriorated to track surface features or distinguish ice types.

3.4 RESULTS

3.4.1 *Algorithm accuracy*

A contingency table was produced for each scene using 300-random points "ground-truthed" by the visual examination of original NTM images. Figure 3.4, left, represents the fraction of correctly identified points (red) compared to the fraction of points visually identified as ponds (black) within each scene. An overlap of symbols represents high accuracy, with the distance between similar-shaped symbols being a function of the error rate. On average, the overall classifier accuracy was highest in May, June, and August at 99%, with the lowest in July at 96%. The largest absolute error was seven percent for melt ponds in the 23 July scene where numerous floes were rubbled, heavily-ponded, and water-saturated, leading to an increase in mixed pixels and subsequent misclassifications of open water and melt ponds (Table 3.2). Upon closer inspection of the scene, there was an abundance of misclassified rubble and brash ice sandwiched in between fragmented floes; false positive misclassifications occurred due to their similar intensity to melt ponds and their neighboring relationship with sea ice pixels (Fig. 3.4, right). In future work, these misclassifications may be avoided by using geometric thresholds for separating angular-like rubble ice areas from more circular-patterned melt ponds, and/or evaluating object variance and applying pond and rubble ice variance thresholds.

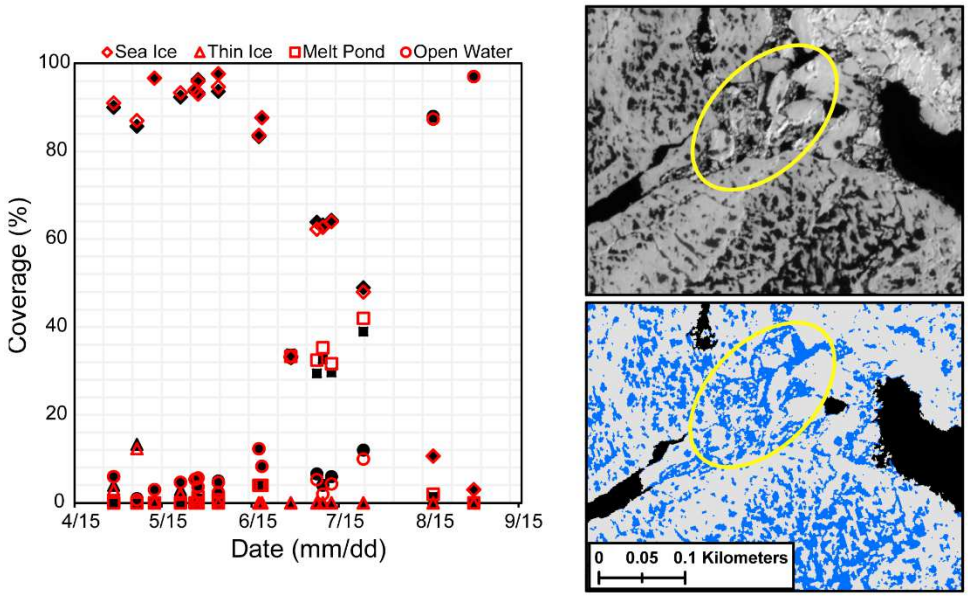

Figure 3.4. Left: A comparison of algorithm classifications (red) and true user inspection-determined class identifications (black) from each NTM image using a 300-random point sample distribution. Each symbol shape depicts a specific surface class: sea ice, thin ice, melt pond, or open water. The distance between similar-shaped symbols is a direct function of accuracy: the closer the overlap, the more accurate the algorithm classification. **Right:** False positive melt pond classifications due to the presence of rubble ice (within yellow circle). In the melt pond product, sea ice is light grey, melt ponds are blue, and open water is black.

Table 3.2 The 23 July contingency table[a]

23-Jul	True SI	True MP	True OW
SI Class	144	0	0
MP Class	3	117	6
OW Class	0	0	30

[a]The contingency table for 23 July showing sea ice, melt pond, and open water classification accuracies using 300-random point sample distribution. The false positive misclassifications of melt ponds were due to mixed pixels, and brash and rubble ice.

3.4.2 *First-year and multiyear melt pond evolution*

At the 2011 APLIS site, sub-zero temperatures persisted throughout April and no melt ponds were observed (Fig. 3.5). Areas of wind-scoured blue ice were present, and many were identified in the field as the tops of hummocks and refrozen melt ponds from the previous year. The first melt ponds were observed on multiyear sea ice on 26 May (Fig. 3.6, left). By 27 May, ponds encompassed ~1% of the multiyear ice area while those on first-year ice covered a negligible area. Multiyear pond fractions increased substantially from 3% to 24% between 3 June and 18 June. No melt ponds were observed on first-year ice (Fig. 3.6, top right) until June 17 when pond fractions increased to 3%. On June 28, first-year pond fractions jumped to 31%, exceeding the 26% multiyear pond fractions.

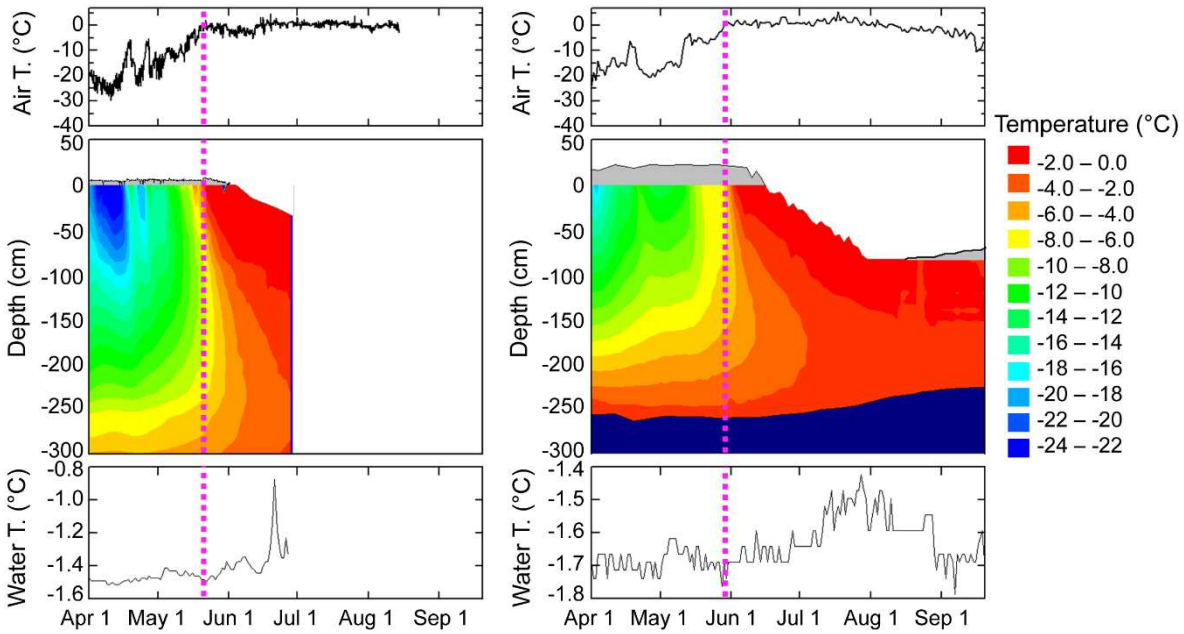

Figure 3.5. Left: From top down, 2011 APLIS air temperature, snow depth, ice and ocean temperatures, and surface ocean temperature from IMB buoy 2011A. The warming in the surface ocean coincides with melt pond formation. The IMB was deployed on a multiyear ice floe of 350 cm thickness with no snow cover. **Right:** From top down, 1998 SHEBA air temperature, snow depth, and ice and ocean temperatures, and surface ocean temperature from IMB buoy 1997E, which was deployed on a multiyear ice floe in October 1997. Before melt onset in 1998, the multiyear floe had an ice thickness of 260 cm and a 22 cm deep snow cover. The pink dashed lines indicate melt onset determined by buoy data, NTM imagery, and SHEBA field observations.

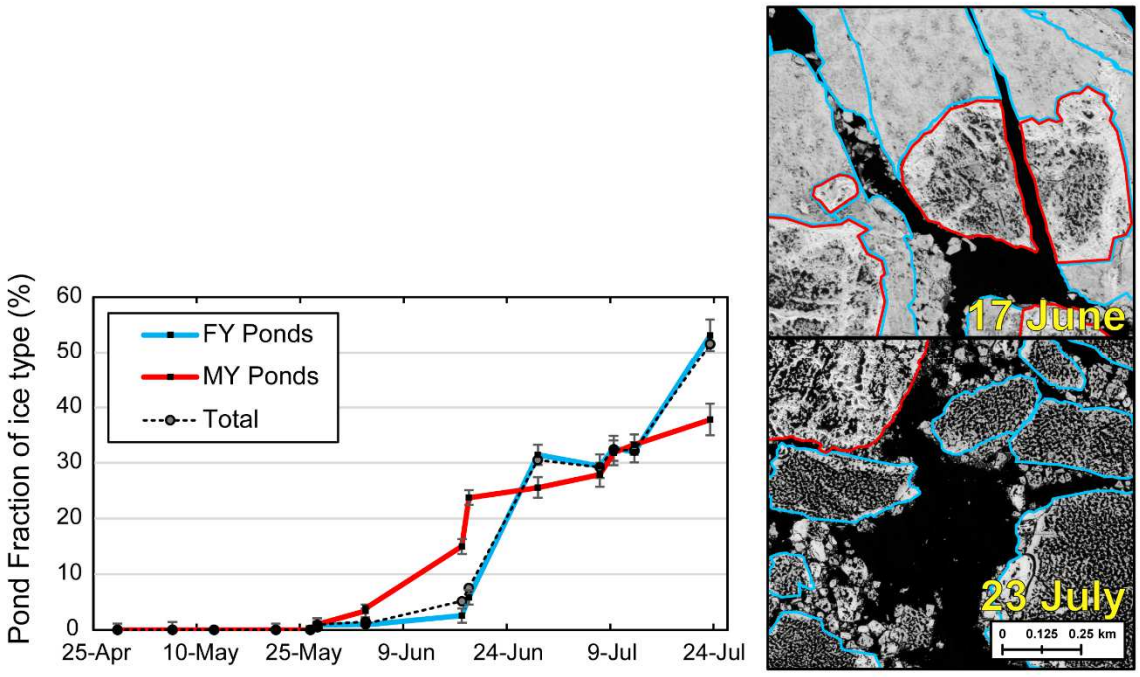

Figure 3.6. Left: Pond fractions given as the fraction of the corresponding ice type area. The error bars denote confidence intervals to the 95th percentile. The sea ice in the scenes disintegrated after late July, making differentiation between ice types unreliable. **Top right:** A zoom-in of the 17 June scene showing substantial ponding on multiyear floes surrounded by unponded first-year floes. **Bottom Right:** A zoom-in of the 23 July scene showing maximum pond fractions on both ice types. Note first-year ice floes have become progressively fragmented at this time in the melt season. Ice type masks outline multiyear ice in red and first-year ice in cyan in both scenes.

Pond drainage was visibly evident on multiyear ice in scenes between 18 June and 28 June and on first-year ice between 28 June and 7 July (Fig. 3.7). During melt Stage 2, drainage typically decreases melt pond fractions due to the loss of surface meltwater via vertical percolation and horizontal transport into flaws [*Eicken et al.,* 2002; *Polashenski et al.,* 2012]. Interestingly,

multiyear pond fractions did not decrease during the drainage event. Instead, the growth rate in melt pond fractions temporarily slowed between 18 June and 28 June. During this ten-day period, air temperatures ranged from 0°C to 2°C and no snow accumulation was recorded by the IMB buoy, indicating that the reduced growth rate was not influenced by a freeze or snowfall event.

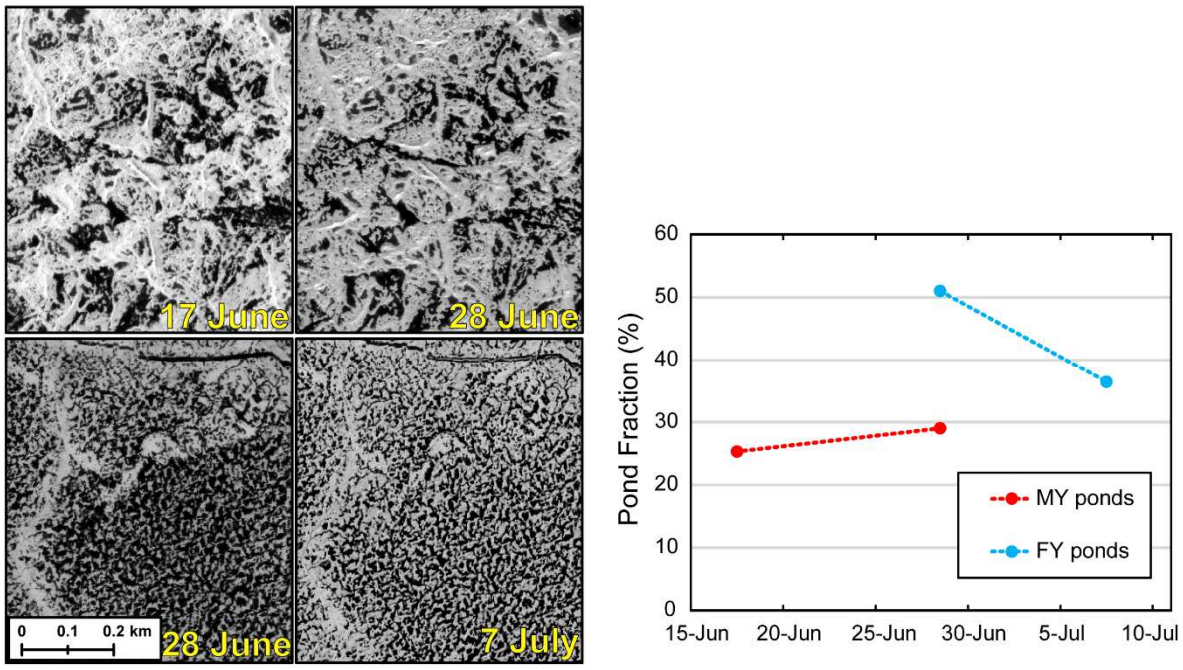

Figure 3.7. Left: At the 2011 APLIS site, pond drainage on multiyear ice (top) occurred between 17 June and 28 June, while drainage on first-year ice (bottom) occurred between 28 June and 7 July. **Right:** Melt pond fractions for the corresponding multiyear and first-year ice floes samples during melt pond drainage. Note that these sample areas were within three kilometers of each other.

To explore why multiyear pond fractions increased during drainage, we tracked two 650-m-by-650-m areas, one sampling a multiyear ice floe and the other a first-year ice floe, during their drainage events (Fig. 3.7). Drainage on the multiyear floe decreased some pond areas, but this decrease was compensated by the formation of new, smaller ponds and growth of other ponds on other parts of the ice floe, and increased pond fractions by four percent (Fig. 3.7). First-year pond drainage was not observed until after June 28, and caused only a slight decrease in the total first-year pond fractions (Fig. 3.6). On the first-year floe sample, drainage was uniform and wide-spread, decreasing pond fractions by 15% (Fig. 3.7). These findings reveal that multiyear pond drainage is spatially and temporally variable, unlike the uniform nature of pond drainage on first-year sea ice. Despite both ice types undergoing the same air temperature forcings, the different behaviors of their melt ponds come back to the effects of their contrasting ice topographies. After 12 July, first-year pond fractions steadily increased to a maximum of ~53% (Fig. 3.6). Multiyear pond fractions rebounded to ~30% in early July, increasing slowly for the remainder of the month to reach a maximum of ~38% on 23 July. The sea ice began breaking up in late July, and by early August, the vast majority of sea ice in the scenes had completely melted.

3.4.3 *Melt pond evolution at APLIS and SHEBA*

The melt seasons at SHEBA and APLIS began similarly, but diverged in their progressions, concluding with remaining sea ice at SHEBA and complete open water at APLIS when autumn freeze-up began (Fig. 3.8). Melt onset at the field sites started about one week apart in late May (Fig. 3.5). Air and surface temperatures rose to 0°C on 20 May at APLIS and remained near the freezing point until 1 June, with the first melt ponds appearing in the imagery on 26 May. The date

of pond onset is somewhat consistent with the passive microwave melt product, which showed the date of the first melt of the season, occurring on 29 May (Fig. 3.1) [*Markus et al.,* 2009]. At SHEBA, melt onset was observed after a rain event on May 29. Air temperatures remained above freezing after 29 May, the snow cover completely melted by 5 June, and the first ponds appeared on 20 June [*Perovich et al.,* 2002b; *Perovich et al.,* 2003]. APLIS air temperatures cooled below 0°C from 1 June to 12 June (Fig. 3.5), and melt pond fractions initially grew more slowly than those at SHEBA, taking eight additional days to reach 5% on 17 June (Fig. 3.8). By 28 June, APLIS air temperatures were well above freezing, and melt pond fractions at APLIS reached 30%, exceeding the 20% pond fractions at SHEBA.

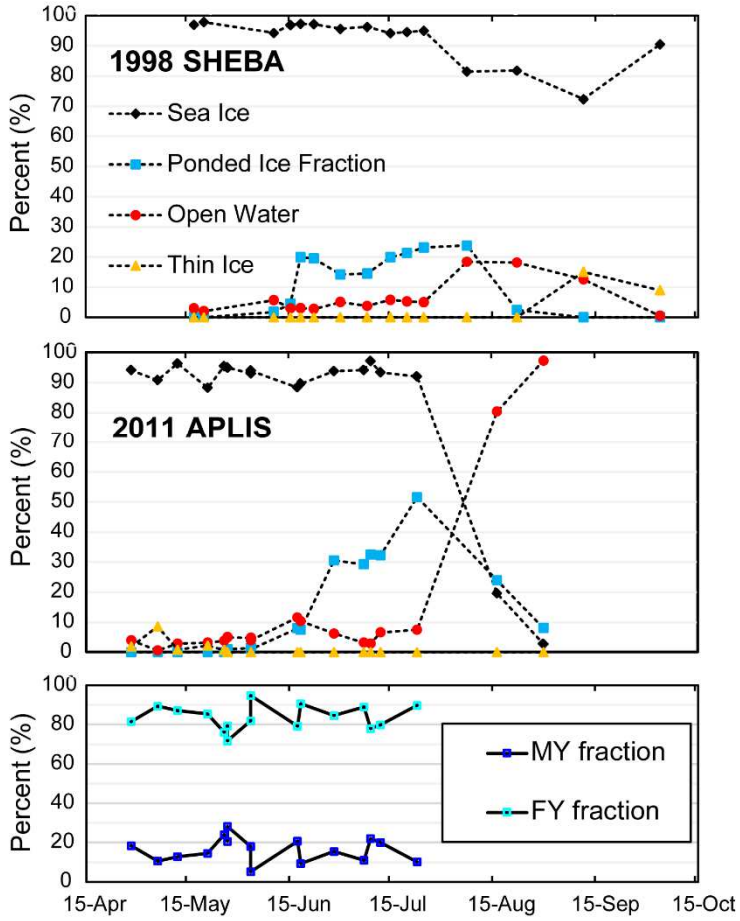

Figure 3.8. Top: Sea ice, thin ice, and open water fractions of the 1998 aerial SHEBA imagery, adapted from *Perovich et al.,* [2002b]. Their sum equals 100%. Melt ponds are represented as the fraction of ponded ice to the total sea ice area. **Middle:** Sea ice, thin ice, and open water fractions of each NTM scene for the 2011 APLIS site. Again, melt ponds are represented as the fraction of ponded ice to the total sea ice area. Sea ice fractions are subject to scene variability and ice drift. **Bottom:** The fraction of multiyear and first-year ice within each scene for the 2011 APLIS site due to variability in scene acquisition and ice floe convergence and divergence along the multiyear ice pack boundary. Extensive melt and breakup of the sea ice pack made ice type identifications unreliable after July.

Pond drainage was observed at SHEBA between 22 June and 30 June, and likely contributed to the six percent drop in pond fractions during that time [*Perovich et al.,* 2002a; *Perovich et al.,* 2002b]. APLIS melt pond drainage occurred from mid-June to mid-July with minimal effect on melt pond fractions due to the timing offset in drainage between ice types (Fig. 3.6), and the varying percentages of ice types in each scene (Fig. 3.8, bottom). Melt pond fractions decreased by two percent between 28 June and 7 July, and was likely due to the uniform, wide-spread drainage observed on first-year sea ice (Fig. 3.7), which made up 85%–89% of the sea ice in the scenes (Figs. 3.8, bottom, and Table 3.1). By 23 July, APLIS pond fractions reached their maximum of 48%, which was twice as much as the 24% maximum at SHEBA. Following the maximum, pond fractions decreased at both sites as a result of two contrasting processes. SHEBA ponds began freezing over on 17 August, while melt continued at rapid pace at APLIS, eventually leading to the total melt of sea ice in the NTM scenes. By September, the APLIS site had become ~100% open water, while SHEBA had a ~15% increase in newly-formed thin, or young, ice. According to the passive microwave melt product, early autumn freeze-up began at APLIS on September 25, approximately one month later than the observed freeze-up at SHEBA [*Markus et al.,* 2009]. Interestingly, in 1998, sea ice at the location of the 2011 APLIS site also completely melted.

3.5 DISCUSSION

3.5.1 *APLIS versus SHEBA*

At the end of the melt season, freeze-up began from 100% open water at APLIS and only 20% open water at SHEBA. Several environmental conditions differed between the field sites, and their differences likely contributed to the disproportionate amount of open water at the end of the melt season. For one, the APLIS snow cover was nearly 50% thinner than SHEBA's; APLIS had a 17.7 cm average and 17.3 cm standard deviation compared to SHEBA's 33.7 cm average and 19.3 cm standard deviation [*Sturm et al.,* 2002]. Using an average snow density of 340 kg m^{-3} and latent heat of fusion of 0.335 MJ m^{-2}, 20 W m^{-2} of energy was needed to melt the snow at APLIS, or nearly half of the required 38 W m^{-2} for melting SHEBA's snow cover. Considering the 17.3 cm standard deviation in snow depth at APLIS, many areas had very little or no snow, and as such, would have had an albedo approaching or equivalent to bare sea ice, which is 0.7, rather than the 0.85 of an optically-thick snow cover of ten centimeters or more [*Perovich,* 2007]. Under these conditions, the amount of combined solar absorption and transmittance would have doubled. While surface albedo plays a large role in the timing of melt onset, additional factors can also affect when melt onset occurs. For example, the rainfall event on 29 May at SHEBA may have increased sensible and downward longwave fluxes.

Another important discrepancy between APLIS and SHEBA is the composition of ice types. Both sites were composed of a mixture of ice types: undeformed, deformed, first-year and multiyear sea ice. However, APLIS had a substantially larger percentage of first-year ice, making up ~86% of the NTM scenes, while SHEBA was predominately multiyear ice. Additionally, the majority of first-year ice at APLIS was undeformed. As such, the APLIS site had a thinner ice

cover with larger melt pond fractions, which allowed greater solar absorption within and through the ice cover, facilitating melt. The difference in ice type composition, together with dissimilar snow covers, undoubtedly contributed to the diverging melt progressions at APLIS and SHEBA due to the effect of their albedo and subsequent solar absorption. Being a comparison of two case studies, there are differing factors that may have also influenced melt processes, such the relative latitude with respect to solar radiation and atmospheric conditions.

3.5.2 *Effects of snow distribution*

Melt onset occurred in mid-May at APLIS, yet ponds were not observed on first-year ice until three weeks after multiyear ponds became present. A possible source of this timing offset may be the local snow depth distributions on first-year and multiyear ice. For example, a thin snow cover on one ice type may expose its ice surface to solar radiation earlier in the season, increasing solar absorption, warming, and subsequent melt [*Perovich et al.,* 2002a; *Light et al.,* 2008; *Perovich and Polashenski,* 2012]. March in situ snow depth data from the NASA/NRL survey line were evaluated to assess snow depth distributions on each ice type. Snow data from the IMB buoy at the 2011 site indicates that snow depths did not increase significantly after the March measurements were taken, showing less than five-centimeter accumulation for April and May combined (Fig. 3.5). The lack of snow accumulation is consistent with the results of Webster et al. [2014], which show low April and May snow accumulation rates in this region from more recent years.

According to the March in situ measurements, snow on first-year ice had an 18 cm average, 17 cm standard deviation, and one centimeter standard error, while multiyear ice snow had a 17

cm average, 20 cm standard deviation, and two centimeter standard error. The differences in the snow depth averages and standard deviations were within their standard errors, suggesting that, on average, the snow cover was similar on both ice types. However, snow depth distributions on multiyear and first-year ice are often dissimilar due to the effects of ice topography on wind-driven redistribution. On multiyear ice, snow is blown off of the tops of hummocks and ridges and collected in surface depressions, resulting in a non-uniform snow depth distribution. The non-uniform location of multiyear melt ponds also reflects the influence of rough ice topography. On deformed first-year ice, the surface topography is even rougher since it has not yet undergone significant melt and weathering, and as a consequence, its snow cover is typically thicker, more variable. On undeformed first-year ice, snow depth distributions vary, but in a more uniform way via the formation of drift bedforms, such as sastrugi and barchans, which later act to guide the uniform distribution of melt ponds.

Considering the effects of ice topography on snow depth distributions, in situ snow depths were examined as a function of ice age and level of deformation to see if a relationship between snow depth and pond onset existed. At first glance, no relationship was found between the timing of melt pond formation and the mean snow depths; pond formation occurred first on multiyear, and roughly at the same time on deformed and undeformed first-year ice, but mean snow depths were thickest on deformed first-year ice, and comparable between multiyear and undeformed first-year ice. Upon closer inspection, thin snow covered a significantly larger area on multiyear ice than first-year ice (Fig. 3.9), with zero-to-five-centimeter deep snow making up ~37% of the surveyed multiyear ice area. In comparison, zero-to-five-centimeter deep snow covered only 11% and 15% of the surveyed deformed and undeformed first-year ice, respectively. A snow depth of less than ten centimeters is no longer optically thick [*Perovich,* 2007], and thus, the surface albedo

of the multiyear ice areas would have been relatively lower, enabling more solar absorption and warming of the ice surface.

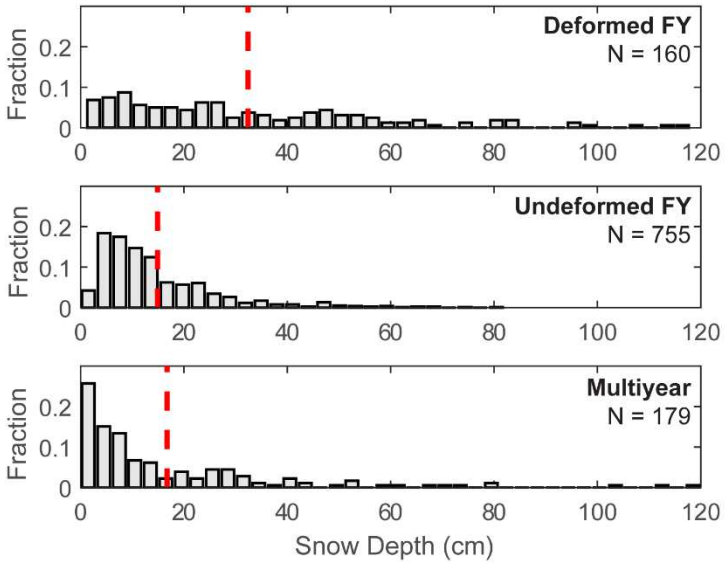

Figure 3.9. Snow depth distributions for deformed and undeformed first-year sea ice, and multiyear sea ice. The red dashed line is the mean snow depth for the corresponding ice type. A bin size of approximately three centimeters was used for all sea ice types.

3.5.3 *Influence of meltwater transport and surface topography*

Lateral meltwater transport and surface topography play large roles in the extent of ponding on different ice types [*Fetterer and Untersteiner,* 1998; *Eicken et al.,* 2002; *Eicken et al.,* 2004; *Polashenski et al.,* 2012], but little is known about their roles in the timing of melt pond evolution. Lateral meltwater transport is topography-driven, with meltwater draining to lower elevations, from ridges onto depressions and in flaws and cracks within the sea ice [*Eicken et al.,* 2002;

Polashenski et al., 2012]. We evaluated OIB altimetry-derived surface elevations of first-year and multiyear ice from the NASA/NRL in situ survey line to determine the relative surface elevation and surface roughness of each ice type in conjunction with early melt pond location on undeformed and deformed first-year sea ice. The ATM elevation measurements were gridded with an average of three points per cell. The elevation grid was aligned with multiyear and deformed and undeformed first-year ice type masks. Following *Eicken et al.* [2004], surface roughness was determined using the standard deviation of surface elevation in each ice type's area.

Multiyear ice had the highest surface elevations and more than double the surface roughness of undeformed first-year ice, followed by deformed first-year sea ice which was 1.5 times rougher than undeformed first-year ice. Hummocks and ridges funnel meltwater into smaller, low-lying areas, which accumulate meltwater within a fixed area at a faster rate than level sea ice due to drainage from surrounding sloped surfaces. On multiyear sea ice, these areas were likely the first to accumulate sufficient meltwater to penetrate through its relatively thin snow cover, become exposed to the air, and thus, would have been the first melt ponds to be detected by satellite sensors at the APLIS site. On undeformed first-year ice, meltwater can spread more thinly and extensively, and remain shielded by its relatively thicker, more reflective snow cover for a longer period of time, and may explain the delayed visibility of first-year melt ponds at the APLIS site. It may also explain the sudden presence of numerous first-year melt ponds on June 28; both the snow cover had become sufficiently thinned by melt, and enough meltwater had accumulated for many melt ponds to penetrate through the uniformly-distributed snow cover at the same time.

Interestingly, the first melt ponds to form on deformed and undeformed first-year ice were located on the boundary with multiyear ice floes. These melt ponds likely formed from the accumulation of meltwater from higher freeboard areas of neighboring multiyear floes. It is not

clear whether meltwater follows surface gradients to these boundaries, accumulates in depressions on first-year ice, and seeps upward through the snow cover, or simply melts through the snow cover. Additionally, seawater may have percolated onto lower-lying first-year ice at these boundaries, especially if the first-year ice is depressed down by thicker, neighboring ice floes. Regardless of the cause, these boundaries are the locations of the first ponds on drifting first-year ice, and can be thought of as "hot spots" for solar absorption early in the melt season. These areas became the location of "break points" later in the melt season, where the sea ice broke apart into smaller ice floes. Having had more time to melt and thermodynamically weaken, these spots are more susceptible to breakup during dynamic events, and have been shown to be an important factor in the evolution of summer floe size distributions [*Arntsen et al.,* 2015].

In addition to melt pond onset, surface roughness influences the pace of melt throughout the melt season as illustrated in Figure 3.6. The formation of discrete ponds on the low-elevation areas of multiyear floes facilitates a melt evolution that is fairly steady throughout the melt season. In contrast, once melt starts on first-year ice, it quickly intensifies and exceeds the pace seen on multiyear ice because of the effects of the smooth surface topography of first-year ice.

3.6 CONCLUSION

The results of this study: (1) demonstrate the utility of the NTM imagery for evaluating seasonal melt pond evolution on drifting sea ice, (2) introduce a newly-developed algorithm for accurately identifying melt pond, sea ice, thin ice, and open water classes, and (3) show the significant impact of ice type and snow thickness distribution on the evolution of the melt season in the drifting ice pack. The latter point is revealed by the considerable differences in the observed melt pond

evolution between the 1998 SHEBA and 2011 APLIS sites, and between drifting first-year and multiyear sea ice at the 2011 APLIS site. There is great potential for developing a four-class product from the NTM imagery capturing the changes of the Arctic surface from a Lagrangian point-of-view. Such a product could be used to validate coarser satellite products and model output so that surface conditions and melt processes can be better represented and understood in sea ice and climate models.

The three week offset in pond formation on first-year and multiyear ice at APLIS underscores the importance of snow, particularly snow depth distributions, on melt onset and melt pond formation. Whether or not the snow conditions at APLIS were anomalous for a mixed ice type zone is an open question, as winter snow redistribution may be affected by the local ice type composition and the number of nearby leads. On a broader scale, Webster et al. [2014] have shown that snow depth distributions on both ice types in the Western Arctic have decreased. Thinner snow may have two effects on seasonal melt pond formation (1) thin snow and the absence of snow expose the sea ice surface to solar radiation earlier in the season which hastens melt, and (2) less freshwater may be available during early pond formation to form low-salinity ice surface layers [*Eicken et al.,* 2002]. This finding motivates future observations of melt pond evolution as the Arctic sea ice pack continues to shift towards a more seasonal sea ice regime, and as snow accumulation on Arctic sea ice is projected to decrease [*Hezel et al.,* 2012]. The specific roles of snow distribution, surface topography, and ice type variability on the seasonal melt pond evolution on drifting Arctic sea ice may be better understood through continued combined efforts from the modeling and observational communities, especially with respect to sea ice predictability.

Chapter 4. Spatial scaling of melt pond distributions

ABSTRACT

Melt ponds play a critical role in the ice-albedo feedback of Arctic sea ice; melt ponds absorb five times more solar radiation than bare sea ice, increase the pace of melt, and thus their distribution affects the survivability of Arctic sea ice during the summer melt season. This study examines the spatial scaling of melt pond distributions and studies the links between small-scale variability in melt pond geometry, snow and sea ice thickness, and aggregate-scale estimates of melt pond fractions. Data from field sites of two programs, "Determining the Impact of Sea Ice Thickness on the Arctic's Naturally Changing Environment" (DISTANCE) in 2011 and "Marginal Ice Zone" (MIZ) in 2014, were used to examine melt ponds on two floes with homogenous (undeformed first-year) and heterogeneous (mixed deformation and age) sea ice in the Beaufort and Chukchi seas. The results reveal that: (1) melt pond geometry is most variable during maximum coverage prior to melt pond drainage at the heterogeneous site, but after pond drainage at the homogenous site, (2) aggregate-scale estimates of melt pond fractions in homogenous and heterogeneous sea ice environments are larger than previously recognized, ranging from ~70 km^2 to ~480 km^2, and (3) aggregate-scale estimates of melt pond fractions may be dependent on the composition of sea ice and stage of melt pond evolution, the latter of which was revealed by the 2011 DISTANCE site, which exhibited the largest aggregate-scale prior to melt pond drainage. These data on the heterogeneity of melt pond distributions may be useful for parameterizing melt pond processes in high-resolution numerical models and designing future experiments for field data collection.

4.1 INTRODUCTION

The Arctic sea ice cover is undergoing a physical transformation due to climate change [*Kirtman et al.,* 2013; *Stocker et al.,* 2013]. Sea ice thickness [*Kwok and Rothrock,* 2009; *Lindsay and Schweiger,* 2015] and extent [*Parkinson and Cavalieri,* 2008; *Cavalieri and Parkinson,* 2012] are decreasing, and the Arctic sea ice cover is transitioning towards a seasonal state in which the Arctic is projected to be sea ice-free in September [*Kirtman et al.,* 2013; *Stocker et al.,* 2013]. To date, the Arctic sea ice pack, defined as sea ice that drifts with the ocean currents and surface winds [*Untersteiner,* 1986], has been a composite of sea ice age ranging from young sea ice in frozen leads to multiyear sea ice over ten years of age. The relationships between sea ice age, its geophysical properties, and their effects on sea ice processes have been well-established from a foundation of observational data [*Untersteiner,* 1986; *Wadhams,* 2000; *Eicken et al.,* 2009; *Thomas and Dieckmann,* 2010]. What is less well-understood is how the heterogeneity in sea ice types affects sea ice processes, such as melt pond evolution, and the spatial scales over which these effects persist.

At the end of the melt season, whatever sea ice that remains is integrated into a network of young ice types (frazil, grease, nilas, and others) as sea ice freeze-up occurs. By mid-autumn, small sea ice floes, hereafter referred to as "sub-floes," freeze together to create larger, conglomerate floes that resemble a patchwork of sea ice thickness and deformation. Satellite imagery reveals that such conglomerations of sub-floes yield equally-patchy distributions of melt ponds in summer (Figure 4.1). Particularly in heterogeneous sea ice environments, a statistically-representative estimate of melt pond distributions is highly dependent on the spatial scale over which they are

investigated. Thus, such estimates are subject to errors if the spatial extent of study areas is too small to fully capture the intra-floe heterogeneity in melt pond distributions.

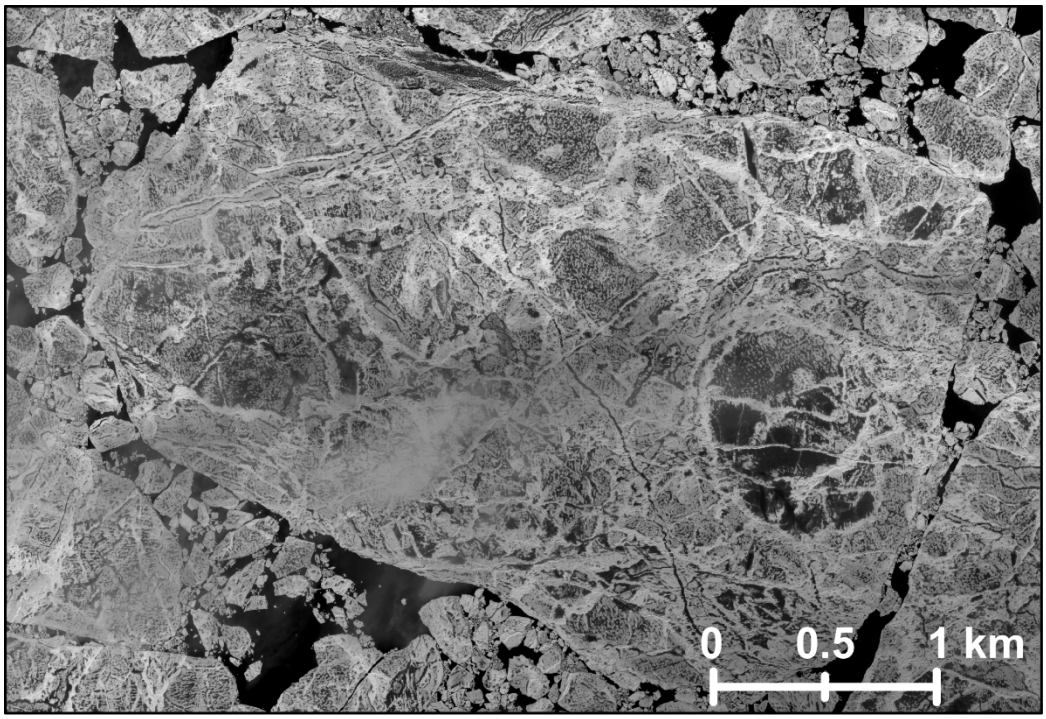

Figure 4.1 Sea ice in the marginal ice zone of the Beaufort Sea on 1 July 2014. Note the large intra-floe heterogeneity in melt pond distributions, and the appearance of "sub-floes," or remnants of smaller floes that make up a larger, conglomerate floe.

Observations of small-scale, melt pond processes and large-scale, melt pond coverage have been critical for developing and improving parameterizations of melt ponds in sea ice models [*Flocco et al.,* 2010; *Hunke et al.,* 2013]. With advances in high-resolution numerical modeling, however, model resolutions are now approaching the spatial scales (one to several kilometers) at which the small-scale heterogeneity in melt pond distributions (Figure 4.1) is a necessary consideration for accurate simulations of processes, such as the partitioning of solar radiation and

the associated sea ice melt [*Perovich et al.,* 2002b; *Perovich and Polashenski,* 2012]. Despite its importance, the spatial scaling of melt pond heterogeneity has remained poorly understood due to the challenge in gathering coincident data over the necessary range in spatial scales for its investigation.

In this study, we use a combination of in situ, airborne, and satellite data to investigate the spatial scaling of melt ponds distributions in two contrasting environments: (1) a homogenous sea ice case, predominantly composed of undeformed first-year sea ice, and (2) a heterogeneous sea ice case, composed of a mixture of deformed and undeformed first-year, second-year, and multiyear sea ice types. Our objectives are to examine the spatial heterogeneity in melt pond distributions from meter- to ~25 kilometer-scales, and link small-scale variability in melt pond geometry to aggregate-scale estimates of melt pond coverage. We define aggregate scale as the spatial scale over which estimates of melt pond coverage are statistically representative of the sea ice surface following Perovich and Tucker [1997]. We hope that these results will aid the development and improvement of melt pond parameterizations in high-resolution numerical models, and serve as a guide for the experimental designs in field data collection.

4.2 BACKGROUND

In this section, we present an overview of the factors that control the seasonal evolution of melt ponds: sea ice permeability, flaws within the sea ice structure, sea ice surface topography, and surface meltwater [*Eicken et al.,* 2002; *Eicken et al.,* 2004; *Polashenski et al.,* 2012]. These factors dictate the timing of melt pond formation, growth, and drainage, and thereby affecting the temporal changes in melt pond distributions.

Low sea ice permeability is essential for melt pond formation to occur, and it can result from one of two processes: (1) meltwater flushing and freezing within sea ice that survives at least one summer melt season, and (2) the addition of freshwater into the sea ice surface via surface meltwater and rainfall. The primary source of surface meltwater is melted snow [*Eicken et al.,* 2002] and, as such, surface meltwater is mostly fresh. As meltwater percolates downward into the sea ice surface, the meltwater comes in contact with sea ice that is cooler than its freezing temperature, which triggers the formation of a sub-surface, superimposed ice layer [*Eicken et al.,* 2002; *Eicken et al.,* 2004]. The sub-surface ice layer is an impenetrable layer of freshwater ice over which meltwater pools to form melt ponds. When melt ponds develop, the surface albedo decreases, causing more solar radiation to be absorbed and transmitted in ponded sea ice relative to bare sea ice [*Perovich et al.,* 2002a; *Perovich and Polashenski,* 2012]. Warming from solar absorption, in turn, causes sea ice under melt ponds, including any sub-surface ice layers, to become more permeable [*Eicken et al.,* 2002; *Eicken et al.,* 2004; *Golden et al.,* 2007]. When sea ice permeability reaches about ~0.05 [*Golden et al.,* 2007], melt ponds drain through sea ice. Melt pond drainage flushes interior brine channels with meltwater, of which ~70% ends up in the underlying ocean and the remaining ~30% can be refrozen within the sea ice structure [*Eicken et al.,* 2002]. Flaws and cracks within sea ice also affect the timing of melt pond drainage by providing outlets for surface meltwater to drain through early during the melt season when sea ice permeability is still low [*Eicken et al.,* 2002; *Polashenski et al.,* 2012].

Surface topography plays multiple roles in melt pond evolution (Figure 4.2). Indirectly, surface topography modifies the amount of available snowmelt via the topographic effects on wind-driven snow redistribution during winter [*Radionov et al.,* 1997; *Sturm et al.,* 2002b]. In the presence of strong winds, rough topography, such as ridged and rubbled sea ice, traps drifting snow

in surface depressions, which leads to a deep, heterogeneous snow depth distribution [*Radionov et al.,* 1997; *Sturm et al.,* 2002b], from which more meltwater is generated in summer. In contrast, undeformed sea ice typically develops a thinner, more uniform snow cover [*Radionov et al.,* 1997; *Sturm et al.,* 2002b] and consequently less meltwater, due to the absence of topographic features which impede drifting snow. In summer, topography directly controls the spread of meltwater on the sea ice surface; ridges and hummocks confine the horizontal spread of pooled meltwater, and thus limit the areal fraction of melt ponds [*Fetterer and Untersteiner,* 1998; *Eicken et al.,* 2002; *Perovich et al.,* 2002b*; Eicken et al.,* 2004]. The smooth surface of undeformed sea ice has the opposite effect; meltwater spreads laterally and thinly, which yields large areal fractions of melt ponds [*Fetterer and Untersteiner,* 1998; *Perovich et al.,* 2002b; *Webster et al.,* 2015].

Melt ponds have three major sources of meltwater: (1) snow melt, which is the primary source, (2) sea ice melt, and (3) meltwater transported from higher surface elevations, such as ridges and hummocks, to lower surface elevations (Figure 4.2) [*Eicken et al.,* 2002]. During the Surface Heat Budget of the Arctic Ocean (SHEBA) field campaign, the snow cover was removed from sea ice on the site's runway. Interestingly, the snow removal inhibited melt pond formation during the summer melt season, as there was no source of freshwater to form a superimposed, sub-surface ice layer [*Eicken et al.,* 2004]. The results show that snow is a critical component for melt pond evolution, and changes in snow depth, distribution and density may impact the amount of available meltwater for melt pond growth.

Lateral meltwater transport plays an important role in the growth of melt ponds (Figure 4.2), particularly during the early melt season and summer-round on deformed sea ice [*Eicken et al.,* 2002]. Meltwater flows down sloped surfaces and accumulates into local topographic depressions, and, depending on the surface elevation gradients, meltwater can travel over 16

meters across the sea ice surface [*Eicken et al.,* 2002]. Throughout summer, lateral meltwater transport on deformed sea ice types produces deep, narrow melt ponds, such as those commonly observed on multiyear sea ice [*Fetterer and Untersteiner,* 1998; *Perovich et al.,* 2002b]. Rainfall during the melt season also contributes to melt pond formation, but the frequency and magnitude of rainfall events over Arctic sea ice are currently unknown. Global climate models project an increase in Arctic rainfall events during summer [*Stocker et al.,* 2013], which may make rainfall a more significant source of freshwater for melt pond growth in the future.

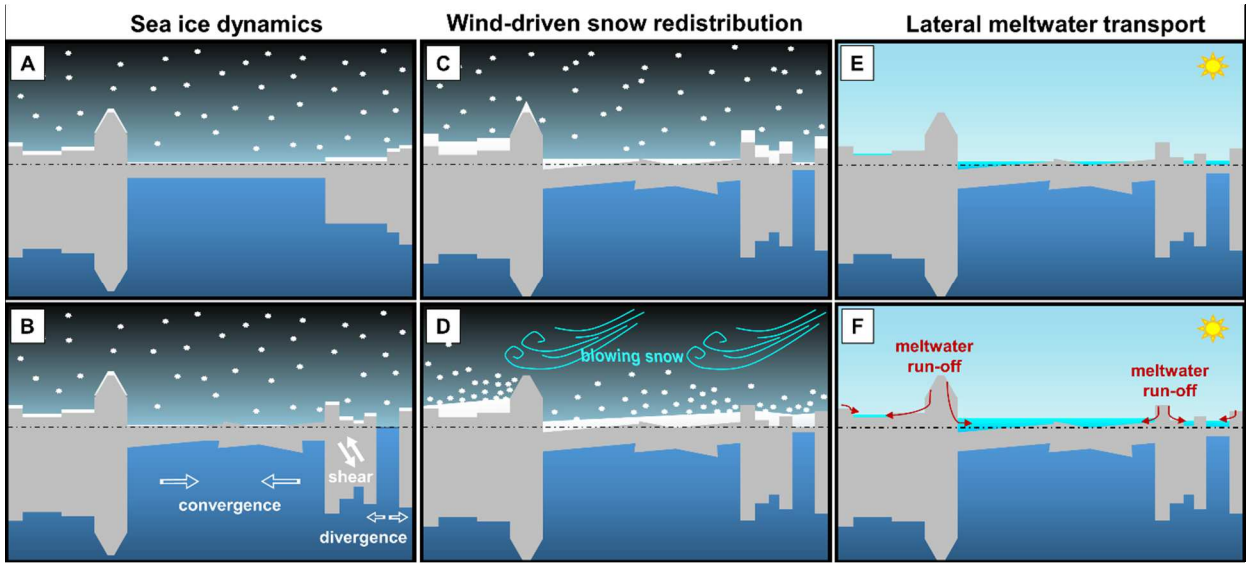

Figure 4.2 An overview of processes that have indirect and direct effects on melt pond evolution and distributions. **(A–B)** Sea ice dynamics reshape the surface topography of the sea ice, which affects the distribution of snow and melt ponds in the following seasons. Depending on the age of the sea ice, sea ice may have pre-existing topographic features, such as ridges and rubble, from dynamic events in previous years. **(C–D)** In autumn, storms bring heavy snowfall and strong winds, which redistribute the snow on the sea ice surface. On exposed topographic features, like ridges, snow is blown off and deposited onto topographic depressions, where it can remain trapped

throughout winter. In summer, deep snow provides more meltwater for melt pond formation. **(E–F)** As summer melt progresses, meltwater drains down sloped sea ice surfaces and accumulates in the local low-lying areas, contributing to melt pond growth.

4.3 DATA

We synthesized results from several data sources to examine the heterogeneity and spatial scaling of melt pond distributions at two sites with contrasting surface topographies. This study uses observations from the 2011 field campaign of the project called "Determining the Impact of Sea Ice Thickness on the Arctic's Naturally Changing Environment" (DISTANCE) [*Gardner et al.,* 2012] and from the 2014 cluster 2 site of the "Marginal Ice Zone Program" (MIZ) project [http://www.apl.washington.edu/project/project.php?id=miz] in the Beaufort and Chukchi seas (Figure 4.3). The sites were chosen for their abundance of coincident buoy, airborne, and satellite data.

We focused on two sub-floes, one from each site, approximately four km^2 in size. The 2011 DISTANCE sub-floe was composed of undeformed first-year sea ice and surrounded by predominantly undeformed first-year sea ice; multiyear sea ice made up less than five percent of the study area [*Webster et al.,* 2015]. The 2014 MIZ sub-floe was a mixture of deformed and undeformed first-year, second-year, and multiyear sea ice. Here we introduce the different data sources including buoy, airborne, and satellite from the 2011 DISTANCE and 2014 MIZ sites.

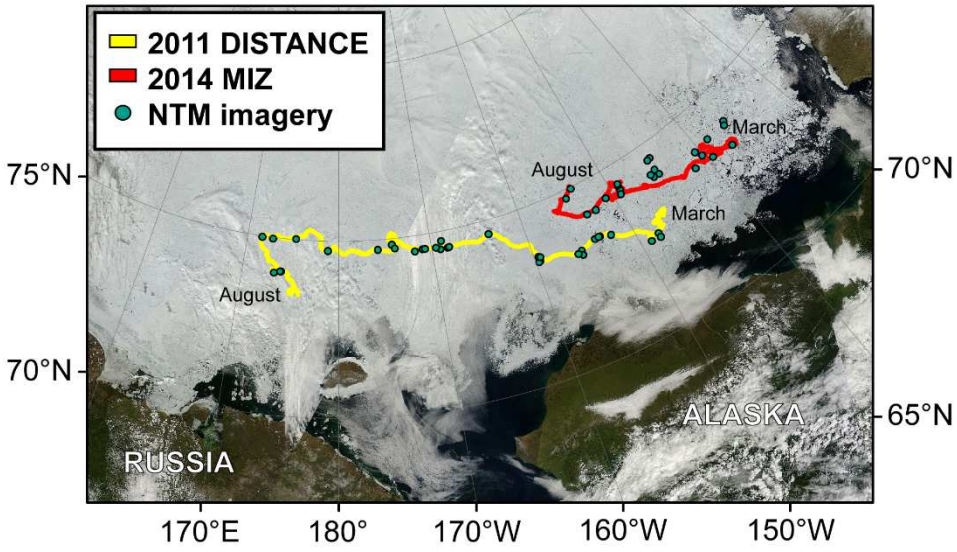

Figure 4.3 The drift tracks of the 2011 DISTANCE site (yellow) and 2014 MIZ cluster 2 site (red) from March to August. The turquoise dots represent locations of National Technical Means (NTM) image acquisitions tracking International Arctic Buoy Programme (IABP) buoys 732080 (2011), 533365 (2014), and 620250 (2014). The background image is a true color Moderate Resolution Imaging Spectroradiometer (MODIS) mosaic at one kilometer resolution for 9 July 2014 [MODIS data are available at https://ladsweb.nascom.nasa.gov/].

4.3.1 *Ice mass balance buoy*

The Cold Regions Research and Engineering Laboratory's Ice Mass Balance (IMB) buoy "2014C" was deployed on 19 March 2014 at MIZ cluster 2 [*Perovich et al.,* 2013]. IMB 2014C aimed to provide seasonal insight into the changing surface conditions of the sub-floe until 24 August, when the buoy melted free. IMB buoys are equipped with a sonic range-finder which measures the time between a transmitted and backscattered pulse from the air-snow or air-ice interface. This

information, together with the initial snow depth from when the buoy was deployed, were used to derive hourly snow thickness estimates, which were then used to determine snow accumulation events and surface melt. Thermistors were placed ten centimeters apart along the buoy, from the top, through the snow and sea ice, and into the underlying surface ocean, giving a full vertical temperature profile with a 0.1°C accuracy from which surface and bottom melt rates and heat fluxes were estimated.

4.3.2 *Airborne data*

Airborne data were collected as part of NASA's Operation IceBridge, an airborne mission dedicated to bridging the gap between the Ice, Cloud and land Elevation Satellite (ICESat) and ICESat-2 satellite missions of measuring ice thickness over sea ice, glaciers, and ice sheets [*Koenig et al.,* 2010]. Operation IceBridge conducted 13 passes over the DISTANCE field site on 23 March 2011 and ten passes over the MIZ cluster 2 site on 18 March 2014 with a P-3 aircraft equipped with an array of instruments. Three of the IceBridge data sets were used: RGB imagery from the Digital Mapping System (DMS), the snow and sea ice thickness Quicklook product derived from the University of Kansas' snow radar, and relative surface elevations from the Airborne Topographic Mapper (ATM). The DMS images are orthorectified and geolocated, and have a horizontal resolution of ten centimeters at the nominal flight altitude of 460 m [*Dominguez,* 2010], and aided in the co-location of data onto the same reference plane. The Quicklook snow and ice thickness estimates provided information on the pre-melt conditions of the main floe, yielding 40-m snow and ice thickness averages along the flight path. The associated uncertainties are 5.7 cm and ~51 cm for snow and sea ice, respectively [*Kurtz et al.,* 2013b]. The ATM is a spiral scanning

laser altimeter with a single-shot vertical accuracy of five to seven centimeters depending on the surface roughness within the laser footprint [*Krabill,* 2010; *Farrell et al.,* 2012; *Martin et al.,* 2012].

4.3.3 *Satellite imagery*

Declassified, one-meter grayscale images from the National Technical Means (NTM) were used to evaluate the changes in melt pond geometric properties and fractions as the summer melt seasons progressed. The images are publicly available at the Global Fiducials Library [gfl.usgs.gov]. Images are stretched to 256 grayscale levels, radiometrically inconsistent, and typically ~15 km by ~15 km in size [*Kwok,* 2013], but are sometimes stitched together to create larger, composite images ~30 km by ~30 km in size. Some images are tasked to static coordinates, while others track the GPS coordinates of drifting buoys. In this study, images tasked to (IABP) 2011 DISTANCE buoy 732080 and (IABP) 2014 MIZ buoys 533365 and 620250 were analyzed.

4.4 METHODS

4.4.1 *NTM imagery*

The two sub-floes of interest were chosen based on the location of the Operation IceBridge passes and on the sub-floes' large summer melt pond fractions and ability to remain intact despite dynamic events throughout summer. Both sub-floes were comparable in size, ranging from over two km^2 to four km^2 until late August, when profuse melt and breakup reduced the sea ice

concentration to ~20% at both sites, as calculated from the NTM imagery. The 2011 DISTANCE sub-floe was identified as FY ice, and 2014 MIZ sub-floe was a mixture of sea ice types.

Melt ponds were identified in the NTM imagery following Webster et al., [2015]. The algorithm can be described as an automated decision tree that uses grayscale values of similar interconnected pixels and compares their grayscale statistics with neighboring pixels for classification as sea ice, melt ponds, or open water. Owing to foggy conditions in the 1 July NTM image of the 2014 MIZ site, the algorithm thresholds were modified to avoid misclassification of melt ponds in this particular scene. The thresholds were manually determined based on training sets over the main sub-floe; the algorithm thresholds are listed in Table 4.1. Between 1 July and 30 July, scenes of the MIZ sub-floe were limited, either due to deteriorated atmospheric conditions, or poor coverage in the scene acquisition. However, the cloud cover was sufficiently transparent to visibly discern the progression of melt pond evolution (Figure 4.4).

Table 4.1 Modified algorithm thresholds[a]

Thresholds	Value
Threshold (A)	114
Threshold (B)	46
Threshold (C)	131
Object Mode	56

[a]Thresholds for the algorithm in Webster et al. [2015] were modified to prevent misclassifications of melt ponds in foggy conditions in the 1 July 2014 NTM image tracking buoy 533365 at the 2014 MIZ site. The thresholds were determined using training sets over the sub-floe of interest. Without any modifications, Threshold (A) is the first standard deviation of the grayscale intensities of the scene, Threshold (B) is the mean of interconnected pixels whose binned and numerically-

increasing derivative is equal to one, Threshold (C) is the upper grayscale limit, defined as 1.75 times Threshold (A), used to analyze pixels of light-colored melt ponds and dark sea ice, and Object Mode is used for separating open water from the melt pond class in cases where melt ponds are located on thin sea ice and, hence, have a similarly dark intensity as open water.

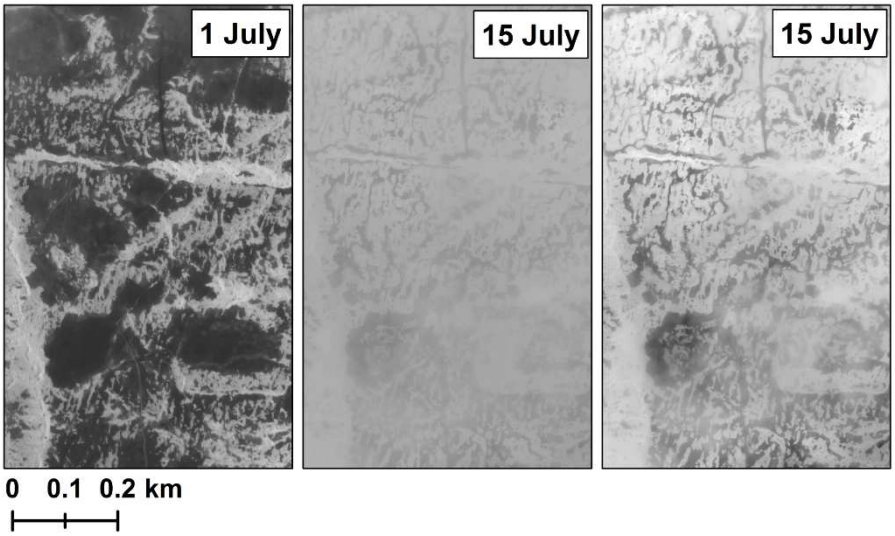

Figure 4.4 Left: Maximum melt pond coverage on 1 July 2014 at the MIZ site. **Middle:** The 15 July 2014 NTM scene of the same area after melt pond drainage had occurred. The scene was too foggy to extract melt pond fractions. **Right:** The same 15 July 2014 NTM scene of the same area with a stretched grayscale histogram; the histogram was horizontally stretched to improve the visibility of drained melt ponds.

4.4.2 *Data co-location*

A challenge in analyzing data collected over drifting sea ice is the discrepancy in data location due to sea ice drift. On 18 March at the 2014 MIZ site, the sea ice drifted north-northwest, accelerating

from 0.15 m s^{-1} to 0.23 m s^{-1} with a slight rotation while Operation IceBridge conducted passes over the field site. To co-locate the IceBridge Quicklook product onto the NTM imagery, tie points were created between the DMS and NTM images. Surface features such as leads, thin ice, rubble, and ridges were easily identifiable in both sets of imagery and thus provided effective tie points for linking the airborne and satellite images. On average, 13 DMS images were used per airborne pass of the main floe, with three tie points per image. The same approach was taken for co-locating data over the 2011 DISTANCE sub-floe since it had broken away from a larger ice floe equipped with a buoy array for tracking sea ice drift [*Webster et al.,* 2015].

4.4.3 *Surface elevations*

ATM data contain erroneous surface elevation measurements due to conditions where specular reflection can occur (e.g. open water). Consequently, the data require processing to remove erroneous values, as well as to derive surface elevations relative to sea level. Values from recently frozen leads, as identified from DMS imagery, were used as the minimum surface elevations and were subtracted from all ATM measurements to derive surface elevations relative to sea level. This method underestimates the true surface elevation by a few centimeters or less since the minimum surface elevation values are of young sea ice, which has typical freeboard height of two to three centimeters above sea level [*WMO,* 1970; *Johnston and Timco,* 2008]. The underestimation was assumed to be consistent for each field site.

4.4.4 *Geometric properties*

A comparison was made of the melt pond geometric properties between the 2011 DISTANCE and 2014 MIZ sub-floes to investigate which factors influenced their magnitude and behavior during different stages of melt pond evolution. The satellite observations were categorized based on three stages of melt pond evolution: (A) maximum melt pond coverage before drainage, (B) melt pond drainage, and (C) late season melt, just prior to floe breakup. A comparison for melt pond onset was not available due to the lack of NTM imagery of the 2014 MIZ site for this period. Nevertheless, this stage was included for the 2011 DISTANCE site out of interest in melt pond geometry during melt pond onset.

For the purpose of this study, melt ponds that may have melted entirely through the sea ice were classified as melt ponds rather than open water due to the lack of field observations for validation. Melt ponds with an area of one m^2 were discarded from the analysis because their small size was near the resolution limit of the imagery; they comprised less than one percent of the total melt pond fractions for all scenes.

Melt ponds derived from the NTM imagery were analyzed for their geometric properties. Melt pond area, perimeter, and major and minor axis lengths were found using Matlab's Image Processing Toolbox, version 2015b. Major and minor axis lengths were used to evaluate the narrowing and widening of melt ponds and drainage channels as melt pond evolution. Melt pond density and area were used to interpret the relative changes in melt pond interconnectedness due to meltwater accumulation and drainage. Following Perovich et al. [2002b], melt pond density was calculated as the number of melt ponds divided by the sum of the melt pond and sea ice areas of the sub-floes.

Circularity gives information regarding the complexity of melt pond shapes, which may be useful for interpreting the relative amount of lateral melt as melt pond areas and perimeters with each stage of melt pond evolution. Circularity, *C*, was defined as:

$$C = \frac{4\pi A}{P^2} \tag{4.1}$$

where *A* is the melt pond area and *P* is the melt pond perimeter. Values closer to one represent circles; as C decreases, the fractal nature of the melt pond shapes increases.

Unlike the area of a melt pond, the value of its perimeter is dependent on the method used to determine it. With Matlab's Image Processing Toolbox, the perimeter is calculated as the distance between the centers of two pixels along the edge of a melt pond, rather than the distance around the outside of a melt pond. Hence, this approach underestimates the true perimeter of a melt pond. In some cases, this underestimation can lead to a melt pond circularity greater than one, which is not physically possible since the maximum circularity (i.e. a circle) is equal to one. To reconcile this issue, we adapted Equation 4.1 based on the difference in calculating a perimeter of a circle using central distances of border pixels versus the circumference of the circle, which resulted in the addition of π in the squared denominator:

$$C \approx \frac{4\pi A}{(P + \pi)^2} \tag{4.2}$$

4.5 RESULTS

The section 4.5.1 presents the results of the 2014 MIZ site, with Section 4.5.1.1 showing the seasonal evolution, and section 4.5.1.2 showing the comparison of physical properties between the

MIZ sub-floe and its surroundings. Section 4.5.2 presents the results of the 2011 DISTANCE site. We have omitted description of the seasonal evolution at the 2011 DISTANCE site, as it is already well-documented in Webster et al. [2015], which contains specific details of the changing surface conditions from melt pond onset to late season melt and sea ice breakup. Instead, the comparison between the 2011 DISTANCE sub-floe and its surroundings are presented in Section 4.5.2. Sections 4.5.3 to 4.5.5 show the resulting comparisons between the 2011 DISTANCE and 2014 MIZ sites based on their physical properties (Section 4.5.3), melt pond geometries (Section 4.5.4), and melt pond distributions (Section 4.5.5). Lastly, section 4.5.6 presents the results of the spatial scaling analysis in which the aggregate-scale estimates of melt pond coverage were determined for the 2011 DISTANCE and 2014 MIZ sites.

4.5.1 *2014 MIZ site*

4.5.1.1 MIZ *seasonal melt pond evolution*

1. *Pre-melt snow drift conditions:* The Quicklook product and IMB data showed that spring snow depths were ~20–25 cm on the main floe. The IMB buoy measured a sudden depth increase of 26 cm within a four-hour period on 27 April (not shown). The accumulation may have resulted from a change in the orientation of acoustic range finder or the development of a snow drift, because a snowfall of such large magnitude within a four-hour time period is rare for Arctic snowfall events [*Radionov et al.,* 1997; *Warren et al.,* 1999]. Furthermore, no new snow deposition was apparent between the 18 March DMS images and 30 April NTM imagery. Many of the larger, newly frozen-over leads appeared to remain snow-free between March and late April, but some snow drifts changed direction by 90°, indicating that at least one blowing snow event had occurred (Figure

4.5). The buoy drift speed increased for several days from 24 April to 28 April, which is evidence of increased winds and a possible blowing-snow event. Nevertheless, the majority of snow drift bedforms [*Filhol and Sturm,* 2015] kept the same size, shape, and position between March and April. There was no clear pattern in where drift bedforms formed, changed orientation or location, or simply remained the same with respect to wind direction and surrounding surface topography. Due to the rarity of a 26-cm snowfall event, as well as a sudden development of a 26-cm snow drift within a four-hour period [*Radionov et al.,* 1997; *Warren et al.,* 1999], the accumulation event was deemed an instrumental error, and thus the 26-cm snow accumulation was removed from the data (marked in Figure 4.6D).

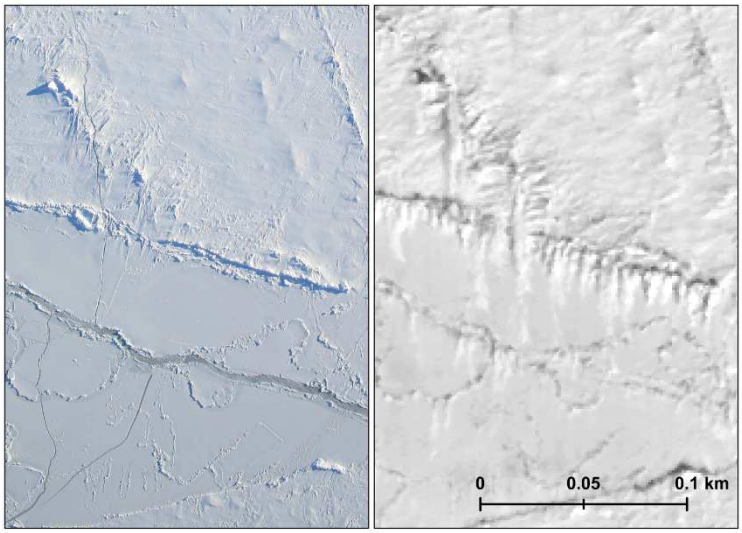

Figure 4.5 Left: The DMS image from 18 March 2014 of the 2014 MIZ site showing no visible snow drifts on a recently-frozen over lead. **Right:** The 30 April 2014 NTM image showing new snow drifts on the frozen lead, after what was presumably a wind event based on the increase in sea ice drift.

2. *Melt onset to maximum pond fractions:* On 6 June, sea ice bottom melt began, and snow melt began one day later. From melt onset and throughout the rest of summer, sea ice bottom melt surpassed surface melt (Figure 4.6). The first melt ponds appeared on 17 June in the NTM imagery. One week later (24 June), melt pond fractions were near their maximum extent. The 1 July NTM scene showed melt pond fractions as high as 64% for over half of the main sub-floe (Figure 4.7); the total sub-floe's melt pond fraction was 56%. The melt pond fraction on the larger, conglomerate floe, of which the sub-floe was part of, was ~31%. By 6 July, snow at the IMB buoy had completely melted.

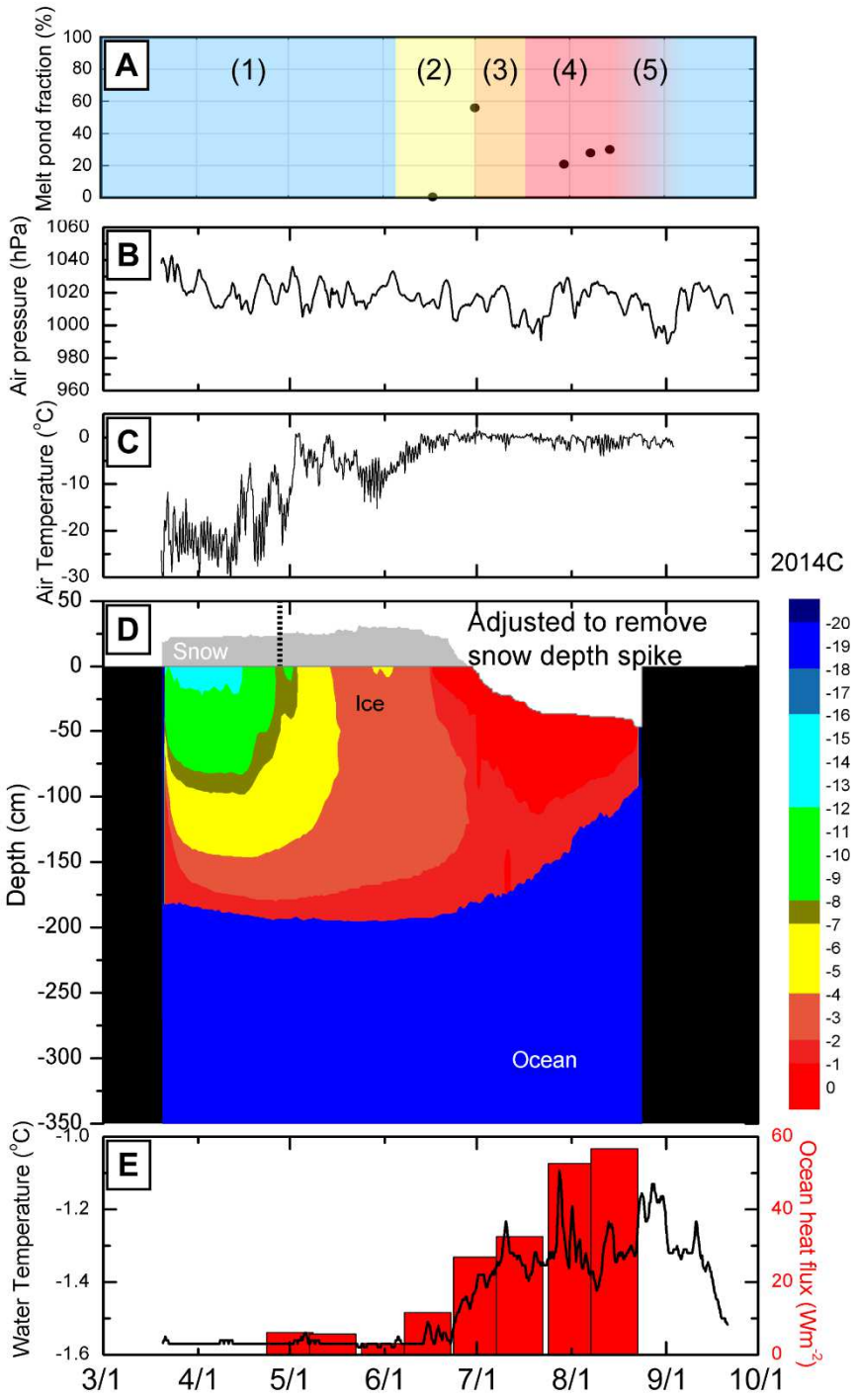

Figure 4.6 (A) Melt pond fractions on the 2014 MIZ sub-floe, derived from NTM imagery. The enumeration and color shading denote different stages of seasonal evolution as described in the text. **(B–E)** IMB buoy data from 2014C for **(B)** sea level pressure, **(C)** air temperature, **(D)** the

temperature profile within the sea ice and surface ocean in degrees Celsius, and **(E)** ocean heat flux (red) and water temperature (black). Snow depth is represented by the grey coloring in panel D; the erroneous 26-cm snow accumulation on 27 April was removed (dashed black line in panel D) to better illustrate periods of snow accumulation and melt over time.

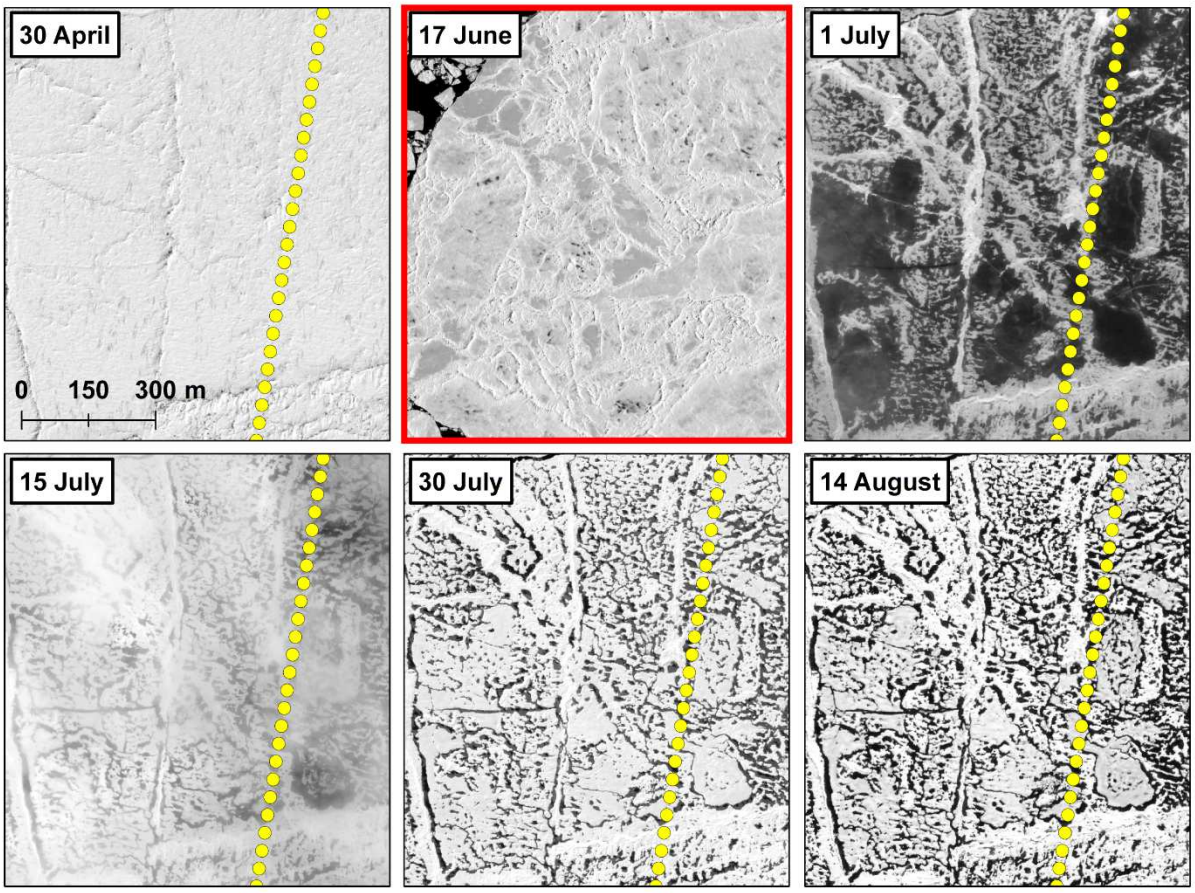

Figure 4.7 Subsets of the sub-floe or sea ice nearby for different stages of surface conditions at the 2014 MIZ site: pre-melt conditions on 30 April, melt pond onset on 17 June, maximum melt pond coverage on 1 July, melt pond drainage on 15 July, after a freeze event and/or scant snowfall accumulation on 30 July, and late season melt on 14 August, just prior to floe breakup. The yellow dots represent the flight path of Operation IceBridge on 18 March 2014. The red border denotes a

subset ~30 km away from the main sub-floe due to the location discrepancy in the scene acquisition. Note, the grayscale histogram of the 15 July NTM scene has been horizontally stretched to improve the visibility of melt ponds despite foggy conditions.

3. *Drainage:* Cloud cover in the 15, 18, and 26 July NTM images made it impossible to retrieve areal melt pond fractions. However, clouds in the 15 July scene were sufficiently transparent to observe that melt pond drainage had occurred on the sub-floe, on the surrounding sea ice, and on ice floes visible in the NTM scene (Figures 4.4 and 4.7). The appearance of drainage channels and above-freezing air temperatures from IMB data (Figure 4.6) confirmed that the decrease in the total melt pond fractions was not due to a freeze or snowfall event. Despite a decrease in total melt pond fractions, a few melt ponds on along ridged sea ice grew in size, which is consistent with previous observations of the topographic effects on melt pond evolution [*Webster et al.,* 2015]; melt pond growth and drainage are temporally heterogeneous on sea ice with rough surface topography, such as ridges and MY ice. In contrast, melt ponds on sea ice with smooth topography, like undeformed FY ice, undergo growth and drainage at approximately the same time on sea ice.

4. *Late summer freeze and melt:* On 30 July, the sub-floe appeared to have undergone either freezing or snow accumulation, or both, as drainage channels became partially obscured but fully reappeared two days later in the 2 August scene (not shown due to limited coverage of the sub-floe in the 2 August NTM scene). IMB data displayed a two-centimeter increase in the air-snow-ice interface on 25 July, and air temperatures that hovered below 0°C until 31 July. Any effects of freezing or accumulated snow were relatively short-lived, as melt ponds increased from 21% to 28% by 8 August (Figure 4.6). Between 8 August and 14 August, melt pond fractions increased

by two percent (Figure 4.6), and patches of smooth, bare ice that were once covered by melt ponds darkened significantly during this six-day period (Figure 4.7). The darkening of the sea ice surface may have resulted from one of two processes: (1) the growth of new melt ponds which are on the verge of becoming fully developed and visible through a snow cover, or (2) melting sea ice that has become optically-thin and thus transparent so that the underlying ocean, which has a low albedo of 0.07, is visible. We speculate that, in this case, the sea ice had become optically-thin due to large ocean heat fluxes and bottom melt rates in August (Figure 4.6 D-E).

5. *Breakup and freeze-up:* On 30 August, open water covered ~77% of a ~600 km^2 area, and the remaining ice consisted of rotten ice floes and fragments that showed signs of freezing. By 25 September, pancake, nilas, and grease ice made up the majority of the scene, and surrounded the remaining fragments of rotten ice. By definition, these remaining floes are second-year or multiyear sea ice, yet they did not exhibit many of the geophysical characteristics of second-year and multiyear floes [*WMO,* 1970; *Johnston and Timco,* 2008]; for example, instead of having well-rounded and defined shapes, their edges were dendritic, owing to break points where melt ponds had melted through and sufficiently weakened the sea ice structure for floe breakage to occur [*Arntsen et al.,* 2015; *Webster et al.,* 2015]. Given the projected decrease in older sea ice types in the Arctic and increase in open water in summer, it may become more difficult to distinguish older sea ice types in the marginal ice zone due to the extreme melt that surviving floes are likely to undergo. Thus it may be helpful to identify these surviving sea ice fragments as “rotten MY sea ice” to avoid ambiguity in the identification of MY sea ice.

4.5.1.2 *MIZ 2014 sub-floe vs. surroundings*

The 2014 MIZ sub-floe was identified as deformed first-year sea ice surrounded by a mixture of deformed and undeformed first-year, second-year, and multiyear sea ice. Relative to the surrounding sea ice, the sub-floe was thinner by ~50 cm and less deformed based on the standard deviation in sea ice thickness (Figure 4.8). The thickness of the surrounding sea ice had a standard deviation over a meter on average, indicating significant variability in sea ice age and deformation, the latter of which was evident by the prevalence of ridges in the NTM imagery (Figure 4.9).

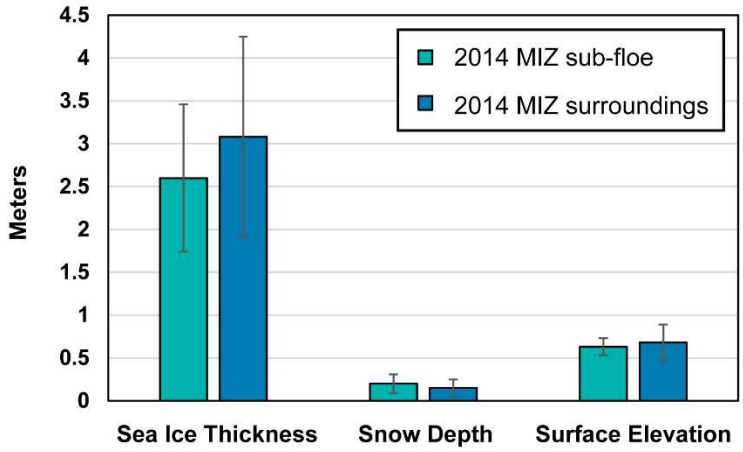

Figure 4.8 Sea ice thickness, snow depth, and surface elevation data of the sub-floe and surrounding sea ice, which were collected during the Operation IceBridge airborne campaign on 18 March 2014 over the MIZ field site.

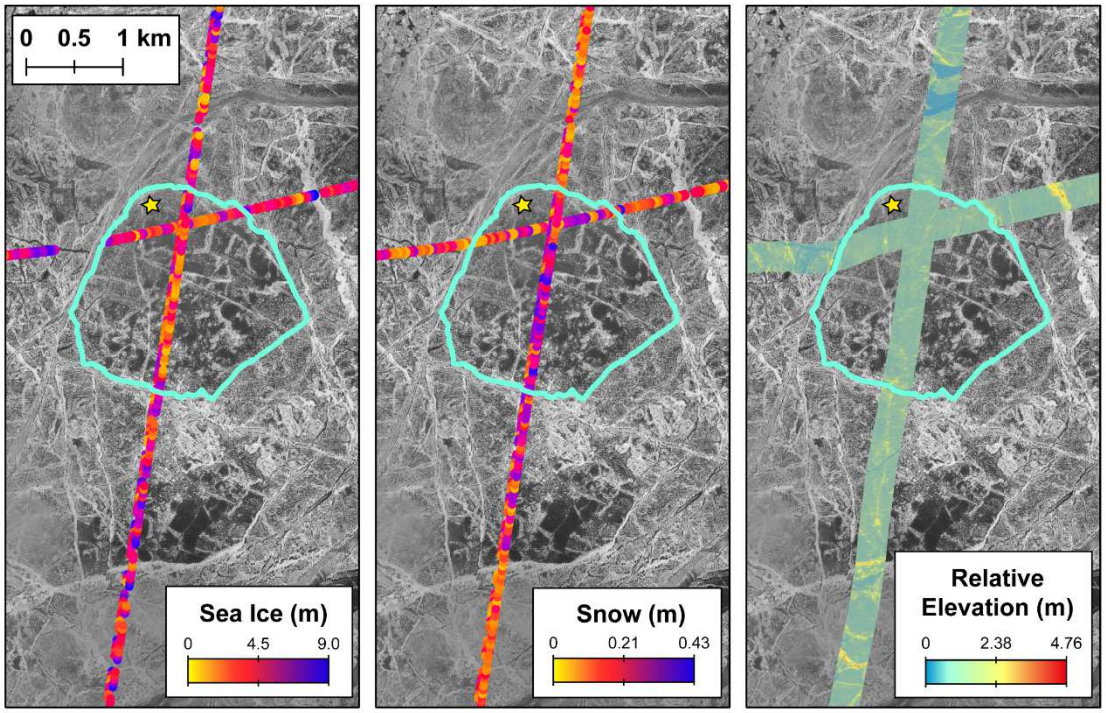

Figure 4.9 The 2014 MIZ site overlaid with Operation IceBridge data products of **(Left)** sea ice thickness, **(Middle)** snow depth, and **(Right)** relative surface elevations in the 1 July 2014 NTM scene. The sub-floe is highlighted in cyan, and the yellow star is the location of IMB 2014C.

Interestingly, the sub-floe had, on average, five centimeters more snow than the surrounding sea ice (Figure 4.8), despite the sub-floe being younger and consequently having less time to accumulate snow [*Thomas and Dieckmann,* 2010; *Webster et al.,* 2015]. The snow surface of the sub-floe was particularly smooth with few snow drift bedforms, and no distinction could be made between the characteristics of its snow surface and that on the surrounding sea ice; both exhibited few snow drift bedforms.

During maximum melt pond coverage, melt pond fractions on the sub-floe were 15% larger than those in the surrounding area. Based on the NTM imagery, the timing of melt pond drainage on the sub-floe and surrounding sea ice was the same. After drainage occurred, melt pond fractions

on the sub-floe and surrounding sea ice became approximately equal, and remained so throughout the rest of the melt season.

4.5.2 *2011 DISTANCE site*

The 2011 DISTANCE sub-floe was primarily composed of undeformed first-year sea ice and had a snow cover consisting of well-developed drift bedforms, of which barchans and sastrugi were the dominant features [*Filhol and Sturm,* 2015]. The five-kilometer-by-five-kilometer area around the sub-floe consisted of ~85% first-year sea ice, most of which was undeformed, and five percent multiyear sea ice [*Webster et al.,* 2015]. The sub-floe had a handful of ridges that separated expanses of level sea ice, which was characteristic of the surface topography of most sea ice in the surrounding area. The surrounding sea ice was ~40 cm thicker, on average, than the sub-floe (Figure 4.10). The sub-floe's averages for snow depth distribution and surface elevations were comparable to those of the surrounding sea ice (Figure 4.10).

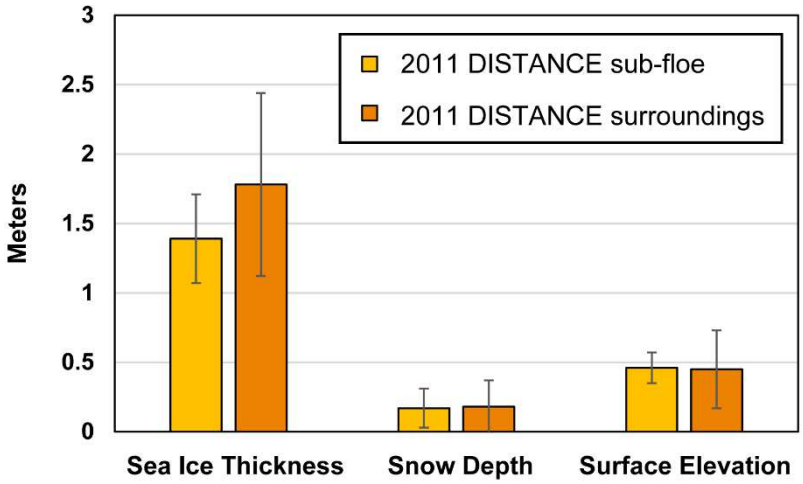

Figure 4.10 Sea ice thickness, snow depth, and surface elevation data of the sub-floe and surrounding sea ice, which were collected during the Operation IceBridge airborne campaign on 23 March 2011 over the DISTANCE field site.

Throughout the seasonal evolution of melt ponds at the 2011 DISTANCE site, the melt pond behavior, fractions, and distributions on the sub-floe were similar to those on the surrounding sea ice with the exception of multiyear floes that were present. In mid-June when melt ponds began to appear, melt ponds on the sub-floe and the surrounding sea ice oriented around snow drift bedforms and remained aligned for the duration of sea ice's presence (Figure 4.11). Just prior to sea ice breakup, ~56% of the sub-floe was covered by melt ponds, and melt ponds covered ~53% of sea ice in the entire 23 July NTM scene, which covered a ~14 km by ~14 km area [*Webster et al.,* 2015]. We speculate that the three percent different in melt pond fractions, as well as the discrepancy in sea ice thickness between the sub-floe and surroundings, may have resulted from the presence of deformed first-year sea ice and multiyear ice floes surrounding the sub-floe, which would have contributed to thicker sea ice and lower melt pond fractions in the sub-floe's surroundings.

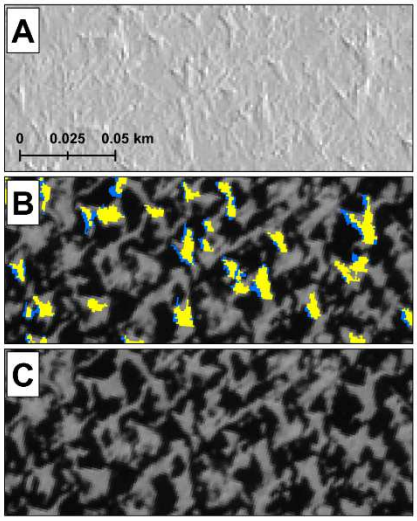

Figure 4.11 (**A)** A subset of the 2011 DISTANCE sub-floe on 28 April, when barchans, which are snow drift features characterized by a crescent shape, were ubiquitous on the surface. **(B)** Highlighted areas where barchans were present in spring, on the 23 July 2011 NTM scene. Yellow denotes areas of bare sea ice; blue represents melt ponds. Approximately 70% of the detected barchans remained free of melt ponds during summer. **(C)** The 23 July 2011 NTM scene, without the highlighted snow drift bedforms. The majority of melt ponds remained aligned around the drift bedforms throughout the melt season. Note that each subset has the same spatial scale.

4.5.3 *DISTANCE site is less heterogeneous than MIZ site*

Overall, the 2011 DISTANCE site was less heterogeneous than the 2014 MIZ site based on the standard deviation in the sea ice thickness of its sub-floe and the sub-floe's surroundings (Figure 4.12). The MIZ site's sea ice thickness was considerably larger and more variable due to the mixed composition of sea ice types. Average snow depths were within five centimeters between sites,

sub-floes, and surroundings, and showed no clear relationship with the average or variability in sea ice thicknesses. The DISTANCE surface elevations were lower, but more variable than those from the MIZ site. We speculate that the larger variability at DISTANCE may have been due to the presence of well-developed drift bedforms and highly deformed MY ice, the latter of which made up a small fraction of the sub-floe's surroundings.

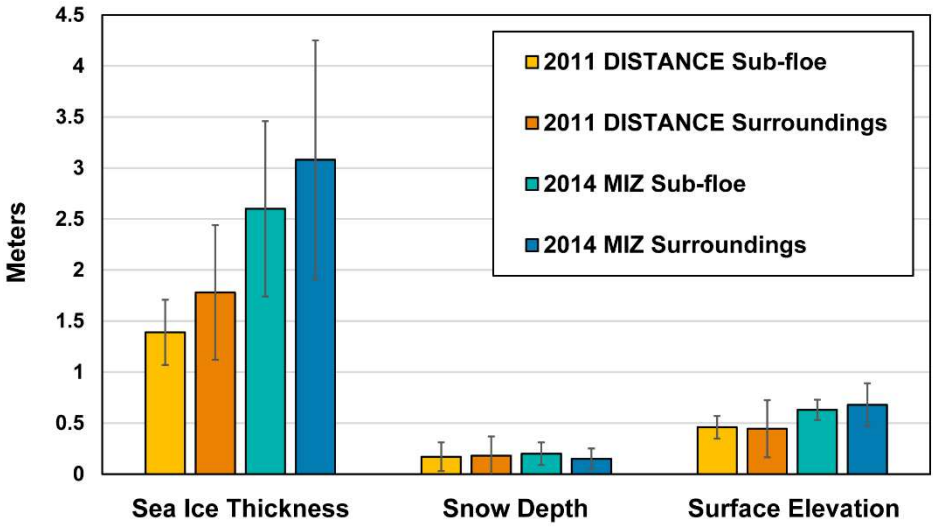

Figure 4.12 Sea ice thickness, snow depth, and surface elevations for the 2011 DISTANCE (yellow shades) and 2014 MIZ (blue shades) sub-floes and their surroundings within five kilometers. The standard deviations are shown as error bars. The means and standard deviations are provided in Table 4.2.

Table 4.2 Physical properties of sub-floes and their surroundings[a]

	Sub-floe thickness (m)	Sub-floe snow (m)	Sub-floe elevation (m)	Surrounding thickness (m)	Surrounding snow (m)	Surrounding elevation (m)
DISTANCE	1.39 (0.32)	0.17 (0.14)	0.46 (0.11)	1.78 (0.66)	0.18 (0.19)	0.45 (0.28)
MIZ	2.60 (0.86)	0.20 (0.11)	0.63 (0.10)	3.08 (1.17)	0.15 (0.10)	0.68 (0.21)

[a]Mean values for sea ice and snow thickness, and relative surface elevations at the 2011 DISTANCE and 2014 MIZ sub-floes and the surrounding sea ice within a five-kilometer radius. The standard deviation is provided in parentheses. The DISTANCE measurements were collected on 23 March 2011; the MIZ measurements were collected on 18 March 2014.

4.5.4 *DISTANCE melt pond geometry is less heterogeneous than MIZ*

The effects of smooth and rough surface topography are illustrated by the differences in the melt pond geometries between the 2011 DISTANCE and 2014 MIZ sites. The 2011 DISTANCE melt ponds were uniform in shape, size, and orientation as result of the smooth surface topography, while the 2014 MIZ melt ponds were more irregular in shape, size, and orientation owing to the complex surface topography.

The maximum circularity of melt ponds was observed during melt pond onset at the 2011 DISTANCE site, which is consistent with previous works that attributed large circularity to pooled meltwater that had recently become visible during the early melt season [*Hohenegger et al.,* 2012]. The DISTANCE melt ponds had Euclidean shapes, with the exception of a few that formed along young (frozen-over) leads and boundaries between rafted and ridged sea ice, which added variability to the axis dimensions (Table 4.3). It should be noted, however, that the shapes of the early DISTANCE melt ponds were not perfect circles; the average of their major axes was more

than double the average of the minor axes, which may have resulted from the orientation of the sub-floe's snow drift bedforms, which control the location of melt pond formation on undeformed sea ice (Figure 4.9) [*Petrich et al.,* 2012a].

Table 4.3 Melt pond geometric properties[a]

	C, Circularity	Perimeter (m)	Major axis (m)	Minor axis (m)	Fraction (%)	Area (m^2)	Density (km^{-2})
(Onset) DISTANCE, 17 June 2011	0.84	9 (14)	5 (5)	2 (2)	1	11 (28)	1.19
(A) DISTANCE, 28 June 2011	0.75	35 (371)	9 (22)	5 (14)	56	119 (3,839)	3.70
(B) DISTANCE, 7 July 2011	0.73	30 (331)	9 (19)	4 (10)	34	64 (1,468)	5.28
(C) DISTANCE, 23 July 2011	0.81	34 (680)	7 (35)	4 (22)	56	315 (11,249)	1.77
(A) MIZ, 1 July 2014	0.75	39 (1235)	8 (33)	4 (28)	56	417 (25,650)	1.35
(B) MIZ, 30 July 2014	0.68	35 (145)	12 (24)	5 (9)	21	72 (482)	2.96
(C) MIZ, 14 August 2014	0.71	38 (681)	11 (28)	5 (19)	30	120 (5,640)	2.53

[a]Geometric properties of melt ponds from the 2011 DISTANCE and 2014 MIZ field sites. The letters in parentheses denote the following stages of melt pond evolution: (A) maximum coverage, (B) after drainage, and (C) late season melt, just prior to floe breakup. The standard deviation is included in parentheses next to the mean value of the corresponding melt pond property.

At (A) maximum melt pond coverage, melt pond geometries between the DISTANCE and MIZ sub-floes were comparable (Table 4.3). The melt pond circularities were equal, and the

averages of melt pond perimeters and axis dimensions were similar. The largest difference between melt pond geometries was in the standard deviation of melt pond perimeters, of which the MIZ melt ponds had three times more variability than the DISTANCE melt ponds.

From (A) maximum coverage to (B) drainage, the circularity of melt ponds at both sites decreased due to the narrowing of interconnected melt ponds (Figure 4.13, upper panels) and development of narrow drainage channels (Figure 4.13, lower panels), which added to the complexity of the melt pond shapes, as further indicated by larger ratios between the major and minor axis dimensions. From drainage (Figure 4.13B) to late season melt (Figure 4.13C), the DISTANCE melt pond circularity increased to its near maximum value due to the widening of old melt ponds and drainage channels, and the development of connections between previously isolated ponds.

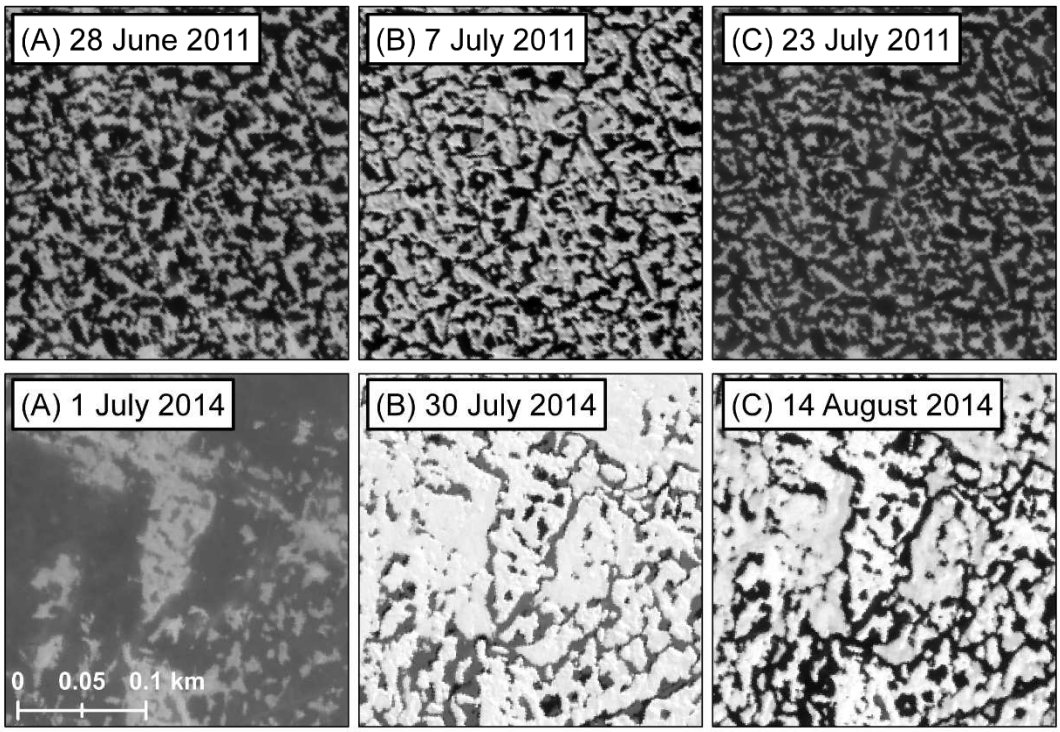

Figure 4.13 NTM scene subsets representative of the evolution in the fractal nature of melt ponds on the **(Top)** 2011 DISTANCE and **(Bottom)** 2014 MIZ sub-floes. Stages of melt pond evolution are labeled as: **(A)** maximum melt pond coverage, **(B)** drainage, and **(C)** late season melt, just prior to floe breakup.

4.5.5 *DISTANCE melt pond distributions are less heterogeneous than MIZ*

At (A) peak coverage, melt ponds covered 56% of the both the DISTANCE and MIZ sub-floes (Table 4.3), which is a similar value to previous observations of ~50% and larger melt pond fractions on drifting first-year sea ice [*Fetterer and Untersteiner,* 1998; *Perovich et al.,* 2002b]. Despite the similarity in melt pond fractions, the DISTANCE melt pond areas were four times smaller and had double the melt pond density than those on the MIZ sub-floe (Table 4.3).

The MIZ's distributions of melt pond areas were highly variable over time, as noted by the large changes in the fitted lines in Figure 4.14, bottom panel. The green fitted line for the MIZ sub-floe (Figure 4.14, bottom) had the largest absolute values in slope and y-intercept of all fitted probability lines (Table 4.4), which was indicative of the abundance of large melt ponds. Interestingly, all slopes of the fitted probabilities were smaller than those found in Perovich et al., [2002b]; they calculated a -1.5 slope for the distributions of melt pond sizes late in the melt season at the 1998 SHEBA field campaign. We attribute the difference to the composition of 85% MY ice and 15% FY at the SHEBA study site [*Perovich et al.,* 2002b]; MY ice typically has a larger abundance of small, isolated melt ponds throughout the melt season due to rough surface topography, which constrains the lateral spread in surface meltwater [*Fetterer and Untersteiner,* 1998; *Perovich et al.,* 2002b; *Webster et al.,* 2015]. Hence, a fitted probability of MY melt pond area distributions in late summer would tend to have a relatively large slope and small y-intercept.

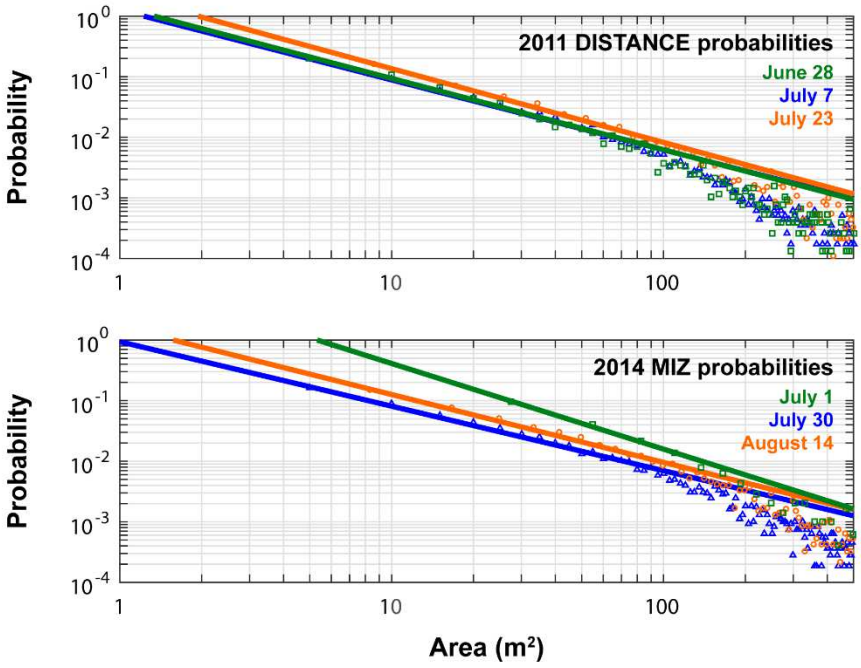

Figure 4.14 The probabilities of melt pond areas based on melt pond distributions from the 2011 DISTANCE **(Top)** and 2014 MIZ **(Bottom)** sub-floes during maximum melt pond coverage **(green)**, melt pond drainage **(blue)**, and late season melt **(orange)**. The fitted lines are power functions that have been converted to a log-log scale. The correlation coefficients are 0.990 or higher (Table 4.4).

Table 4.4 Fits for the probabilities of melt pond areas using a power function[a]

$f(x) = A*(x)^B$	A	B	R
DISTANCE, 28 June 2011	1.266	–1.155	0.994
DISTANCE, 7 July 2011	1.413	–1.197	0.996
DISTANCE, 23 July 2011	2.246	–1.218	0.995
MIZ, 1 July 2014	10.640	–1.414	0.993
MIZ, 30 July 2014	0.940	–1.065	0.990
MIZ, 14 August 2014	1.662	–1.120	0.990

[a]The coefficients (A and B) and correlation coefficients (R) of the fit lines of melt pond areas and probabilities for the three melt stages for the 2014 MIZ and 2011 DISTANCE sub-floes using a power function. Note, the results are shown on a log-log scale in Figure 4.14.

After (B) melt pond drainage, melt pond fractions decreased to 34% and 21% for the DISTANCE and MIZ sub-floes, respectively (Table 4.3). On average, both sub-floes had comparable melt pond areas (Table 4.3), but the DISTANCE sub-floe had a slightly larger abundance of small melt ponds (blue lines in Figure 4.14; Table 4.4). The DISTANCE site had three times as much variability in melt pond area as the MIZ sub-floe, as shown by the standard deviations in Table 4.3. From (A) peak coverage to (B) drainage, the MIZ melt pond areas decreased by a factor of almost six, with the largest melt ponds undergoing the most dramatic change, while smaller ponds on its deformed sea ice remained largely unaffected (Figure 4.13). Many melt ponds became disconnected from one another after drainage (Figure 4.13) and accordingly, melt pond densities increased on the DISTANCE and MIZ sub-floes, with the DISTANCE sub-floe having nearly double the pond density as that on the MIZ sub-floe (Table 4.3).

From drainage (B) to late season melt (C), the DISTANCE melt ponds rebounded to the maximum melt pond fraction (56%), while MIZ melt ponds increased to 30% (Table 4.3). The DISTANCE melt ponds were larger in size relative to those on the MIZ sub-floe, as indicated by the larger y-intercept and slope of the fitted yellow line (Figure 4.14; Table 4.4). In some areas, the MIZ melt ponds appeared to be in the late stages of melt pond evolution, exhibiting highly interconnected, fractal shapes; in other areas, particularly on deformed sea ice, smaller, more circular melt ponds were present due to melt ponds being either at an earlier stage in evolution or more constricted in their lateral growth due to rough surface topography (Figure 4.13). On both sub-floes, melt pond densities decreased, with the DISTANCE sub-floe undergoing a greater decrease in density than the MIZ sub-floe (Table 4.3). Visible in the NTM imagery (Figure 4.13), the larger decrease in melt pond density may have been due to the widening of old melt ponds and drainage channels, as well as the development of connections between previously isolated ponds.

4.5.6 *Spatial scaling of melt pond distributions at the DISTANCE and MIZ sites*

Significant variability in melt pond distributions was present on spatial scales of four km^2 and smaller for the homogenous (2011 DISTANCE) and heterogeneous (2014 MIZ) case studies based on the results of the melt pond geometries, fractions, area probabilities, and densities. As a follow-up to this finding, we ask: does the spatial scaling of melt pond distributions differ between homogenous and heterogeneous sea ice environments? To answer this question, we calculated the aggregate-scale estimates of melt pond fractions following Perovich and Tucker [1997]. This method analyzes subsets of incrementally-increasing size until the standard deviation in melt pond fractions reaches a minimum. Using the coefficients (A and B) of the fitted lines in Figure 4.15

(Table 4.5), the theoretical aggregate-scales were found by setting the standard deviation in melt pond fractions, *SD*, to zero and solving for the area of interest:

$$Area = e^{(SD-B)\times A^{-1}} \tag{4.3}$$

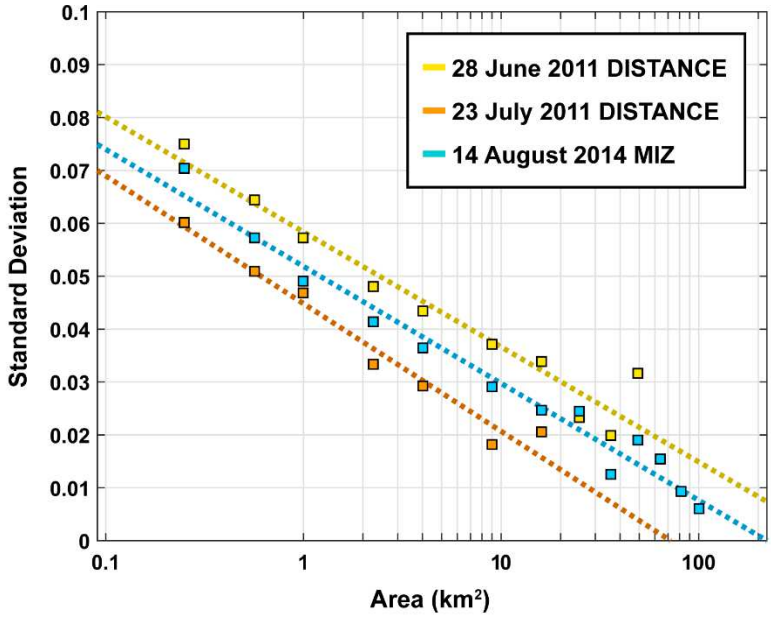

Figure 4.15 The standard deviations melt pond fractions of the 28 June 2011 DISTANCE (**yellow**), 23 July 2011 DISTANCE (**orange**), and 14 August 2014 MIZ (**blue**) NTM scenes. The solid lines are power law fits for which the associated coefficients are listed in Table 4.5.

The DISTANCE results from the 28 June 2011 (before melt pond drainage) and 23 July 2011 (after melt pond drainage) NTM scenes are shown in Figure 4.15. Due to the limited coverage of the 2014 MIZ site in clear-sky conditions, only results from the 14 August 2014 NTM scene are shown. For the 2011 DISTANCE site, the aggregate scales were ~480 km^2 (22 km by 22 km) for 28 June, and ~70 km^2 (eight km by eight km) for 23 July. The 2014 MIZ site had an aggregate

scale of ~220 km^2 (15 km by 15 km) for the 14 August NTM scene. After melt pond drainage, the aggregate scale for the heterogeneous site was more than double that of the homogenous site.

Compared to previous works, the aggregate scales from the 2011 DISTANCE and 2014 MIZ sites are considerably larger. Perovich and Tucker [1997], using airborne imagery, estimated two-three km^2 but were limited by the three km^2 areal extent of their study area. Fetterer and Untersteiner [1998], using NTM imagery of predominantly multiyear sea ice from earlier years, estimated 30 km^2 but suggested it was a tentative result due to the limited sample size of the NTM imagery. Perovich et al. [2002b], using airborne imagery, concluded that the aggregate scale was more than six km^2, as the variability in melt pond fractions had not yet reached a minimum at that spatial scale.

Perhaps of equal interest is that the spatial scaling appears to differ before and after melt pond drainage at the homogenous site, as shown by the difference between the yellow (before drainage) and orange (after drainage) fitted lines in Figure 4.15. There is the possibility that, due to sea ice drift, the NTM scenes of 28 June 2011 and 23 July 2011 may not have sampled the same sets of sea ice floes or sea ice types. Webster et al. [2015] showed a five percent difference in multiyear sea ice composition between the 28 June and 23 July NTM scenes, which may be too small of a difference to create such variability between melt pond distributions. Nevertheless, with this in mind, the difference between the variability in melt pond fractions before and after drainage suggest that aggregate-scale estimates of melt pond fractions may be sensitive to the stage of melt pond evolution, particularly in cases just prior to melt pond drainage.

Table 4.5 Fits for the standard deviations in melt pond fractions[a]

*f(x) = A*log(x) + B*	A	B	R^2
DISTANCE, 28 June 2011	-0.009445	0.05838	0.93
DISTANCE, 23 July 2011	-0.010480	0.04482	0.96
MIZ, 14 August 2014	-0.009604	0.05186	0.97

[a]The coefficients (A and B) and squared correlation coefficients (R^2) of the fitted lines of the standard deviations in melt pond fractions as a function of area for the 2011 DISTANCE and 2014 MIZ sites, as shown in Figure 4.15.

4.6 DISCUSSION

As described in Section 4.2, three things influence melt ponds: surface topography, available meltwater, and sea ice permeability. Here, we explore the environment conditions that may have contributed to the heterogeneity in melt pond fractions between the sub-floe and its surroundings at the 2014 MIZ site, and provide four hypotheses on possible mechanisms that facilitated large melt pond coverage on the sub-floe prior to melt pond drainage.

The first hypothesis is that less deformed surface topography fosters large melt pond fractions. Based on the standard deviation in sea ice thickness, the sea ice surface roughness of the MIZ sub-floe was considerably less pronounced than its surroundings (Figure 4.12; Table 4.2). However, the 2014 MIZ sub-floe had rougher topography than the 2011 DISTANCE sub-floe, yet both had equal melt pond fractions prior to melt pond drainage (Table 4.3). Thus the evidence is ambiguous, which indicates that other factors, in additional to surface topography, were involved and may play equally important roles as surface topography in controlling melt pond coverage.

The second hypothesis is that more available meltwater increases melt pond fractions. The snow cover on the sub-floe was five centimeters deeper than its surroundings (Figure 4.12; Table 4.2). Using a bulk snow density of 330 kg m^{-3} for wind-packed snow and depth hoar [*Warren et al.,* 1999; *Sturm et al.,* 2002b], a five cm difference would amount to an additional ~1.7 cm per cm^2 area of snow water equivalent (SWE) on the sub-floe, which is not large enough to fully explain the sub-floe's large melt pond fraction. Furthermore, the difference in SWE between the 2011 DISTANCE and 2014 MIZ sub-floes was less than one cm per cm^2 area, which, depending on whether or not the snow densities between sub-floes differed, suggests that both sub-floes had comparable amounts of meltwater from snow. Although the data supports this hypothesis, the effect is not large enough to explain the observations.

The third hypothesis is that the lateral meltwater transport increases melt pond fractions. The surface elevation and snow results in Table 4.2 reveal that the MIZ sub-floe had a lower freeboard than the surrounding sea ice, based on the difference between the surface elevations and snow depths. Because meltwater flows downhill to the lowest elevation areas, the sub-floe may have accumulated more meltwater along its border with neighboring, thicker sea ice floes and ridges. Work by Eicken et al. [2002] have shown that meltwater can travel distances over 16 meters over deformed sea ice; however, their study was limited to the floe size where the study took place, and it is currently unknown how far meltwater can travel across sloped sea ice surfaces. Furthermore, it is not known whether or not the contribution of meltwater from higher elevation surfaces is a local effect or can span several kilometers. The data qualitatively support this hypothesis, but more evidence is needed for validation.

The fourth hypothesis is that low sea ice permeability increases melt pond fractions. Sea ice permeability affects the timing and depth at which the superimposed, freshwater ice layer forms

(Section 4.2). As described in hypotheses two and three, the freshwater supply to the sub-floe may have been relatively larger than its surroundings due to melt from a deeper snow cover and greater lateral meltwater transport from neighboring, thicker sea ice floes. If this were the case, the larger amount of freshwater may have reduced the permeability of the sub-floe via the incorporation of freshwater in its sea ice structure, thereby diluting the brine in brine channels and creating fresher, superimposed ice in places where freezing temperatures were encountered (Section 4.2). Cooler sea ice temperatures also reduce sea ice permeability by decreasing brine volumes [*Untersteiner,* 1986; *Golden et al.,* 2007], and in addition to freshwater melt, facilitate shallower superimposed freshwater ice layers within the sea ice surface. To the author's knowledge, no sea ice salinity, temperature, and permeability data were collected at the 2014 MIZ site, but the effects of freshwater vs. saline water on sea ice permeability is a topic of on-going research, which may provide future insight into this hypothesis. The data are thus inconclusive on this hypothesis.

4.7 CONCLUSION

This study contributes to the understanding of melt ponds by linking small-scale variability in melt pond, snow, and sea ice properties to aggregate-scale estimates of melt pond distributions. Specifically, the results: (1) show that the geometric properties of melt ponds display the largest variability prior to melt pond drainage at the heterogeneous sea ice site, but after melt pond drainage at the homogenous sea ice site (2) confirm that aggregate-scale estimates of melt pond fractions for the homogenous and heterogeneous sites are larger than previously recognized, ranging from ~8 km by ~8 km to ~ 22 km by ~22 km, and (3) suggest that aggregate-scale estimates

are dependent on the composition of sea ice types as well as the stage of melt pond evolution in the study area.

Although this study provides new information on the spatial scaling of melt pond properties, it is limited to two case studies, and thus more information is needed for better understanding the relationships between the spatial scaling of melt pond distributions, composition of sea ice types, and stages of melt pond evolution. Such information could be gained by examining additional sites with varying stages of melt pond evolution on different sea ice types from different years and locations. Regarding future research directions, there is a need for field observations of lateral meltwater transport and sea ice permeability on spatial scales leading up to several kilometers for establishing which mechanisms influence intra-floe heterogeneity in melt pond distributions. As demonstrated with the 2011 DISTANCE and 2014 MIZ campaigns, these observational needs can be met through the coordinated efforts between the observational, remote sensing, and modelling communities. We anticipate that such efforts to understand and implement small-scale processes in models will be a way forward in successfully capturing intra-floe heterogeneity in melt pond distributions.

Chapter 5. Conclusions

The ice mass balance of the Arctic sea ice cover is governed by the interplay between dynamic and thermodynamic processes. In this dissertation, I focused on the roles of snow and melt ponds in thermodynamic processes, but consideration of sea ice dynamics is essential for understanding the results and their implications to feedbacks within the Arctic system. In Section 5.1, I summarize the major findings and discuss their impacts in the broader context of climate change. To conclude, suggestions are given on future directions in sea ice research involving the coordinated efforts between the modeling, observational, and remote sensing communities.

5.1 SUMMARY AND IMPACTS OF KEY FINDINGS

5.1.1 *Interdecadal change in snow depth*

In Chapter 2, we learned that spring snow depth distributions in the western Arctic have decreased, and that the decrease is attributed to the delay in sea ice formation in autumn. While a multitude of feedbacks affect one another due to the delay in sea ice formation [*Serreze et al.,* 2009; *Stroeve et al.,* 2014], this discussion focuses on the feedbacks resulting from a thinner snow cover, and the associated changes that can be expected in a future seasonally ice-free Arctic. Snow has dual roles in sea ice mass balance in winter and summer [*Maykut and Untersteiner,* 1971; *Maykut,* 1986; *Thomas and Dieckmann,* 2010]. As such, a thinner snow cover has two contrasting effects in these seasons.

In winter, a thinner snow cover has a negative feedback. Thinner snow allows more heat loss from the ocean to the atmosphere, thereby increasing winter sea ice growth rates. Shown by

Maykut and Untersteiner [1971], the growth of sea ice with a thickness of one meter or less is highly sensitive to changes in snow depth. With the projected decline in sea ice thickness [*Lindsay and Zhang,* 2005], one can expect snow to play an increasingly important role in heat loss from the ocean to the atmosphere in winter. Consequently, deep water formation will likely be affected by the amount of snow on thinner sea ice. Less snow enables more heat loss and sea ice growth, resulting in a larger production of deep water formation, which in turn, ultimately impacts global thermohaline circulation [*Aagaard et al.,* 1985; *Aagaard and Carmack,* 1989]. What is less well-understood is the effect of more snow falling into open water in autumn. Snowfall freshens the surface ocean and provides more nucleation points for ice crystallization to occur [*Untersteiner,* 1986; *Petrenko and Whitworth,* 1999], which would counteract the delay in freeze-up by promoting sea ice formation. Unknown is whether snow density and metamorphism will change with the changes in the temperature gradient between the atmosphere and ocean, in the frequency of blowing snow events, and in atmospheric moisture content.

In contrast to winter, the feedback of a thinner snow cover in late spring and summer is largely positive. Thinner snow requires less radiation to melt completely, and as a consequence, the surface becomes snow-free earlier in the melt season. The early absence of snow increases the cumulative amount of sea ice surface melt due to the low albedo of sea ice (0.70) relative to that of snow (0.85), and causes a corresponding increase in solar absorption and transmission in sea ice [*Perovich et al.,* 2007*; Perovich and Polashenski,* 2012]. Thus, thin snow acts to reduce the overall thickness of the sea ice cover via the effects of a reduced surface albedo in the ice-albedo feedback [*Maykut and Untersteiner,* 1971; *Curry et al.,* 1995; *Perovich et al.,* 2002a].

A thinner snow cover has a more complex effect on melt pond evolution, however. On the one hand, thin snow shifts melt pond processes earlier in the melt season, advancing the

progression of solar absorption and transmission into the underlying surface ocean. This shift impacts the phenology of the sympagic ecosystem, in which many species critically rely on the temporal balance between availability in photosynthetically active radiation and food, the latter of which often depend on processes such as nutrient-upwelling and prey availability [*Post et al.,* 2013; *Leu et al.,* 2015]. In cases where snow is optically-thin, the earlier shift can lead to a timing offset of three weeks and more. From a biological perspective, three weeks is sufficiently long for creating a temporal mismatch between available primary producers and foraging grazers [*Leu et al.,* 2015]. Thus thinner snow enhances timing offsets, and may effectively reduce the energy (biomass) transfer to higher trophic levels.

In extreme cases, such as little or no snow, the effect on melt pond evolution is the opposite. When little or no snow is present, melt pond formation is inhibited by the insufficient amount of freshwater melt. Freshwater melt is key to melt pond formation as it sustains sea ice impermeability via the formation of superimposed, sub-surface fresh ice layers, on which meltwater can accumulate [*Eicken et al.,* 2002; *Eicken et al.,* 2004]. With the projected increase in younger and thus more saline sea ice types [*WMO,* 1970; *Johnston and Timco,* 2008], the amount of available freshwater melt may become increasingly important for melt pond formation to take place.

There is still the outstanding question of whether or not snow accumulation rates will increase, despite projections that they will rise due to the increasing trend in open water and corresponding moisture fluxes in autumn and winter [*Liu et al.,* 2012; *Stocker et al.,* 2013]. More recent works have shown increases in moisture fluxes over many regions of the Arctic for autumn and spring using satellite data [*Boisvert et al.,* 2013; *Boisvert and Stroeve,* 2015]. However, the effects of increased moisture flux on larger snow accumulation rates have not presented themselves in the available observational data to date [*Webster et al.,* 2014]. It is not known whether these

effects should be localized near leads and open water or be more widespread over the sea ice pack. While all of the pieces for increased snow accumulation are coming into play, a change in snow accumulation rates still remains to be seen. It is important to consider processes that serve as sinks for snow, and thus may impede an observable increase in snow accumulation rates: longer distances of snow drift due to the greater presence of less deformed sea ice associated with younger sea ice types [*WMO,* 1970; *Johnston and Timco,* 2008], an increase in cracks and leads due to the greater mobility of a thinner sea ice cover [*Kwok,* 2006; *Rampal et al.,* 2009], and more frequent rain-on-snow events.

5.1.2 *Seasonal Melt Pond Evolution*

In Chapter 3, we learned three key things: (1) melt pond fractions on drifting first-year sea ice are ~1.5 times larger than those on drifting multiyear ice, (2) snow depth distributions influence the timing of melt pond onset, and (3) the uniformity in melt pond distribution and seasonal evolution are inversely related to sea ice deformation.

There are several positive feedbacks associated with first-year melt pond fractions. The albedo of melt ponds is largely determined by the presence of a surface scattering layer and the thickness of the underlying sea ice. First-year and younger sea ice types lack a surface scattering layer, as they have not experienced meltwater flushing associated with a summer melt season, and thus, their melt ponds are more transmittive compared to those on multiyear sea ice [*Light et al.,* 2015]. As the fraction of first-year sea ice increases in the Arctic, one can expect more solar absorption and transmission in sea ice and the underlying ocean, due to both inherent optical properties and larger melt pond coverage. More solar absorption increases the amount of internal

and bottom sea ice melt [*Perovich et al.,* 2011] and raises the oceanic heat content [*Steele et al.,* 2008], which further delays the timing of sea ice formation [*Markus et al.,* 2009]. The uniform distribution of first-year melt ponds also acts to distribute the light field underneath the sea ice cover more evenly, and thus, would create a more widespread distribution in solar absorption [*Frey et al.,* 2011]. While some studies have shown that an increase in solar radiation in the Arctic Ocean will increase primary productivity [*Arrigo et al.,* 2008; *Kahru et al.,* 2011; *Slagstad et al.,* 2011] and the success rate of open ocean-like species [*Wassmann et al.,* 2010; *Grebmeier et al.,* 2012], others have shown it to have a negative impact on organisms specially adapted to low-light conditions [*Leu et al.,* 2010].

Snow distribution plays an important role in the timing of melt pond onset, and its distribution is determined by surface topography, blowing snow events, and the composition of sea ice types and open water from autumn to spring. Wind-driven snow redistribution is likely to become a positive feedback for multiyear sea ice in the MIZ. In autumn when young sea ice has yet to form, snow is blown off of sparsely-scattered multiyear floes and into the surface ocean, thereby reducing total snow depth and distribution on multiyear floes in the MIZ. Once young sea ice forms around individual multiyear floes, blowing snow events continue to reduce the snow depth on multiyear sea ice, as drifting snow is effectively trapped onto the lower elevation of young ice relative to the larger freeboard of multiyear sea ice. This reduced snow depth facilitates an earlier formation of melt ponds on multiyear sea ice, which leads to a faster progression of surface melt during the summer.

The level of deformation in surface topography controls the magnitude of melt pond fractions and the uniformity, or lack thereof, in melt pond distributions and seasonal evolution. First-year sea ice is less deformed than multiyear, so that, as a whole, the seasonal Arctic sea ice

cover may become smoother, more uniform, and more ponded than it is today. Smoother surface topography allows snow to drift more freely, creating a more uniform snow depth distribution, which later influences the geometric properties of melt ponds in summer. On an aggregate spatial scale, the effects of smooth topography on melt pond fractions would reduce the surface albedo of the Arctic sea ice cover, and further reduce the survivability of the ice during the summer melt season.

Less well-understood are the effects of uniform melt pond drainage on the properties of the surface ocean. Large volumes of warm, fresh meltwater will increase the stratification of the surface mixed layer [*Toole et al.,* 2010; *Peralta-Ferriz and Woodgate,* 2015], which may effectively trap the meltwater underneath the sea ice, enhancing bottom melt. However, in early autumn when sea ice is at its thinnest, open water is at its maximum extent, and storms occur most frequently; turbulent mixing via sea ice drift and wave action may bring both this fresh, warm meltwater deeper into the water column and the deep ocean heat into the surface mixed layer, increasing the mixed layer depth and its ocean heat content [*Rainville et al.,* 2011; *Peralta-Ferriz and Woodgate,* 2015].

5.1.3 *Spatial scaling of melt pond distributions*

In Chapter 4, we learned that: (1) melt pond geometry is most variable before melt pond drainage at a heterogeneous sea ice site, but after pond drainage at a homogenous sea ice site, (2) aggregate-scale estimates of melt pond fractions at the homogenous and heterogeneous sea ice sites are larger than previously recognized, ranging from ~70 km^2 to ~480 km^2, and (3) aggregate-scale estimates of melt pond fractions may be dependent on the composition of sea ice types and stage of melt

pond evolution. The implications of these findings are tentative as Chapter 4 was limited to two case studies. As such, implications of these findings are briefly described with the caveat that the two case studies may not be wholly representative of homogenous and heterogeneous sea ice environments.

As the Arctic continues to transition toward a seasonal state, the surface topography of the sea ice pack may become smoother and more uniform as more undeformed, first-year sea ice replaces thicker, hummocky multiyear sea ice [*Nghiem et al.,* 2007; *Maslanik et al.,* 2011]. Surface topography modifies the following seasons' thermodynamic processes by controlling the re-distribution of winter snow [*Radionov et al.,* 1997; *Sturm et al.,* 2002] and summer melt pond distributions [*Fetterer and Untersteiner, 1998; Perovich et al.,* 2002b; *Webster et al.,* 2015], both of which are key players in the ice-albedo feedback [*Curry et al.,* 1995; *Perovich et al.,* 2002a; *Perovich and Polashenski,* 2012].

If undeformed, first-year sea ice becomes the dominant sea ice type in the future Arctic, smoother, more uniform surface topography will impact the spatial scaling of melt pond distributions by reducing the overall complexity in melt pond properties. The geometric properties will be more sensitive to the stage of melt pond evolution, and less sensitive to sea ice properties that typically vary between sea ice types and facilitate differences in melt pond distributions and behaviors. On a seasonal basis, small-scale variability in melt pond geometry will increase as melt pond evolution progresses, because melt ponds on undeformed first-year sea ice become increasingly interconnected and fractal with the later stages in melt pond evolution. Obtaining statistically-representative estimates of melt pond distributions in a future, seasonal Arctic may be more feasible due to the greater uniformity in geometric properties and thus smaller aggregate

scales estimates in melt pond coverage relative to sea ice environments composed of a mixture of sea ice types, like we observe in the present-day.

5.2 SUGGESTED FUTURE DIRECTIONS

The following discussion echoes the sentiments of Untersteiner [1986]: the rapid advancement in sea ice and global models warrants their use in guiding the future efforts in field and remote sensing observations. At this point in time, high-resolution numerical sea ice models are running simulations at spatial resolutions of one-to-several kilometers, which are spatial scales at which the dynamic and thermodynamic interactions between individual floes become increasingly important. It is pragmatic to expect a continual progression in sea ice model resolution and computational capability, which will allow for the incorporation of more small-scale processes that affect the ice mass balance of the Arctic sea ice cover. Here, we discuss future directions in the field on snow on sea ice based on two selected modelling studies that highlight snow processes that are poorly observed and/or understood, but can be built on readily.

In recent work by Light et al. [2015], the seasonal evolution of surface albedo was compared between remotely-sensed observations and output from the Community Climate System Model v.4 (CCSM4). Relative to the observational data, the model results exhibited a higher surface albedo and a shorter duration of low albedo during summer. Upon closer inspection, these discrepancies were attributed to summer snowfall events, during which snow accumulation effectively halted the progression of melt pond formation, resulting in “frozen summers.” These results reveal that model parameterizations of snow and melt ponds are particularly sensitive to

episodic snowfall events during summer, and solicit further work on identifying the frequency of summer snowfall events and the duration of the freshly accumulated snow.

Unfortunately, observations of summer snowfall events are sparse. Even in the data sets from Soviet drifting stations used to create the 1937 and 1954–1991 snow climatology, snow line measurements ceased when snow became less than five centimeters in depth or when the snow coverage dropped below 50% [*Warren et al.,* 1999]. Fortunately, qualitative observations of "frozen summers" exist from the Soviet drifting ice station data, and have been used to quantify the frequency of frozen summers. For the more contemporary period, snow data from the Cold Regions Research and Engineering Laboratory ice mass balance (IMB) buoys have proved to be a goldmine of information on summer snowfall frequency, snow cover duration, and the average and variability in the magnitude of summer snow accumulation. These data, together with logs documenting weather events from multiple field campaigns, have been used to quantify the frequency of snowfall events and "frozen summers" for validating CCSM model output, and exploring ways for improving its snow parameterizations [*Bailey et al.,* in progress].

A recent study by Lecomte et al. [2015] highlighted the importance of the distribution of wind-driven snow in the timing and areal fraction of melt ponds in the Louvain-la-Neuve (LIM) sea ice model. Similar to the CESM results by Light et al. [2015], the LIM model overestimated summer surface albedo, particularly over regions of multiyear sea ice. Unlike the CESM study, the overestimation in surface albedo was attributed to the delayed onset of melt pond formation, and the slow progression of melt pond evolution due to a thick spring snow cover. A blowing-snow parameterization was implemented, in which a percentage of blowing snow was lost to leads. To briefly summarize the results, blowing snow thinned the spring snow cover, which led to earlier melt pond formation, greater melt pond coverage, and faster sea ice surface melt, but multiyear ice

still exhibited melt pond fractions that were lower than observations. The results of this insightful study open up a flurry of questions whose answers require not just field and remotely-sensed observations, but a dialogue between the modeling and observational communities: (1) how much blowing snow is lost to leads?, (2) how far does snow drift on level sea ice?, (3) what effects do individual floes with differing morphology have on snow redistribution?, and (4) how do snow depth distributions change over a range in spatial scales?

An ongoing effort is being made to evaluate the spatial scaling of snow depth distributions over two contrasting morphological cases of sea ice, level and deformed sea ice, at sub-grid- and grid-scale levels using in situ, airborne, satellite, and model data [*Webster et al.,* in progress]. The objectives are to explore the spatial scaling of snow depth distributions in relation to sea ice deformation, assess snow depth distributions in the Community Earth System Model (CESM), and identify useful geophysical characteristics of the sea ice cover for improving the parameterizations of snow distribution. We anticipate that the results will provide insight into the spatial scales over which the topographic effects on snow redistribution occur, which will assist with future developments in modelling snow processes.

References

Arntsen, A.E., Song, A.J., Perovich, D.K., and J.A. Richter-Menge (2015), Observations of the summer breakup of an Arctic sea ice cover, *Geophys. Res. Lett.,* 42, doi:10.1002/2015GL065224.

Arrigo, K.R., Dijken, G., and S. Pabi, (2008), Impact of a shrinking Arctic ice cover on marine primary production. *Geophys. Res. Lett., 35*, L19603, doi:10.1029/2008GL035028.

Blanchet, J., and A.C. Davidson (2011), Spatial modeling of extreme snow depth, *Ann. Applied Stat., 5*(3), 1699–1725, doi:10.1214/11-AOAS464.

Blazey, B.A., Holland, M.M., and E.C. Hunke (2013), Arctic Ocean sea ice snow depth evaluation and bias sensitivity in CCSM. *The Cryosphere Discussions, 7*, 1495-1532, doi:10.5194/tcd-7-1495-2013.

Boisvert, L.N., and J.C. Stroeve (2015). The Arctic is becoming warmer and wetter as revealed by the Atmospheric Infrared Sounder. *Geophys. Res. Lett.* 42, 4439–4446. doi: 10.1002/2015GL063775

Boisvert, L., Markus, T., and T. Vihma (2013), Moisture flux changes and trends for the entire Arctic in 2003–2011 derived from EOS Aqua data, *J. Geophys. Res.,* 118, 5829–5843, doi:10.1002/jgrc.20414.

Brigham, L.W. (2007), Thinking about the Arctic's future: Scenarios for 2040. The Futurist 41:27–34.

Brucker, L., and T. Markus (2013), Arctic-scale assessment of satellite passive microwave-derived snow depth on sea ice using Operation IceBridge airborne data, *J. Geophys. Res. Oceans, 118*, 2892-2905, doi:10.1002/jgrc.20228.

Budikova, D. (2009), Role of Arctic sea ice in global atmospheric circulation: A review, *Global Planet. Change,* 68(3), 149–163, doi:10.1016/j.gloplacha.2009.04.001.

Cavalieri, D.J. and C.L. Parkinson (2012), Arctic sea ice variability and trends, 1979–2010, *Cryosphere,* 6(4), pp. 881–889, doi: 10.5194/tc-6-881-2012.

Comiso, J. (2010), *Polar oceans from space,* Springer, New York.

Deser, C., Tomas, R., Alexander, M., and D. Lawrence (2010), The seasonal atmospheric response to projected Arctic sea ice loss in the late twenty-first century, *J. Clim*., 23, pp. 333–351.

Dickson, R.R., and J. Brown (1994), The production of North Atlantic Deep Water: Sources, rates

and pathways, *J. Geophys. Res.,* 99, 12 319–12 341.

Doble, M.J., De Carolis, G., Meylan, M.H., Bidlot, J.R., and P. Wadhams (2015), Relating wave attenuation to pancake ice thickness, using field measurements and model results, *Geophys. Res. Lett.,* 42, 4473–4481, doi:10.1002/2015GL063628.

Dominguez, R. (2010, updated 2014), *IceBridge DMS L1B Geolocated and Orthorectified Images.* [20110323]. Boulder, Colorado USA: NASA DAAC at the National Snow and Ice Data Center.

Eicken, H., Gradinger, R., Salganek, M., Shirasawa, K., Perovich, D., and M. Leppäranta, (2009), Field Techniques for Sea Ice Research. University of Alaska Press, Fairbanks.

Eicken, H., Grenfell, T.C., Perovich, D.K., Richter-Menge, J.A., and K. Frey (2004), Hydraulic controls of summer Arctic pack ice albedo. *J. Geophys. Res., 109*, C08007, doi:10.1029/2003JC001989.

Eicken, H., Krouse, H.R., Kadko, D., and D.K. Perovich (2002), Tracer studies of pathways and rates of meltwater transport through Arctic summer sea ice. *J. Geophys. Res., 107,* C108046, doi:10.1029/2000JC000583.

Eicken, H., Tucker, I.I.I., and D.K. Perovich (2001), Indirect measurements of the mass balance of summer Arctic sea ice with an electromagnetic induction technique, *Ann. Glaciol.,* 33, 194-200, doi:10.3189/172756401781818356.

Farrell, S.L., Kurtz, N., Connor, L.N., Elder, B.C., Leuschen, C., Markus, T., McAdoo, D.C., Panzer, B., Richter-Menge, J., and J.G. Sonntag (2012), A first assessment of IceBridge snow and ice thickness data over Arctic sea ice, *IEEE Trans. Geosci. Remote Sens.,* 50(6), 2098-2111, doi:10.1109/TGRS.2011.2170843.

Fetterer, F., and N. Untersteiner (1998), Observations of melt ponds on Arctic sea ice. *J. Geophys. Res.,* 103, C11, pp. 24,821–24,835.

Fetterer, F., and V. Radionov (2000), Arctic Climatology Project. Environmental working group Arctic meteorology and climate atlas. Boulder, CO: National Snow and Ice Data Center. CD-ROM. http://dx.doi.org/10.7265/N5MS3QNJ

Filhol, S., and M. Sturm (2015), Snow bedforms: A review, new data, and a formation model, *J. Geophys. Res. Earth Surf.,* 120, doi:10.1002/2015JF003529.

Flato, G., J. Marotzke, J., Abiodun, B., Braconnot, P., Chou, S.C., Collins, W., Cox, P., Driouech,

F., Emori, S., Eyring, V., Forest, C., Gleckler, P., Guilyardi, E., Jakob, C., Kattsov, V., Reason, C., and M. Rummukainen, 2013: Evaluation of Climate Models. In: Climate Change (2013), The physical science basis. Contribution of Working Group I to the Fifth Assessment Report of the Intergovernmental Panel on Climate Change [Stocker, T.F., D. Qin, G.-K. Plattner, M. Tignor, S.K. Allen, J. Boschung, A. Nauels, Y. Xia, V. Bex and P.M. Midgley (eds.)]. Cambridge University Press, Cambridge, UK and New York, NY, USA.

Flocco, D., Feltham, D.L., and A.K. Turner (2010), Incorporation of a physically based melt pond scheme into the sea ice component of a climate model. *J. Geophys. Res. 115,* C08012. http://dx.doi.org/10.1029/2009JC005568.

Flocco, D., Schroeder, D., Feltham, D.L., and E.C. Hunke, (2012), Impact of melt ponds on Arctic sea ice simulations from 1990 to 2007. *J. Geophys. Res.,* 117, C9, doi:10.1029/2012JC008195.

Frey, K.E., Perovich, D.K., and B. Light (2011), The spatial distribution of solar radiation under a melting Arctic sea ice cover. *Geophys. Res. Lett., 38,* L22501, doi:10/1029/2011GL049421.

Gardner, J., Richter-Menge, J., Farrell, S., and J. Brozena (2012), Coincident Multiscale Estimates of Arctic Sea Ice Thickness, *EOS Transactions*, 93:(6) 57-58.

George, J.C., Huntington, H.P., Brewster, K., Eicken, H., Norton, D.W., and R. Glenn (2004), Observations on shorefast ice dynamics in Arctic Alaska and the responses of the Iñupiat hunting community, *Arctic, 57,* pp. 363–374.

Gloersen, P., Campbell, W.J., Cavalieri, D.J., Comiso, J.C., Parkinson, C.L., and H.J. Zwally (1992) Arctic and Antarctic sea ice, 1978-1987: Satellite passive-microwave observations and analysis. NASA: Washington D.C.

Golden, K.M., Eicken, H., Heaton, A.L., Miner, J., Pringle, D.J., and J. Zhu (2007) Thermal evolution of permeability and microstructure in sea ice, *Geophys. Res. Lett., 34,* L16501, doi:10.1029/2007GL030447

Grebmeier, J.M., Moore, S.E., Overland, J.E., Frey, K.E., and R. Gradinger (2010), Biological response to recent Pacific Arctic sea ice retreats. Eos Trans. AGU, 91(18), 161-168.

Grenfell, T.C., and D.K. Perovich (1984), Spectral albedos of sea ice and incident solar irradiance

in the southern Beaufort Sea, J. Geophys. Res., 89, 3573-3580.

Hezel, P.J., Zhang, X., Bitz, C.M., Kelly, B.P., and F. Massonnet (2012), Projected decline in spring snow depth on Arctic sea ice caused by progressively later autumn open ocean freeze-up this century. *Geophys. Res. Lett., 39*, L17505, doi:10.1029/2012GL052794.

Hohenegger, C., Alali, B., Steffen, K.R., Perovich, D.K., and K.M. Golden (2012), Transition in the fractal geometry of Arctic melt ponds, The Cryosphere, 6, 1157–1162, doi:10.5194/tc-6-1157-2012.

Holland, M.M., Bailey, D.A., Briegleb, B.P., Light, B., and E. Hunke, (2012), Improved sea ice shortwave radiation physics in CCSM4: The impact of melt ponds and aerosols on Arctic sea ice. *J. Climate*, doi:10.1175/JCLI-D-11-00078.1.

Holland, M.M., Bitz, C.M., and B. Tremblay (2006), Future abrupt reductions in the summer Arctic sea ice, *Geophys. Res. Lett.,* 33, L23503, doi:10.1029/2006GL028024.

Hunke, E.C., Hebert, D.A., and O. Lecomte, (2013), Level-ice melt ponds in the Los Alamos sea ice model, CICE. *Ocean Modelling,* 71, pp. 26–42.

IPCC (2013), *Climate Change 2013: The Physical Science Basis.* Contribution of Working Group I to the Fifth Assessment Report of the Intergovernmental Panel on Climate Change Stocker, T.F., Qin, D., Plattner, G.K., Tignor, M., Allen, S.K., Boschung, J., Nauels, A., Xia, Y., Bex, V., and P.M. Migley (eds.). Cambridge University Press, Cambridge, United Kingdom and New York, NY, USA, 1535 pp.

Johnston, M.E., and G.W. Timco (2008), *Understanding and identifying old ice in summer.* Canadian Hydraulics Centre, National Research Council Canada, Ottawa, Ontario, Canada.

Kahru, M., Brotas, V., Manzano-Sarabia, M., and B.G. Mitchell (2011), Are phytoplankton blooms occurring earlier in the Arctic? *Glob. Change Biol.* 17:1733–1739.

Kalnay, E., Kanamitsu, M., Kistler, R., Collins, W., Deaven, D., Gandin, L., Iredell, M., Saha, S., White, G., Woollen, J., Zhu, Y., Chelliah, M., Ebisuzaki, W., Higgins, W., Janowiak, J., Mo, K.C., Ropelewski, C., Wang, J., Leetmaa, A., Reynolds, R., Jenne, R., and D. Joseph (1996), The NCEP/NCAR 40-year reanalysis project. *Bull. Amer. Metero. Soc.,* 77, pp. 437-470.

Killworth, P.D. (1983), Deep convection in the World Ocean. *Rev. Geophys. Space Phys.,* 21, pp. 1-26.

Kirtman, B., Power, S.B., Adedoyin, J.A., Boer, G.J., Bojariu, R., Camilloni, I., Doblas-Reyes, F.J., Fiore, A.M., Kimoto, M., Meehl, G.A., Prather, M., Sarr, A., Schär, C., Sutton, R., van Oldenborgh, G.J., Vecchi, G., and H.J. Wang (2013), Near-term climate change: projections and predictability. In: Climate change 2013: The physical science basis. Contribution of Working Group I to the Fifth Assessment Report of the Intergovernmental Panel on Climate Change. Eds: Stocker, T.F., D. Qin, G.-K. Plattner, M. Tignor, S.K. Allen, J. Boschung, A. Nauels, Y. Xia, V. Bex and P.M. Midgley. Cambridge University Press, Cambridge, UK and New York, NY, USA.

Knowles, K.W. (1993), Points, pixels, grids, and cells -- a mapping and gridding primer. Unpublished report to the National Snow and Ice Data Center, Boulder, Colorado USA.

Koenig, L., Martin, S., Studinger, M., and J. Sonntag (2010), Polar airborne observations fill gap in satellite data, *Eos Trans. AGU,* 91(38), 333–334, doi:10.1029/2010eo380002

Krabill, W.B. (2010), IceBridge ATM L1B Elevation and Return Strength (2011/2012), NASA DAAC at the National Snow and Ice Data Center, Boulder, CO [Updated 2013].

Krupnik, I. and D. Jolly (2002), The Earth is Faster Now: Indigenous Observations of Arctic Environmental Change, Arctic Research Consortium of the United States, Fairbanks, USA, 356.

Kurtz, N., and S. Farrell (2011), Large-scale surveys of snow depth on Arctic sea ice from Operation IceBridge. *Geophys. Res. Lett., 38*, L20505, doi:10/1029/2011GL049216.

Kurtz, N., Farrell, S.L., Galin, N., Harbeck, J.P., Lindsay, R., Onana, V.D., Panzer, B., and J.G. Sonntag (2013b), Sea ice thickness, freeboard, and snow depth products from Operation IceBridge airborne data. *The Cryosphere, 7*, 1035-1056, doi:10.5194/tc-7-1035-2013.

Kurtz, N., Studinger, M., Farrell, S., Paden, J., Richter-Menge, J., Sonntag, J., and J. Yungel (2013a), IceBridge airborne survey data support Arctic sea ice predictions, Eos Trans. AGU, 94(4), 41, doi:10.1002/2013EO040001.

Kurtz, N., Studinger, M., Harbeck, J., Onana, V.D., and S. Farrell (2012), IceBridge Sea Ice Freeboard, Snow Depth, and Thickness. Version 1. [2009, 2010, 2011]. Boulder, Colorado USA: NASA DAAC at the National Snow and Ice Data Center.

Kwok, R. (2013), Declassified high-resolution visible imagery for Arctic sea ice investigations: An overview, *Rem. Sens. Envir.,* 142, 44-56, doi:10.1016/j.rse.2-13.11.015.

Kwok, R., and D.A. Rothrock (2009), Decline in Arctic sea ice thickness from submarine and ICESat records: 1958-2008. *Geophys. Res. Lett., 36*, L15501, doi:10.1029/2009GL039035.

Kwok, R., and G.F. Cunningham (2008), ICESat over Arctic sea ice: Estimation of snow depth and ice thickness. *J. Geophys. Res.,* 113, C08010, doi:10.1029/2008JC00475.

Laidler, G. (2006), Inuit and scientific perspective on the relationship between sea ice and climate change: the ideal complement? Clim. Change, 78, pp. 407.

Laidler, G., Ford, J.D., Gough, W.A., Ikummaq, T., Gagnon, A.S., Kowal, S., Qrunnut, K., and C. Irngaut (2009), Assessing Inuit vulnerability to sea ice change in Igloolik, Nunavut, Clim. Change, 94, pp. 363-397.

Laxon S., Giles, K.A., Rideout, A.L., Wingham, D.J., Willat, R., Cullen, R., Kwok, R., Schweiger, A., Zhang, J., Haas, C., Hendricks, S., Krishld, R., Kurtz, N., Farrell, S., and M. Davidson (2013), CryoSat-2 estimates of Arctic sea ice thickness and volume. *Geophys. Res. Lett., 40*, 732-737, doi:10/1002/grl.50193.

Leu, E., Wiktor, J., Søreide, J.E., Berge, J., and S. Falk-Petersen (2010) Increased irradiance reduces food quality of sea ice algae, *Mar. Ecol. Prog. Ser.,* 411, pp. 49-60.

Leuschen, C., (2009), updated current year. IceBridge Snow Radar L1B Geolocated Radar Echo Strength Profiles, Apr. 2, 2009–Apr. 25, 2013]. Boulder, Colorado USA: National Snow and Ice Data Center. Digital media.

Light, B., Grenfell, T.C., and D.K. Perovich (2008), Transmission and absorption of solar radiation by Arctic sea ice during the melt season. *J. Geophys. Res., 113,* C03023, doi:10.1029/2006JC003977.

Light, B., Perovich, D.K., Webster, M.A., Polashenski, C., and R. Dadic (2015), Optical properties of melting first-year Arctic sea ice, *J. Geophys. Res. Oceans,* 120, 7657–7675, doi:10.1002/2015JC011163.

Lindsay, R., and A. Schweiger (2015), Arctic sea ice thickness loss determined using subsurface, aircraft, and satellite observations, Cryosphere, 9, 269–283, doi:10.5194/tc-9-269-2015.

Lindsay, R.W., and J. Zhang (2005), The thinning of Arctic sea ice, 1988–2003: Have we passed a tipping point?, J. Clim., 18, 4879–4894.

Lindsay, R., Wensnahan, M., Schweiger, A., and J. Zhang (2014), Evaluation of seven different atmospheric reanalysis products in the Arctic. *J. Clim.* 27, doi:10.1175/JCLI-D-13-00014.1

Liu, J., Curry, J., Wang, H., Song, M., and R. Horton (2012), Impact of declining Arctic sea-ice on winter snowfall, *Proc. Natl. Acad. Sci.* USA, 109, 4074–4079.

Lowry, R.T., and P. Wadhams (1979), On the statistical distribution of pressure ridges in sea ice, *J. Geophys. Res., 84,* C5, pp. 2487-2494.

Mahoney, A., Eicken, H., Gaylord, A.G., and L. Shapiro (2007), Alaska landfast sea ice: Links with bathymetry and atmospheric circulation, *J. Geophys. Res., 112,* C02001, doi:10.1029/2006JC003559.

Markus, T., Stroeve, J.C., and J. Miller (2009), Recent changes in Arctic sea ice melt onset, freezeup, and melt season length. *J. Geophys. Res., 114*, C12024, doi:10.1029/2009JC005436.

Marr, J. C. (1940), Snow surveying, U.S. Dept. of Agri., Technology and Engineering, pp. 9-11.

Martin, C.F., Krabill, W.B., Manizade, S.S., Russell, R.L., Sonntag, J.G., Swift, R.N., and J.K. Yungel (2012), Airborne topographic mapper calibration procedures and accuracy assessment, Tech. Rep. NASA/TM–2012–215891, pp. 1–32, Natl. Aeronaut. and Space Admin., NASA Cent. for AeroSpace Inform., Hanover, MD.

Martin, T., Steele, M., and J. Zhang (2014), Seasonality and long-term trend of Arctic Ocean surface stress in a model, *J. Geophys. Res. Oceans,* 119, doi:10.1002/2013JC009425.

Maslanik, J., Stroeve, J., Fowler, C., and W. Emery (2011), Distribution and trends in Arctic sea ice age through spring 2011. *Geophys. Res. Lett., 38*, L13502, doi:10.1029/2011GL047735.

Maykut, G.A. (1978), Energy exchange over young sea ice in the central Arctic. *J. Geophys. Res., 83*, 8C0241, doi:10.1029/JC083iC07p03646.

Maykut, G.A. (1982), Large-scale heat exchange and ice production in the central arctic. *J. Geophys. Res.,* 87, 7971–7984.

Maykut, G.A. (1986), The surface heat and mass balance in *The Geophysics of Sea Ice*, 395-465, N. Untersteiner, Plenum, New York.

Maykut, G.A., and N. Untersteiner (1971), Some results from a time-dependent thermodynamic model of sea ice. *J. Geophys. Res., 76*(6), 1550-1575, doi:10.1029/JC076i006p01550.

Morison, J.H., and M. McPhee (2001), Ice-ocean interaction, in Encyclopedia of Ocean Sciences, edited by J. Steele et al., pp. 1271–1281, Academic, London, doi:10.1006/rwos.2001.0003.

National Academies (2012), *Seasonal to Decadal Predictions of Arctic Sea Ice–Challenges and Strategies*, Polar Research Board, National Research Council, 92 pp., ISBN 978-0-309-26526-3, National Academies Press, Washington, D.C.

Nazintsev, Y.L. (1964), Teplovoi balans poverkhnosit mnogoletnego lediandogo pokrova v tsentral'noi Arktike, *Akrt. Antarkt. Nauchno-Issled. Inst. Tr.,* 267, 110–126.

Nghiem, S.V., Clemente-Colon, P., Douglas, T., Moore, C., Obrist, D., Perovich, D.K., Pratt, K.A., Rigor, I.G., Simpson, W., Shepson, P.B., Steffen, A., and J. Woods (2013), Studying Bromine, Ozone, and Mercury in the Arctic, Eos Trans. AGU, 94(33), 289-291.

Nghiem, S.V., Rigor, I.G., Perovich, D.K., Celemente-Colon, P., Weatherly, J.W., and G. Neumann (2007), Rapid reduction of Arctic perennial sea ice, *Geophys. Res. Lett., 34*, L19504, doi:10.1029/2007GL031138.

Nicolaus, M., Katlein, C., Maslanik, J., and S. Hendricks (2012), Changes in Arctic sea ice result in increasing light transmittance and absorption. *Geophys. Res. Lett., 39,* L24501, doi:10.1029/2012GL053738.

Ono, N. (1967), Specific heat and fusion of sea ice, in Physics of Snow and Ice: International Conference on Low Temperature Science 1966, vol. 1 (1), edited by H. Oura, pp. 599–610, Inst. of Low Temp. Sci., Hokkaido Univ., Sapporo, Japan.

Overland, J.E., and M. Wang (2010), Large-scale atmospheric circulation changes are associated with the recent loss of Arctic sea ice, *Tellus A*, 62, pp. 1–9.

Overpeck, J.T., Sturm, M., Francis, J.A., Perovich, D.K., Serreze, M.C., Benner, R., Carmack, E.C., Chapin III, F.S., Gerlach, S.C., Hamilton, L.C., Hinzman, L.D., Holland, M., Huntington, H.P., Key, J.R., Lloyd, A.H., MacDonald, G.M., McFadden, J., Noone, D., Prowse, T.D., Schlosser, P., and C. Vörösmarty (2005), Arctic system on trajectory to new, seasonally ice-free state, Eos Trans. AGU, 86(34), 209-316.

Panzer, B., Gomez-Garcia, D., Leuschen, C., Paden, J., Rodriguez-Morales, F., Patel, A., Markus, T., Holt, B., and P. Gogineni (2013), An ultra-wideband, microwave radar for measuring snow thickness on sea ice and mapping near-surface internal layers in polar firn, *J. Glaciology, 59*(214), 244-254, doi:10.3189/2013JoG12J128.

Parkinson, C.L. and D. Cavalieri (2008), Arctic sea ice variability and trends, 1979–2006, *J. Geophys. Res., 113,* C07003, doi:10.1029/2007JC004558.

Parkinson, C.L., Cavalieri, D.J., Gloersen, P., Zwally, H.J., and J. Comiso (1999), Arctic sea ice extents, areas, and trends, 1978–1996. J. Geophys. Res., 104 (C9), 20 837–20.

Peralta-Ferriz, C., and R.A. Woodgate (2014) Seasonal and interannual variability of pan-Arctic surface mixed layer properties from 1979 to 2012 from hydrographic data, and the dominance of stratification for multiyear mixed layer depth shoaling, *Prog. Oceanogr.* 134, 19–53, doi:10.1016/j.pocean.2014.12.005.

Perovich, D.K., and C. Polashenski (2012), Albedo evolution of seasonal Arctic sea ice. *Geophys. Res. Lett., 39*, L08501, doi:10.1029/2012GL051432.

Perovich, D.K., and W.B. Tucker III (1997), Arctic sea-ice conditions and the distribution of solar radiation during summer, *Ann. Glaciol., 25*, pp. 445-450.

Perovich, D.K., Grenfell, T.C., Light, B., and P.V. Hobbs (2002a), Seasonal evolution of the albedo of multiyear Arctic sea ice. *J. Geophys. Res., 107*(C10), 8044, doi:10.1029/2000JC000438.

Perovich, D.K., Grenfell, T.C., Richter-Menge, J.A., Light, B., Tucker III, W.B., and H. Eicken (2003), Thin and thinner: Sea ice mass balance measurements during SHEBA. *J. Geophys. Res.,* 108, C3, doi:10.1029/2001JC001079.

Perovich, D.K., Light, B., Eicken, H., Jones, K.F., Runciman, K., and S.V. Nghiem (2007), Increasing solar heating of the Arctic Ocean and adjacent seas, 1979-2005: attribution and role in the ice-albedo feedback. *Geophys. Res. Lett., 34*, L19505, doi:10.1029/2007GL031480.

Perovich, D.K., Richter-Menge, J.A., and W.B. Tucker III (2001), Seasonal changes in Arctic sea-ice morphology, *Ann. Glaciology,* 33, pp. 171–176.

Perovich, D.K., Richter-Menge, J.A., Elder, B., Arbetter, T., Claffey, K., and C. Polashenski (2013), Observing and understanding climate change: Monitoring the mass balance, motion, and thickness of Arctic sea ice, http://imb.erdc.dren.mil.

Perovich, D.K., Tucker III, W.B., and K.A. Ligett (2002b), Aerial observations of the evolution of ice surface conditions during summer. *J. Geophys. Res.,* 107, C10, doi:10.1029/2000JC000449.

Petrenko, V.F., and R.W. Whitworth (1999), *Physics of ice,* Oxford University Press, Oxford, U.K.

Petrich, C., Eicken, H., Polashenski, C.M., Sturm, M., Harbeck, J.P., Perovich, D.K., and D.C.

Finnegan (2012a), Snow dunes: a controlling factor of melt pond distribution on Arctic sea ice. *J. Geophys. Res., 117*, C09029, doi:10.1029/2012JC008192.

Petrich, C., Eicken, H., Zhang, J., Krieger, J., Fukamachi, Y., and K.I. Ohshima (2012b), Coastal landfast sea ice decay and breakup in northern Alaska: Key processes and seasonal prediction, *J. Geophys. Res., 117,* C02003, doi:10.1029/2011JC007339.

Pringle, D.J., Eicken, H., Trodahl, H.J., and L.G.E. Backstrom (2007), Thermal conductivity of landfast Antarctic and Arctic sea ice, J. Geophys. Res., 112, C04017, doi:10.1029/2006JC003641.

Pringle, D.J., Trodahl, H.J., and T.G. Haskell (2006), Direct measurement of sea ice thermal conductivity: No surface reduction. *J. Geophys. Res., 111*, C05020, doi:10.1029/2005JC002990.

Polashenski, C., Perovich, D.K., and Z. Courville (2012), The mechanisms of sea ice melt pond formation and evolution. *J. Geophys. Res.,* 117, C01001, doi:10.1029/2011JC007231.

Post, E., Bhatt, U.S., Bitz, C.M., Brodie, J.F., Fulton, T.L., Hebblewhite, M., Kerby, J., Kutz, S.J., Stirling, I., and D.A. Walker (2013), Ecological consequences of sea-ice decline, *Science* 341 (6145), 519–524.

Radionov, V.F., Bryazgin, N.N., and E.I. Alexandrov (1997), The Snow cover of the Arctic Basin, Tech. Rep. *APL-UW-TR 9701,* 95 pp., Appl. Phys. Lab., Univ. of Wash., Seattle, Wash.

Rainville, L., and R.A. Woodgate (2009), Observations of internal wave generation in the seasonally ice-free Arctic, *Geophys. Res. Lett.,* 36, L23604, doi:10.1029/2009GL041291.

Rainville, L., Lee, C., and R. Woodgate (2011), Impact of wind-driven mixing in the Arctic Ocean, *Oceanography,* 24(3), 136–145, doi:10.5670/oceanog.2011.65.

Rheimnitz, E., Toimil, L., and P. Barnes (1978), Arctic continental shelf morphology related to sea-ice zonation, Beaufort Sea, Alaska, *Marine Geology, 28*, pp. 179-210.

Ruddiman, W.F. (2000), *Earth's Climate: Past and Future,* W.H. Freeman, New York.

Scharien, R.K., and J.J. Yackel (2005), Analysis of surface roughness and morphology of first-year sea ice melt ponds: Implications for microwave scattering, *IEEE Trans. Geosci. Remote Sens.,* 43, 2927, doi:10.1109/TGRS.2005.857896.

Schröder, D., Feltham, D.L., Flocco, D., and M. Tsamados (2014), September arctic sea-ice minimum predicted by spring melt-pond fraction, *Nat. Clim. Change,* 4, 353–357,

doi:10.1038/nclimate2203

Schweiger, A., Zhang, J., Lindsay, R., Steele, M., and H. Stern (2012), Pan-Arctic Ice Ocean Modeling and Assimilation System (PIOMAS). http://psc.apl.washington.edu/wordpress/research/projects/arctic-sea-ice-volume-anomaly/.

Screen J.A., Simmonds, I., Deser, C., and R. Tomas (2013), The atmospheric response to three decades of observed Arctic sea ice loss, *J. Clim.* 26, pp.1230–1248.

Serreze, M.C., Barrett, A.P., Stroeve, J.C., Kindig, D.M., and M.M. Holland (2009), The emergence of surface based Arctic amplification. *Cryosphere* 3:11–19

Slagstad, D., Ellingsen, I., and P. Wassmann (2011), Evaluating primary and secondary production in a future Arctic Ocean void of summer sea ice: an experimental simulation approach. *Prog. Ocean. 90,* 117–131. doi:10.1016/j.pocean.2011.02.009.

Squire, V.A., Vaughan, G.L., and L.G. Bennetts (2009), Ocean surface wave evolvement in the Arctic Basin, *Geophys. Res. Lett.,* 36, L22502, doi:10.1029/2009GL040676.

Stocker, T.F., D. Qin, G.-K. Plattner, L.V. Alexander, S.K. Allen, N.L. Bindoff, F.-M. Bréon, J.A. Church, U. Cubasch, S. Emori, P. Forster, P. Friedlingstein, N. Gillett, J.M. Gregory, D.L. Hartmann, E. Jansen, B. Kirtman, R. Knutti, K. Krishna Kumar, P. Lemke, J. Marotzke, V. Masson-Delmotte, G.A. Meehl, I.I. Mokhov, S. Piao, V. Ramaswamy, D. Randall, M. Rhein, M. Rojas, C. Sabine, D. Shindell, L.D. Talley, D.G. Vaughan and S.-P. Xie (2013), Technical Summary. In: Climate Change 2013: The Physical Science Basis. Contribution of Working Group I to the Fifth Assessment Report of the Intergovernmental Panel on Climate Change [Stocker, T.F., D. Qin, G.-K. Plattner, M. Tignor, S.K. Allen, J. Boschung, A. Nauels, Y. Xia, V. Bex and P.M. Midgley (eds.)]. Cambridge University Press, Cambridge, United Kingdom and New York, NY, USA.

Stroeve, J., Holland, M.M., Meier, W., Scambos, T., and M. Serreze (2007), Arctic Sea Ice Decline: Faster than Forecast. *Geophys. Res. Lett.,* 33, L09501, doi:10.1029/2007GL029703.

Stroeve, J.C., Markus, T., Boisvert, L., Miller, J., and A. Barrett (2014), Changes in Arctic melt season and implications for sea ice loss, *Geophys Res Lett* 41, doi:10.1002/2013GL058951

Stroeve, J.C., Serreze, M.C., Holland, M.M., Kay, J.E., Maslanik, J., and A.P. Barrett (2012), The

Arctic's rapidly shrinking sea ice cover: a research synthesis. *Clim. Change, 110*,1005-1027, doi:10.1007/s10584-011-0101-1.

Sturm, M., Holmgren, J., and D.K. Perovich (2002b), Winter snow cover on the sea ice of the Arctic Ocean at the Surface Heat Budget of the Arctic Ocean (SHEBA): Temporal evolution and spatial variability. *J. Geophys. Res., 107,* C108047, doi:10.1029/2000JC000400.

Sturm, M., Holmgren, J., König, M., and K. Morris (1997), The thermal conductivity of seasonal snow, *J. Glaciol.,* 43, 26–41, 1997.

Sturm, M., Perovich, D.K., and J. Holmgren (2002a), Thermal conductivity and heat transfer through the snow on the ice of the Beaufort Sea, *J. Geophys. Res.,* 107, C21, 8043, doi:10.1029/2000JC000409.

Thomas, D.N. and G.S. Dieckmann (2010), Sea Ice, 2nd Ed., Wiley-Blackwell, Oxford, pp. 247-424.

Thorndike, A.S., Rothrock, D.A., Maykut, G.A., and R. Colony (1975), The thickness distribution of sea ice, *J. Geophys. Res.,* 80, 33, pp. 4501–4513.

Toole, J.M., Timmermans, M.-L., Perovich, D.K., Krishfield, R.A., Proshutinsky, A., and J.A. Richter-Menge (2010) Influences of the ocean surface mixed layer and thermohaline stratification on arctic sea ice in the central Canada Basin. *J. Geophys. Res.,* 115, C10018, doi:10.1029/2009JC005660.

Trodahl, H.J., Wilkinson, S., McGuinness, M., and T. Haskell (2001), Thermal conductivity of sea ice: Dependence on temperature and depth, Geophys. Res. Lett., 28, 1279–1282.

Untersteiner, N. (1986), *The Geophysics of Sea Ice,* Plenum Press, New York, NY, USA.

Van der Zwaag, D. and C. Lamson (1990), The Challenge of Arctic Shipping: Science, Environmental Assessment and Human Values, Montreal/Toronto, McGill-Queen's University Press.

Vihma, T. (2014), Effects of Arctic sea ice decline on weather and climate: a review. *Surv. Geophys.* 35, pp. 1–40.

Wadhams, P. (1986), The seasonal ice zone. In *The Geophysics of Sea Ice* (ed. N. Untersteiner), Plenum Press, New York, pp. 825 - 991.

Wadhams, P. (2000), *Ice in the Ocean,* Gordon and Breach Science Publishers, Cambridge.

Warren, S., Rigor, I.G., Untersteiner., N., Radionov, V.F., Bryazgin, N.N., Aleksandrov, Y.I., and R. Colony (1999), Snow depth on Arctic sea ice. *J. Climate, 12*, 1814-1829.

Wassmann, P., Duarte, C.M., Agusti, S., and M.K. Sejr (2011), Footprints of climate change in the Arctic marine ecosystem. *Global Change Biology, 17*, 1235-1249.

Webster, M.A., Rigor, I.G., Nghiem, S.V., Kurtz, N.T., Farrell, S.L., Perovich, D.K., and M. Sturm (2014), Interdecadal changes in snow depth on Arctic sea ice, *J. Geophys. Res. Oceans,* 119, doi:10.1002/2014JC009985.

Webster, M.A., Rigor, I.G., Perovich, D.K., Richter-Menge, J.A., Polashenski, C.M., and B. Light (2015), Seasonal evolution of melt ponds on Arctic sea ice, J. Geophys. Res. Oceans, 120, doi:10.1002/2015JC011030.

Weidemann, L. (2014), International Governance of the Arctic Marine Environment: With Particular Emphasis on High Seas Fisheries, New York, Springer Science & Business Media, 27.

World Meteorological Organization, WMO Sea-Ice Nomenclature, Terminology, Codes, and Illustrated Glossary (1970), WMO/OMM/BMO Series, 259, TP 145, Secretariat World Meteorol. Org., Geneva.

Yackel, J.J., Barber, D.G., and J.M. Hanesiak (2000), Melt ponds on sea ice in the Canadian Archipelago 1. Variability in morphological and radiative properties. *J. Geophys. Res.,* 105, C9, pp. 22,049–22,060.